UNIVERSITÀ DEGLI STUDI DI PADOVA

Dipartimento di Fisica e Astronomia "Galileo Galilei"

Master Degree in Physics

Final Dissertation

Performance study of a novel 2D imaging beta detector for medical applications

Thesis supervisor	**Candidate**
Prof. Marcello Lunardon	**Vittoria Pavanello**
Thesis co-supervisor	
Dr. Piero Giubilato	
Dr. Davide Serafini	

Academic Year 2022/2023

A mia madre e a mio padre,
per aver riempito ogni giorno il mio cuore di affetto.

Contents

Abstract

The ISOLPHARM (ISOL technique for radioPHARMaceuticals) experiment is investigating a novel technology aimed at producing high-purity β-emitter radionuclides for medical applications. The leading objective of ISOLPHARM is to exploit these radioisotopes to develop radiopharmaceuticals with high specific activity: the project currently focuses on the development of a pharmaceutical based on ^{111}Ag, a β/γ-emitter with potential theranostic use. Within this context, the Padova research group is developing a new instrument to measure beta activity with high spatial resolution on planar cell cultures using the ALPIDE chips, MAPS detectors developed for the ITS of the ALICE experiment at CERN. The ALPIDE chips will be arranged in a compact flat geometry to create a detector that can measure beta radioactivity in close contact both with traditional and three-dimensional cell cultures, providing 2D activity images. This technology will have the potential to test the internalization of the ISOLPHARM radiopharmaceutical prototype by cancer cell lines for future in-vitro experiments. The performance and limits of the detector will be assessed through comprehensive system simulations in Geant4, providing insights into the design of the final setup and potential applications of this instrument.

Chapter 1

The ISOLPHARM Project

The ISOLPHARM (ISOL technique for radioPHARMaceuticals) project is a multidisciplinary research initiative focused on the production of high-purity radionuclides for medical applications.

Commissioned by the Legnaro National Laboratories (LNL) of the Italian National Institute for Nuclear Physics (INFN), the project was launched in 2016 with the purpose of utilizing the II generation ISOL (Isotope Separator On-Line) facility SPES (Selective Production of Exotic Species) at LNL to obtain radionuclides for medical use, with a specific focus on ^{111}Ag [1].

ISOLPHARM focuses on the production of both radioisotopes commonly used in nuclear medicine and innovative radionuclides with potential medical applications, which are typically unobtainable through conventional production facilities [2]. The ISOLPHARM method should guarantee reduced costs and a lower environmental impact compared to the traditional techniques required for yielding exotic radioisotopes exploited in nuclear medicine. The research carried out by ISOLPHARM extends beyond the optimization of the production mechanism. In the past years, the ISOLPHARM collaboration has conducted interdisciplinary research activities with the intention of developing a radiopharmaceutical prototype labeled with the ^{111}Ag radioisotope. To achieve this ambitious purpose, ISOLPHARM brings together professionals from many diverse fields, such as physics, engineering, biology, and chemistry. The ISOLPHARM initiative is in fact a multisectoral collaboration among many diverse institutions, including the INFN, the University of Padova (Department of Physics and Astronomy, Department of Chemistry, and Department of Pharmaceutical and Pharmacological Sciences), the University of Trento (Department of Industrial Engineering and BIOtech Research Center [3]), the University of Siena (Department of Physics), the University of Brescia (Department of Mechanical and Industrial Engineering).

Starting from 2023, ISOLPHARM has entered a new phase of experimentation known as ADMIRAL (Advanced Dosimetry Methods and In-vitro Radiobiology of ^{111}Ag Labeled Radiopharmaceuticals). ADMIRAL aims to establish the potential of the developed radiopharmaceutical in both diagnostic and therapeutic contexts. The internalization of this prototype will be tested through a series of in-vitro experiments, exploiting ad hoc imaging techniques and advanced dosimetry methods [4], [5].

Figure 1.1: ADMIRAL logo. From [5].

The ISOLPHARM method (whose patent is owned by the INFN) comprises two main stages, as shown in Figure 1.2. The first stage (discussed in detail in Section 1.1) includes the **ISOL** production of radionuclides, which are channeled in a Radioactive Ion Beam (RIB) with a high level of selectivity. The second stage of radio**PHARM**aceuticals production (described in Section 1.2), involves the synthesis of radiopharmaceuticals from the irradiated secondary target.

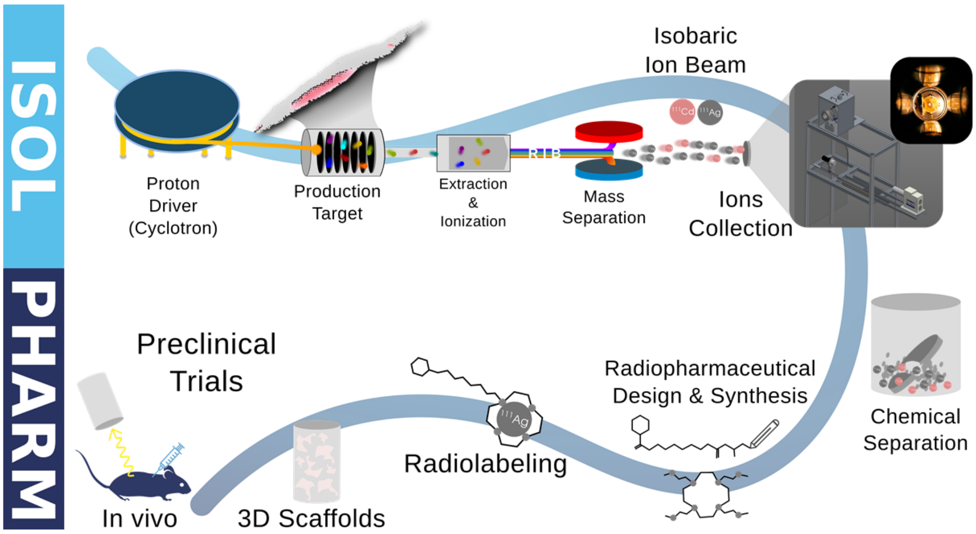

Figure 1.2: Overview of the complete ISOLPHARM production process, divided into its ISOL phase (RIB production and selection) and its PHARM phase (radiopharmaceutical production and testing). From [6].

1.1 ISOL production mechanism

The production of high-quality radioactive ion beams is a critical component of the ISOLPHARM method and is achieved through the use of the SPES (Selective Production of Exotic Species) facility, currently under construction at the Legnaro National Laboratories (LNL).

SPES is an advanced ISOL facility designed with the primary goal of producing intense exotic RIBs [7], [8]. The production of the isotopes of interest relies on a fission reaction induced by a 40 MeV accelerated proton beam (at currents up to 200 μA) hitting a uranium carbide (UC_x) target, made of 7 distinct disks [9]. The uranium used in the production target will be ^{238}U: the yielded nuclei will be thus characterized by a nuclear charge between 28 and 57, the majority of them being neutron-rich. In particular, the fission reaction can lead to the production of many radioisotopes successfully used in nuclear medicine and radiotherapy, such as ^{89}Sr, ^{90}Y, $^{125/131}$I [10], [2] (Figure 1.3 shows all the isotopes that can be produced at SPES). The induced fissions heat the production target to temperatures exceeding 2000 °C, leading to the diffusion and effusion of the yielded radionuclides. As a result, these nuclei evaporate from the target towards an ionizing source under high vacuum conditions (10^{-6} mbar), acquiring a 1+ state charge. The ionization step allows the extraction and the acceleration by means of a high voltage, turning the radioactive ions into a RIB [9], [6]. The desired radioisotopic mass is then selected using an electromagnetic mass separator, which creates an isobaric ultrapure beam and removes isotopic contaminants. The purified beam is finally collected on an implantation substrate, which is subsequently processed to retrieve the radionuclide of interest [10]. Any remaining isobaric contaminant can be removed through chemical separation.

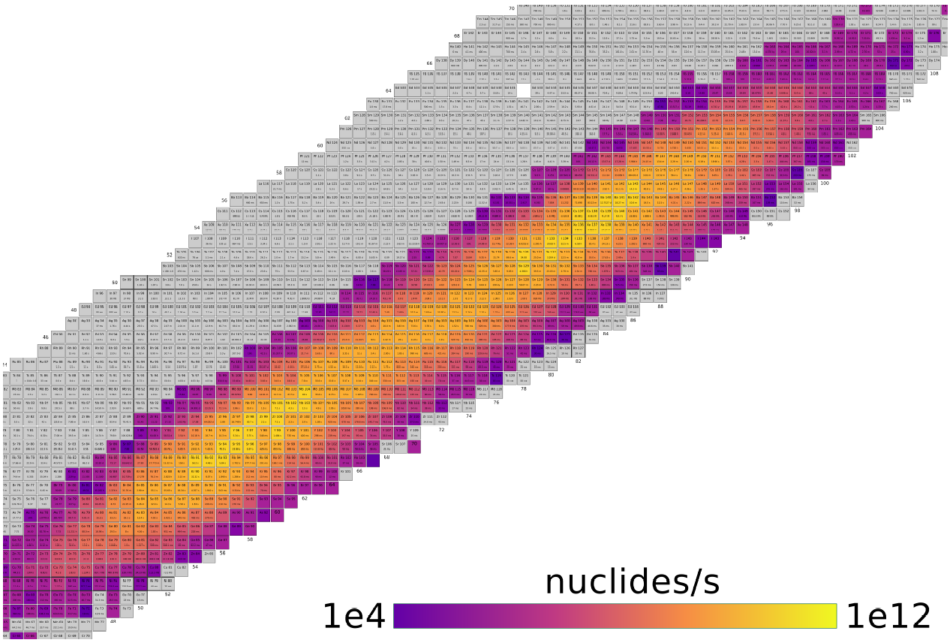

Figure 1.3: SPES isotope production nuclide chart. From [11].

1.2 RadioPHARMaceutical production

The radiopharmaceutical production stage is another crucial element of the ISOLPHARM project. ISOLPHARM aims to produce radiolabelled drugs to treat carcinomas by exploiting the high-purity radionuclides obtained via the ISOL technique. These radiopharmaceuticals should be capable of selectively targeting ill tissues and locally delivering a dose of radiation for diagnostic or therapeutic purposes.

The goal of ISOLPHARM is to integrate the produced isotopes into carrier molecules to provide a targeted biological effect in the tissue of interest. These molecules are characterized by a standard structure, which can be divided into three main constituents [12], [13], as schematized in Figure 1.4:

- a **chelator**, a molecule that can stably bind with coordination covalent bounds and retain the radioisotope in vivo;
- a **targeting agent**, a molecule that binds specifically to cancerous targets, linking with specific receptors overexpressed in the target membrane;
- a **linker**, a molecule that joins the chelator carrying the radioactive nuclide to the targeting molecule.

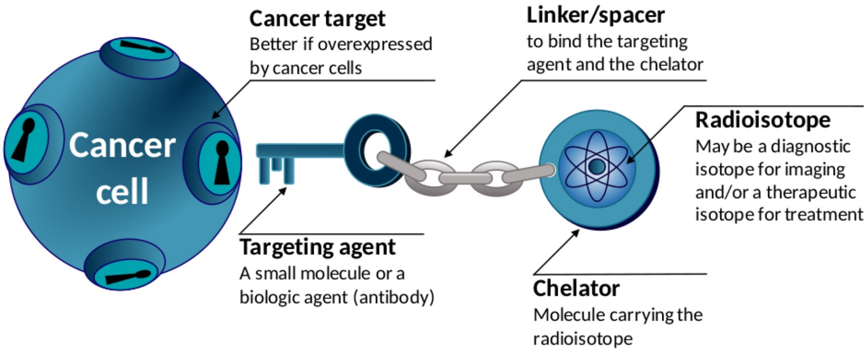

Figure 1.4: Schematic structure and targeting mechanism of a radiopharmaceutical molecule. From [12].

To optimize the structure and composition of the proposed radiolabelled drug, these complex molecules are still under investigation. Before their final commercialization, the radiopharmaceuticals are undergoing in-vitro and ex-vivo experiments in order to inspect their targeting and localized damaging action.

1.3 ISOLPHARM radioisotope production

The ISOL technique performed at the SPES facility has the potential to produce a wide variety of radionuclides, summarized in Figure 1.5.

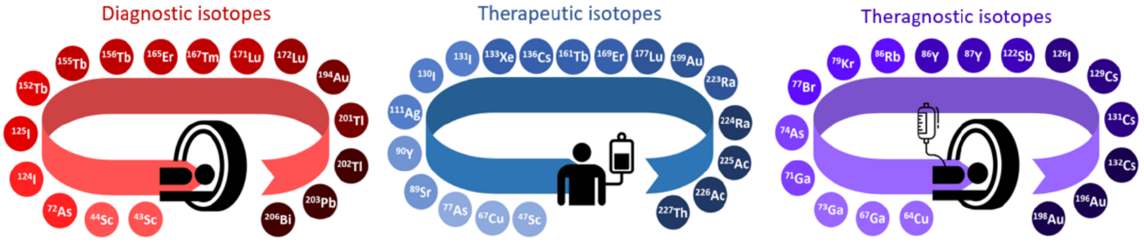

Figure 1.5: Radionuclides of medical interest that can be produced at SPES. From [12].

The fission reaction inside the UC$_x$ production target can yield different n-rich nuclei. Among these, the ISOL method can produce many β-emitting radioisotopes with investigated medical applications, such as ^{89}Sr, ^{90}Y, $^{125/131}$I [10], [2]. ^{89}Sr has been employed in palliative treatments for osseous metastases: being chemically similar to calcium, it can quickly sediment around metastatic deposits (where usually active bone formation takes place) and damage the tumor site [14], [15]. ^{90}Y plays an important role in the treatment of hepatic metastases through brachytherapy [16]. ^{125}I has been analyzed for brachytherapy applications [17] and even employed for imaging purposes exploiting its low energy γ emissions [18]. Similarly, ^{131}I has been used for many years for SPECT imaging [19] as well as for thyroid cancer treatment [20].

The innovation behind the ISOLPHARM production method lies in the ability to produce radionuclides that are already available on the market with excellent purity. The ISOL technique enables a carrier-free production of radioisotopes, including those which are typically produced with a carrier-added yield via traditional production methods (for instance, in the case of ^{89}Sr produced through neutron irradiation) [10].

The ISOLPHARM project did not solely focus on optimizing the production method for radionuclides commonly used in medical physics. The research extended beyond conventional boundaries with a thorough investigation of the production and medical application of ^{111}Ag. The ^{111}Ag radioisotope has been minimally employed in medical physics due to the complexity of its production mechanism (typically neutron capture of ^{110}Pd followed by β-decay of the produced ^{111}Pd [21]) and the associated costs. ISOL production represents a more economical and carrier-free alternative to traditional techniques.

^{111}Ag undergoes β decay to form ^{111}Cd, with a half-life of 7.45 days and an average β- energy of 360 keV [22] (Figure 1.6 shows the energy spectrum of the emitted electrons). This energy makes ^{111}Ag suitable for the treatment of medium size tumors through Targeted Radioactive Therapy (TRT) [21], [23]. The β decay produces ^{111}Cd in an excited state approximately 8.1% of the time: cadmium subsequently undergoes disexcitation via two potential γ emissions of $E_\gamma = 245$ keV and $E_\gamma = 342$ keV. These two radiations might potentially allow for SPECT imaging, hence hopefully leading to a theranostic application of ^{111}Ag.

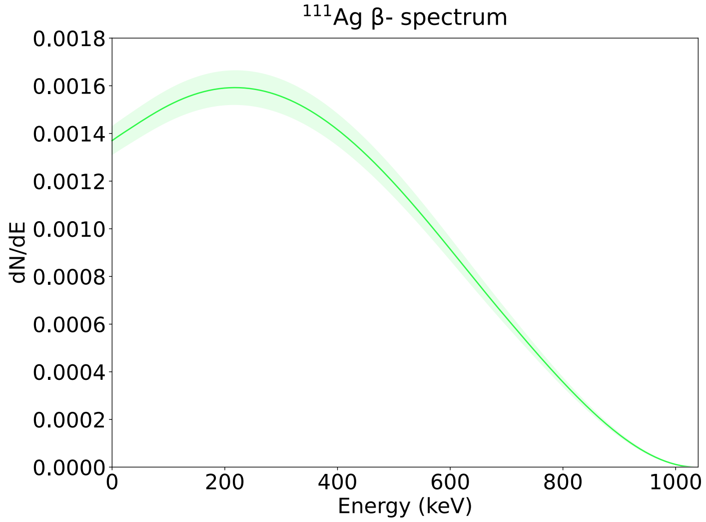

Figure 1.6: Energy spectrum of the β- emitted in the ^{111}Ag decay. Data from NDS [24].

1.4 Thesis objectives

Within the ISOLPHARM framework, the objective of this thesis is to characterize and optimize a new high-resolution large-area 2D β-imaging detector.

In the coming years, ISOLPHARM aims to conduct in-vitro experiments to test the prototype radiopharmaceutical under development. One of ADMIRAL's objectives is to design and construct an innovative β-imaging instrument capable of capturing 2D images from both traditional and three-dimensional cellular cultures. The designed detector will facilitate the investigation of the internalization properties of the prototype drug, *i.e.* its ability to selectively bind to tumor cells. This test will be achieved by detecting the β-radiation emitted by the ^{111}Ag radioisotopes. By generating activity maps that indicate where electrons are produced within the culture, it will be possible to assess the areas where drug molecules have deposited.

To achieve an instrument for this aim, the approach chosen is to exploit high-resolution detectors already available at the University of Padova. The development of this detector will take advantage of the monolithic silicon pixel technology used for the Inner Tracking System of the ALICE experiment at CERN, specifically the ALPIDE chip. By using multiple of these chips in a flat geometry, it will be possible to create a cost-effective β-imaging instrument that can be easily adapted to the geometry of the cell cultures.

This work focuses on evaluating the performance of this device through Monte Carlo simulations, understanding its applicability to the prefixed task. To this end, a detailed simulation model of the detector system was developed using the GEANT4 simulation toolkit [25], which allowed for the study of the behavior of the detector in response to various biological radiation sources. The aim is to create a detailed model of the sensitive and passive detector volumes (the MAPS chip), as well as the mechanical support structure and the cell cultures that will serve as radiation sources. The simulation outcomes shall ultimately facilitate and direct the design of the final setup, allowing for the optimization of different acquisition parameters and for the assessment of the system's resolution limits.

As a first step of the MC validation procedure, experimental data of standard beta sources have been taken with the ALIPIDE detector. The goal is to conduct initial measurements using individual ALPIDE chips to evaluate their response to collimated beta sources with characteristics and emission energies similar to ^{111}Ag, such as ^{90}Sr. These measurements will provide a preliminary understanding of the detector's functioning when dealing with electron sources. These experimental results shall additionally allow for a comparison with the simulation outcomes: in this way, it is possible to test the simulated system and to obtain a potential validation of the GEANT4 simulation.

Chapter 2

Theoretical background

2.1 Electron-Matter Interactions

In order to fully understand the principle of operation of radiation detectors, a deep knowledge of the radiation interactions with matter is required. The interaction processes are influenced by the type and energy of the incoming radiation. Therefore, the detecting mechanism and media used for a specific application must be chosen carefully based on particle type and energy.

When charged particles such as electrons pass through a material, they interact with the atoms in the material and lose energy in the process. The average energy loss per unit path length ($S = -\mathrm{d}E/\mathrm{d}x$) is known as stopping power and it can be divided into different main components corresponding to specific interaction mechanisms.

Electronic stopping power arises from the electromagnetic interaction between the incident charged particle and the electrons in the medium. As the incident particle travels through the material, it ionizes the atoms in its path, liberating electrons from their orbits and generating excited states. These excited states can then relax through the emission of photons or electrons (δ rays), eventually resulting in the generation of additional ionization. This energy loss mechanism is similar for both electrons and other massive charged particles, but there is a difference in the degree of deflection of their trajectories. Electrons undergo significant deflection due to their light mass, while the heavier particles are only slightly deflected.

The electron's electronic stopping power is described by the Rohrlich and Carlson formula [26], [27]:

$$-\left(\frac{\mathrm{d}E}{\mathrm{d}x}\right)^{-}_{e} = S_e = \frac{2\pi n e^4}{m(\beta c)^2}\left[2\ln\left(\frac{mc^2\sqrt{\gamma-1}\gamma\beta}{\sqrt{2}I}\right) + F(\gamma)^{-} - \delta(\beta\gamma)\right],$$

where m is the electron mass at rest, n is the medium number of electrons per cm^3 (dependent on the atomic number Z of the absorber), I is the mean excitation energy of the atoms of the material, γ and β are the relativistic coefficients of the incoming electron. The δ term takes into account the density effect: as the range of the collision is extending, the atoms close to the path of the particle will produce polarization, which results in a screening effect that reduces the electric field strength acting on electrons at large distances. $F(\gamma)^{-}$ is an electron-specific term (a similar one, $F(\gamma)^{+}$, is added when dealing with positrons) which is computed as [26], [27]:

$$F(\gamma)^{-} = 1 - \beta^2 + \ln(2)\frac{(2\gamma-1)}{\gamma} + \frac{(\gamma-1)^2}{8\gamma^2}.$$

Nuclear stopping power (S_{nucl}) arises from the interaction between the incident particle and the nuclei of the atoms in the medium. This interaction is typically much weaker than the electronic interaction

and can be considered negligible in the case of electrons.
Collisional stopping power ($S_{coll} = S_e + S_{nucl}$) dominates the electron energy loss mechanism in the high-energy range (as shown in Figure 2.1 for silicon). When the energy of the electron exceeds a few tens of MeV, the primary energy loss mechanism shifts to the emission of photons through radiative energy loss. *Bremsstrahlung* (braking radiation) consists of the emission of electromagnetic radiation when the charged particle is accelerated due to the presence of an external electric field (the main contribution when electrons traverse a medium is related to the nuclei electric field). The associated radiative stopping power can be computed as [27]:

$$-\left(\frac{\mathrm{d}E}{\mathrm{d}x}\right)_r \simeq \frac{E}{X_0},$$

where X_0 is the radiation length, *i.e.* the distance over which the electron has reduced its energy by a factor e. The radiation length can be calculated as [28], [27]:

$$\frac{1}{X_0} = 4n_A\overline{\phi}\ln\frac{183}{Z^{1/3}},$$

where n_A is the number of atoms per cm^3, $\overline{\phi}$ is the unit of cross section for *bremsstrahlung*.
As anticipated, the two principal energy loss processes, radiation emission and ionization/excitation collisions, dominate in two distinct energy ranges of the incoming radiation, as shown in Figure 2.1. The critical energy E_c is the energy at which the two effects contribute equally to the electron energy loss, which can be approximated as [29]:

$$E_c = \frac{550}{Z}[MeV].$$

This expression is valid, within 10%, for absorbers with $Z \geq 13$.

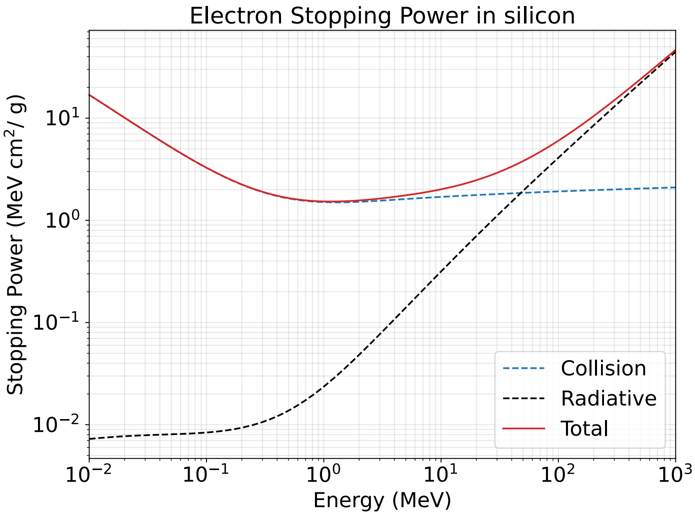

Figure 2.1: Electron stopping power as a function of energy in silicon. Data from [30].

To conclude, another important concept in electron-matter interaction is linear energy transfer (LET), which refers to the amount of energy deposited by ionizing radiation in matter per unit distance. LET is particularly relevant in radiobiology, where it is used to distinguish between the effects of different types of ionizing radiation at subcellular scales. The unit of LET is commonly expressed in keV/μm. Radiation with higher LET, like alpha particles and protons, typically has a greater biological impact than radiation with lower LET, such as photons and electrons.

2.2 Electrons in Radiotherapy

Electron beams have been used in radiation therapy for several decades, particularly in the treatment of superficial tumors located within a few centimeters of the skin surface [31]. Electron-beam therapy is advantageous because it deposits a (reasonably) uniform dose in a relatively shallow depth, after which the dose falls off rapidly, eventually to a near-zero value. This characteristic depth-dose curve (Figure 2.2) makes electrons suitable for treating superficial tumors, up to approximately 6 cm from the surface for 20 MeV beams, while sparing underlying healthy tissues. The depth of treatment can be controlled by selecting the appropriate beam energy.

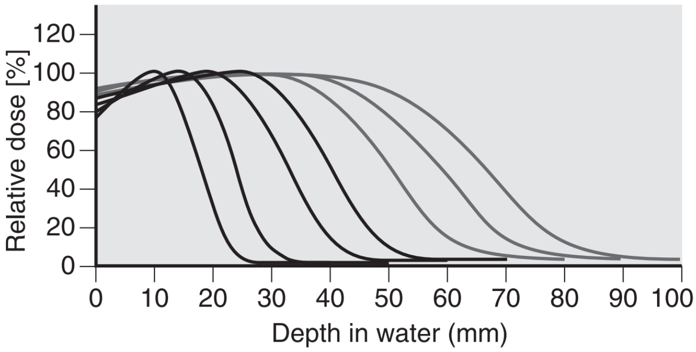

Figure 2.2: Variation of electron depth-dose curves with beam energy for (from left to right) 4, 6, 8, 10, 12, 15, and 18 MeV beams. From [32].

In addition to external beam therapy, electrons are also used in Targeted Radiation Therapy (TRT) for cancer treatment. Targeted Radiation Therapy (also known as Radiopharmaceutical Therapy, RPT) emerged in the last years as a potential approach to treating various types of tumors with minimal damage to adjacent healthy tissues [33]. TRT involves the use of radiopharmaceuticals, which are compounds that combine a radioactive isotope with a targeting molecule that selectively binds to cancer cells. When administered to a patient, these drugs are transported to the tumor site, where they bind to a specific receptor overexpressed by a tumor due to the mediation of a targeting agent. Once deposited, the radioactive decay of the radioisotope inside the radiopharmaceutical generates damaging radiation that can harm the cancer cells from within.
The radionuclides utilized in therapy and theranostics can be classified based on the type of primary emission produced during their decay, namely, α, β, and Auger emitters. The emitted particles exhibit specific ranges and linear energy transfer (LET) values, leading to different types of destructive actions on the carcinoma.

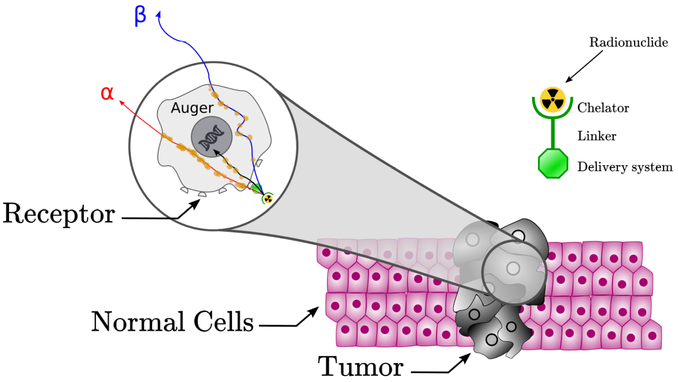

Figure 2.3: Illustration depicting the various types of internalized radiopharmaceuticals, including α-, β-, and Auger emitters, and their corresponding destructive effects on cancerous cells. From [11].

β-emitters were the first radionuclides employed in Targeted Radiation Therapy and remain nowadays the most commonly used in clinical applications. The emitted electrons have ranges of 2–10 mm and LET values of 0.1–1.0 keV/μm [34]. Figures 2.4(a) and 2.4(b) illustrate the stopping power and range of electrons in soft tissue (International Commission on Radiological Protection (ICRP) [35]), highlighting the energy range relevant for TRT applications. The low LET values result in a less damaging effect compared to α and Auger emitters, but the beta radiation is distributed over a longer range. This leads to the "cross-fire" effect, where β-emitters can not only irradiate the cell targeted by the radiolabeled drug but also harm and kill other tumor cells. Several commercial β-emitter radiopharmaceuticals are currently available, such as [^{177}Lu]-PSMA-617 [36] or Lutathera® (lutetium Lu-177 dotatate)[1] [37].

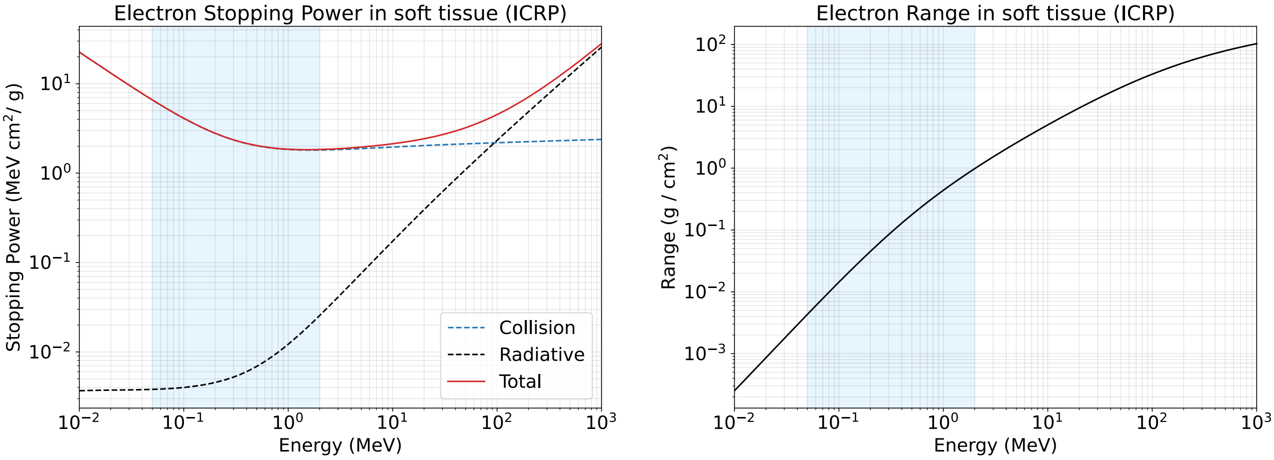

(a) (b)

Figure 2.4: Electron stopping power (a) and electron range (b) as a function of energy in soft tissue (ICRP [35]). In blue the typical energy range for β-emitters used in therapy/theranostics. Data from [30].

As previously mentioned in Section 1.2, the objective of ISOLPHARM is to develop a radiopharmaceutical molecule incorporating ^{111}Ag radionuclide. This isotope is typically generated via neutron capture of ^{110}Pd in a nuclear reactor, resulting in significant levels of contamination [21]. The ISOL technique enables high-purity production of ^{111}Ag, providing an opportunity to develop a radiolabeled drug with maximized radionuclide deposition. Since the number of receptors on the cell surface is limited, the therapeutic effect decreases as the number of receptors occupied by cold isotopes increases. Therefore, the ability to produce pure radioisotopes increases the number of receptors occupied by ^{111}Ag, thereby enhancing the drug's therapeutic performance. Although the structure and composition of the radiolabeled drug proposed by ISOLPHARM are still being optimized, the preliminary results offer a hopeful outlook for the future.

2.3 Imaging techniques

In the field of Targeted Radiation Therapy, it is essential to assess the deposition and effectiveness of radiopharmaceuticals used in the therapy. The spatial distribution of a radiolabelled drug can be visualized by exploiting specific medical imaging systems. In particular, digital imaging techniques offer the capability to produce detailed images of the radiopharmaceutical deposition, enabling a better

---

[1] https://www.novartis.com/

understanding of the localization and behavior of the analyzed drug. In the context of ISOLPHARM, testing the expected prototype drug deposition is a fundamental step in the development of a complete radiopharmaceutical and represents one of the primary objectives of the project.
In order to efficiently deal with a digital imaging system, full knowledge of the principles behind image digitization and tools used to assess image quality is required.

2.3.1 Digital imaging

Medical and biological imaging applications often require the visualization of physical quantities such as radiation or molecular interactions in tissues and cells. To achieve this, researchers rely on digital images, which are created by converting continuous analog signals from sensors or detectors into discrete digital signals using a process of sampling and quantization. Greyscale images, in particular, are widely used in medical imaging to represent the magnitude of a physical quantity at each point in a two-dimensional space.
A greyscale image can be described as a function of two dimensions $f(x, y)$, where x and y are spatial coordinates and the value of f at any point (x, y) represents the intensity (gray level) of the image in that point. A digital image involves finite values both for the coordinates (x, y) and for the intensity level (f). The physical meaning of the scalar quantity f at a given (x, y) is determined by the source of the image. To create a digital image, the continuous image is sampled into a discrete image with M rows and N columns; in this case, x and y are integer values ranging from 0 to $M - 1$ and 0 to $N - 1$, respectively. The intensity f is discretized in a defined number of levels L that represents a power of 2, *i.e.* $L = 2^k$ (where k is an integer). The discrete levels are equally spaced and they are integers in the range $[0, L - 1]$. The process of discretization of the coordinate values $(x,\ y)$ is defined as sampling while the digitization of the input signal amplitude values (f) into intensity values is defined as quantization. When a sensing array is used for image acquisition, the number of pixels in the detector array determines the limits of sampling in both directions [38].
There are three ways to represent the digital image (schematized in Figure 2.5) and the numerical array is the one used for computer processing. The numerical array is a matrix composed of the numerical values of $f(x, y)$ ($\in [0, L - 1]$) for each discrete coordinate (x, y) and can be represented as a M×N array.

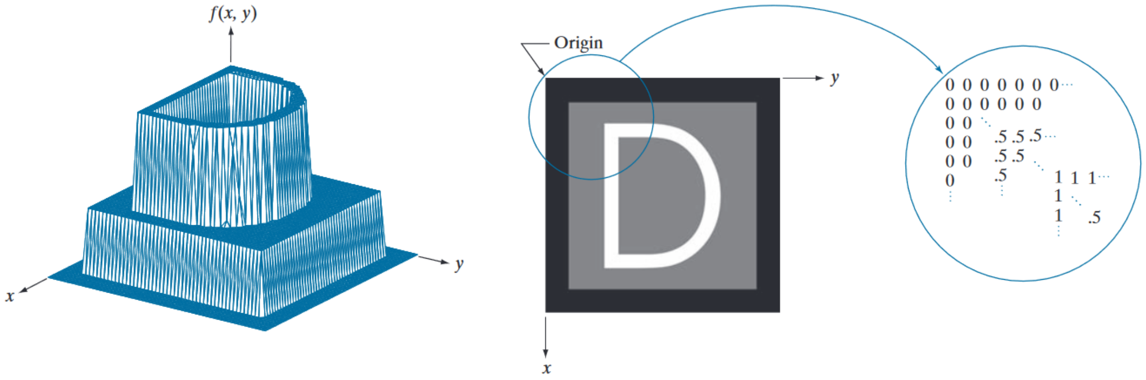

Figure 2.5: Different digital image representations (as a surface, as a visual intensity array, as a 2-D numerical array). From [38].

2.3.2 Spatial resolution

The resolution is the capability of an imaging system to distinguish two neighboring structures as separated, resolving fine details of the object being studied [39]. The spatial resolution specifically refers to the resolution of the imaging system in the spatial domain, *i.e.* the resolution in the x and

y dimensions of the image. Spatial resolution can be measured in different ways depending on the application of the imaging system (whether a detector or a complete system). A common approach used to analyze this quantity is the characterization of the system's representation of an object with known geometry. Two examples of this approach are the point spread function (PSF) and the line spread function (LSF). The PSF is a mathematical function that describes how an imaging system blurs a point source of light, describing the distribution of light around the spot and how it varies with position in the image. Similarly, the LSF describes the response of an imaging system to a thin and long line object.

A normally employed and simplified method for estimating the system's resolution using these functions involves analyzing specific quantities that characterize the PSF and LSF behavior. The full width half maximum (FWHM) and the full width at tenth maximum (FWTM) are two parameters widely used to represent the resolution of an imaging system, describing in one parameter the width of the profile. The FWHM is a measure of the width of a peak or pulse function at half its maximum amplitude, computed as the distance between the two points where the signal reaches half of its maximum amplitude. The relation for a normal distribution between the FWHM and standard deviation σ is [40]

$$\mathrm{FWHM} = 2\sqrt{2\ln 2}\sigma.$$

The FWTM is similarly defined as the width of the function at 1/10 its maximum amplitude. Figure 2.6 graphically represents each of these quantities for a Gaussian distribution.

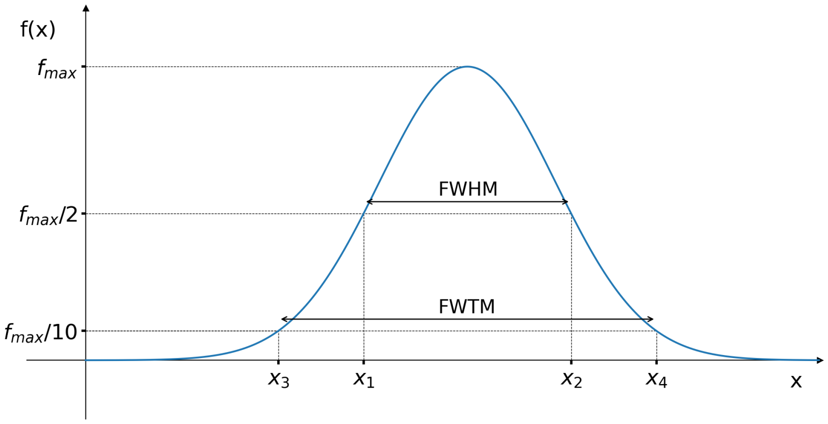

Figure 2.6: Graphical representation of the FWHM and FWTM for a normal distribution.

To evaluate the spatial resolution of an imaging system, the FWHM (or the FWTM) of the produced point spread function is considered as a direct measure of resolution. Nevertheless, these two parameters do not provide any information about a possible asymmetry in the response, so that LSFs or PSFs can have different shapes and still present the same FWHM. The FWHM is thus a rapid resolution measure, ideal to analyze how a point-like source is imaged by the system but does not provide a full understanding of the system's capabilities [40].

There are also definitions of spatial resolution that are based on the separability between two objects. The Rayleigh resolution criterion provides a definition for evaluating if two point-like objects are resolved [41]. The criterion states that two point sources of light can only be distinguished if the peak of one point spread function falls on the first intensity minimum of the other PSF, as illustrated in Figure 2.7. A rigorous application of this criterion would require the two point-like sources to be monochromatic and of equal intensity, although in different experimental applications these conditions may not be met: the Rayleigh criterion can anyway serve as a general tool to determine whether the imaging system is capable of resolving a specified separation distance.

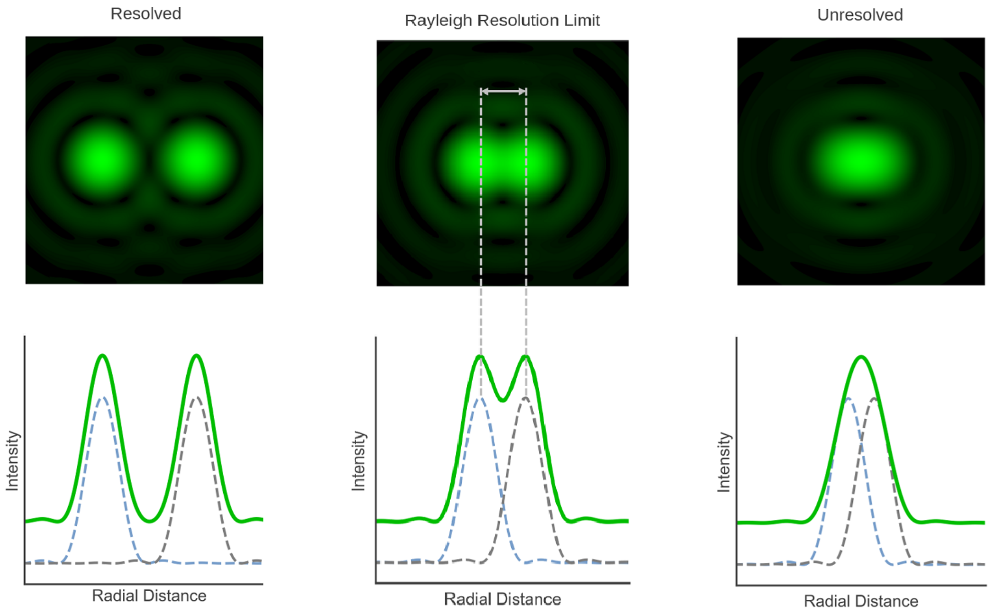

Figure 2.7: Overlap of 2D point-like spread functions: comparison between resolved, unresolved and Rayleigh limit images. From [42].

At the Rayleigh limit, it can be proved that the sum function of the two point spread functions has a defined ratio between the intensity at the mid-point (I_{mid}) to that at the maximum (I_{max}), equal to [41]

$$\frac{I_{\text{mid}}}{I_{\text{max}}} = \frac{8}{\pi^2}.$$

2.3.3 Contrast

Contrast resolution measures the capability of an imaging system to distinguish an object from its surrounding area or background [43]. It is evaluated based on the difference in intensity between the object and the surrounding area, so that contrast depends on the number of intensity levels that an observer can perceive for a given display [41]. A low-contrast image can make it difficult to distinguish objects from their surroundings, reducing the ability to detect them clearly (as shown in Figure 2.8).

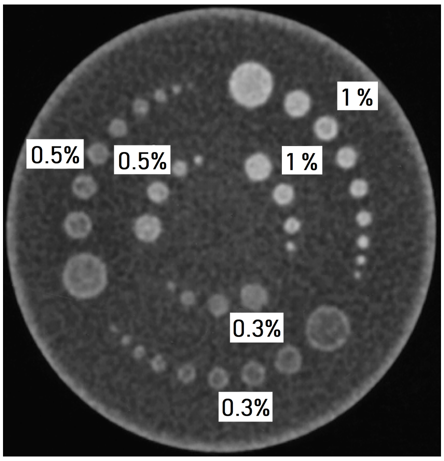

Figure 2.8: Catphan® 600 phantom used to compare different contrast coefficients in CT image. The figure illustrates different objects with specific contrast (1%, 0.5%, and 0.3%) with respect to the background. From [44].

The contrast between an object in a region A and its surrounding background B can be defined as [43]:

$$\frac{I_A - I_B}{I_A + I_B},$$

where I_A and I_B represent respectively the intensity of region A and B.

2.4 β-imaging for cell cultures

Radionuclide imaging refers to the process of producing an image that displays the distribution of radionuclides in biological samples, up to the single-cell level. These imaging techniques offer the possibility to visualize and investigate metabolic processes within live and intact cells, such as normal cell developmental processes and abnormal behaviors [45]. Radionuclide imaging also represents a fundamental tool for the visualization of the deposition of radiopharmaceuticals in cell cultures, allowing for experimental assessment of their selectivity and localization.

β-imaging is a technique that specifically aims to visualize the distribution of a β-emitting radiotracers internalized by biological samples by detecting the electrons released in the decay of the radioisotope. Due to the limited penetration depth of electrons, β-imaging is only suitable for applications that involve cell cultures or thin sections of tissues (a few hundred of μm), while other techniques should be utilized for thicker samples [46].

The requirement for a thin sample is also necessary to avoid the deterioration of the intensity and spatial information in the outcome image. As radiotracers are positioned deeper within the sample, the electrons emitted in the β decay lose more energy and scatter more frequently in the sample medium. As a consequence, the radioactivity measured at the surface diminishes while the cross-section of the emission volume increases, as depicted in Figure 2.9. This depth-dependent behavior has a direct impact on the resolution of the imaged radiotracer: the farther the source is from the imaging system, the less intense and wider its representation becomes.

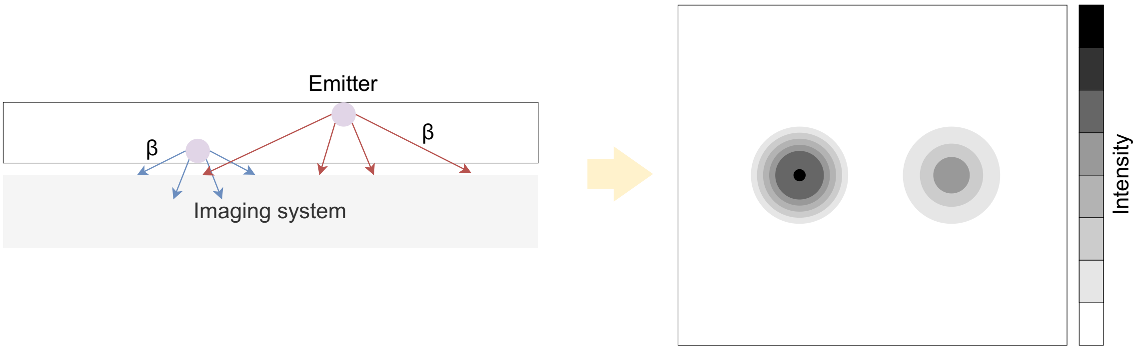

Figure 2.9: Two point beta sources placed in a sample volume. The released electrons scatter and propagate inside the volume. Two identical sources give different surface radioactivity depending on the distance between their location and the detector (left). As a consequence, the most distant source from the imaging system produces a broader and less intense signal (right).

There are two main approaches for β-imaging: direct and indirect. Direct β-imaging is explained in Section 2.5: in this method, the electrons emitted from the radiotracer are directly detected by a sensor placed in close proximity to the sample. Indirect imaging techniques, on the other hand, uses scintillators to convert the emitted beta particles into photons, which are then detected by a camera or other imaging devices; this approach is described in Section 2.6.

2.5 Direct β-imaging

Direct β-imaging comprises two distinct approaches: *autoradiography*, which relies on the use of photographic nuclear emulsions to record the beta particles emitted by the radiotracers, and the use of external detectors, which employs specialized devices to detect the released radiation (typically, gaseous detectors). Section 2.5.1 deepens the autoradiography technique, while the application of radiation detectors to β-imaging in cell cultures is described in Section 2.5.2.

2.5.1 Autoradiography

Autoradiography was the first β-imaging technique to be developed and today still represents a widely utilized option for radionuclide imaging. Autoradiography has often been employed to qualitatively visualize the cellular and subcellular distribution of radiolabeled compounds in biological tissues or cell cultures: the application of this method for cellular-level imaging is specifically referred to as microautoradiography.

Autoradiography detects the electrons emitted by the internalized radionuclides exposing a photographic emulsion or film that is placed in close proximity to the sample. This technique provides a high-resolution visualization of the spatial distribution of radiotracers, making it a valuable tool for various applications in biological research [46]. Figure 2.10 illustrates an example of a microautoradiography application.

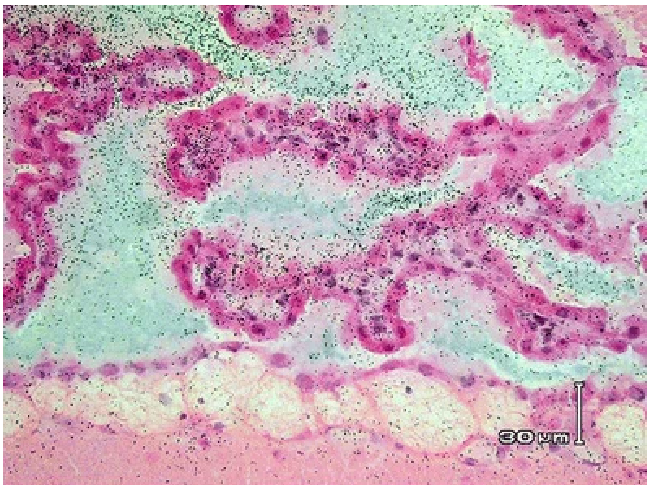

Figure 2.10: Example microautoradiography ^{14}C-azidothymidine in rat brain choroid plexus after an intravenous administration. The location of the drug-derived radioactivity is made apparent by the black specks that appear over the section. From [47].

Radionuclides that emit low-energy beta particles without accompanying gamma or X-ray radiation are traditionally preferred for autoradiography. Lower-energy isotopes emit electrons that have a short range (few μm), producing a highly localized signal that improves the resolution of the image. On the other hand, high-energy β-emitters can penetrate deeper into the tissue, allowing for thicker samples but resulting in a broader signal. The most employed β-emitters consist of isotopes of elements commonly found in biological tissues, such as ^{3}H, ^{14}C, ^{35}S [46].

Autoradiography can be performed using two types of emulsion: silver-based and phosphor-based. The choice of which one to use depends on the specific application and experimental design.

Silver-based emulsions offer potential high spatial resolution but require long exposure times and complete darkness to avoid exposure to light. These photographic emulsions consist of silver halide crystals (usually silver bromide or silver chloride) suspended in a gelatin matrix. When the emulsion is placed in contact with the radioactive sample, the beta particles penetrate the emulsion and interact with the silver halide, causing its ionization. The ionization leads to the reduction of the silver ions to metallic silver atoms, which can aggregate and form dark clusters within the emulsion, as illustrated in Figure 2.11. After exposure, the emulsion is developed using a series of chemical baths, which fix the metallic silver clusters in place and remove the unexposed silver halide crystals. The silver clusters will appear as dark spots on a light background, corresponding to the areas of the sample that have accumulated the radiotracer.

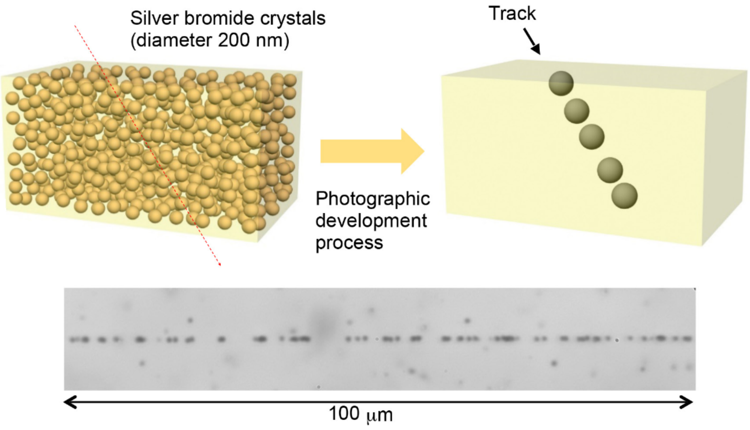

Figure 2.11: Schematic representation of a silver-based emulsion layer. The gelatin matrix contains dispersed silver bromide crystals (left). During the photographic development process, silver grains align along the path of the charged particle (right). At the bottom is an example of an optical microscopic photograph captured using the emulsion. From [48].

Autoradioluminography is a technique that exploits the properties of phosphor screens to perform autoradiography. Phosphor screens consist of a thin layer of phosphor crystals deposited on a support, typically made of aluminum or plastic. When a beta particle penetrates the phosphor layer, it interacts with the atoms in the crystal lattice, causing the excitation of the atomic electrons. These electrons might be trapped in metastable energy levels present within the crystal lattice, where they remain until they are stimulated to return to their ground state. After the exposure to the radioactive sample, the phosphor screen is scanned by a laser beam that stimulates the trapped electrons to return to their ground state, de-exciting through the emission of photons. The emitted light is proportional to the number of trapped electrons. A photomultiplier tube or a CCD camera can detect the light and converts it into an electrical signal, which is processed to generate an image [49]. The whole process is summarized in Figure 2.12. Compared to silver-based emulsions, autoradioluminography can be reused multiple times and can produce digitized images.

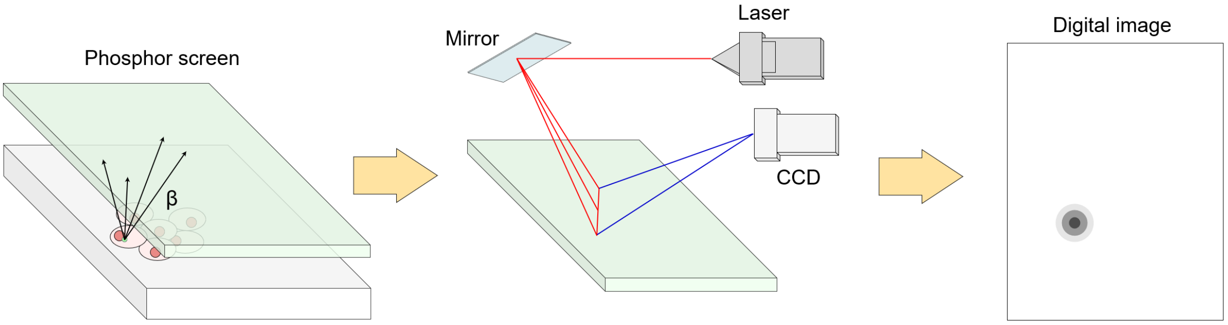

Figure 2.12: Schematized application of a phosphor screen: the phosphor is exposed to the radiolabeled sample, exciting the atomic electrons in the crystal (left); the screen is scanned with a laser beam, leading to the emission of optical photons that can be detected by a camera (center); the captured light can be digitized and produce an image (right).

2.5.2 Gaseous detectors for β-imaging

Gaseous detectors have been extensively used for radiation detection, as they are one of the earliest and most traditional types of particle detectors. In direct β-imaging, gaseous detectors have been employed to achieve good spatial resolution and fast response times.

Parallel plate avalanche counters (PPACs) are widely used in autoradiography. PPACs are gaseous detectors mainly employed in particle tracking and time-of-flight measurements. The basic design of a PPAC consists of two parallel electrodes with an intense electric field applied between the two. The incident radiation can ionize the gas present inside the chamber volume, releasing atomic electrons in the medium. The secondary electrons are accelerated under the electric field until they ionize the gas themselves, creating an avalanche effect [50]. Parallel plate avalanche counters are generally designed to achieve bidimensional position information: the PPAC electrodes are segmented into orthogonal narrow stripes, so that the particle crossing position is inferred from the ratio of the pulse-height amplitudes measured at each end of each strip (after being amplified and shaped) [51]. In some cases, the PPAC design can feature a central electrode and two additional electrodes which are responsible for the X and Y measurement. Only these two electrodes are divided into stripes, which may be oriented at an angle relative to each other. Each strip acquires part of the induced charge so that the centroid of the charge distribution can indicate the crossing position, similar to the standard PPAC design [52]. Figure 2.13 schematizes this design.

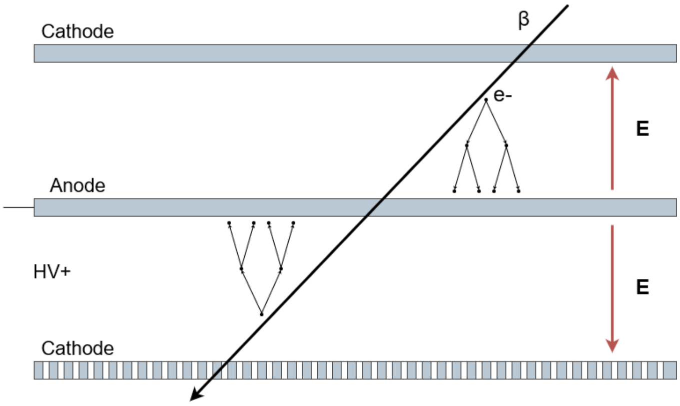

Figure 2.13: PPAC operational principle. Inspired from [52].

One of the most used instruments that apply the gaseous detectors to autoradiography is the BetaIMAGER tRACER™ (produced by Biospace Lab[2]). The BetaIMAGER tRACER is a digital autoradiography system based on a parallel plate avalanche counter that provides real-time imaging of low-energy β-emitting (and eventually α-emitting) isotopes with high resolution (50 μm). Its design is derived from experiments conducted at the CERN laboratory: to simplify the electronic system, the gas mixture in the PPAC is combined with a vapor of triethylamine (TEA) [53]. This vapor is electroluminescent in the UV spectrum, causing the scintillation of the avalanche as it develops. As a result, a small UV light spot is created by each beta particle, which can be captured by an intensified CCD camera. The video signal is then digitized and it is possible to calculate the center of gravity of each spot to determine by approximation the emitting point [46]. Figure 2.14 shows a sample image obtained with this instrument.

---

[2] https://biospacelab.com/

Figure 2.14: Kidney section (20 μm thick) of a rabbit injected with a renal tracer, 99mTc-DMSA. The distribution of radioactivity was obtained with BetaIMAGER tRACER. From [54].

More recent advances in gaseous detectors have led to the development of micromesh-based detectors. Micropattern gas detectors (MPGDs) are widely adopted in high-energy particle experiments and are recently being applied to imaging applications. MPGDs can provide thinner structures (typical distances of 0.1 mm between the electrodes) and higher electric fields (up to 30 kV/cm) compared to traditional PPAC detectors. The increased electric field in MPGDs leads to a higher amplification gain per unit distance compared to PPACs. As a result, micropattern gas detectors can achieve equivalent amplification factors in thinner geometries [46].

There exists a wide variety of micropattern gas detectors with different designs and configurations. MPGDs mainly consist of two parallel electrodes filled with a gas-quencher mixture. This volume includes a set of micro-patterned structures, which can be made up of micro-strips, micro-holes or micro-meshes structures. Microstrip gas chambers exploit a principle analog to wire chamber, using extremely fine printed strips (100 μm) instead of wires. Micromegas similarly exploit micro-meshes to produce electron avalanches. Micro-holes base MPGDs (also called gas electron multiplier, GEM) consists of a single foil featuring a regular pattern of closely spaced holes: when a voltage is applied between the top and bottom electrodes of the GEM, the created dipole field is strong enough inside the holes to allow for gas amplification [55], [56]. Figure 2.15 illustrates the operational principle of a Micromega detector.

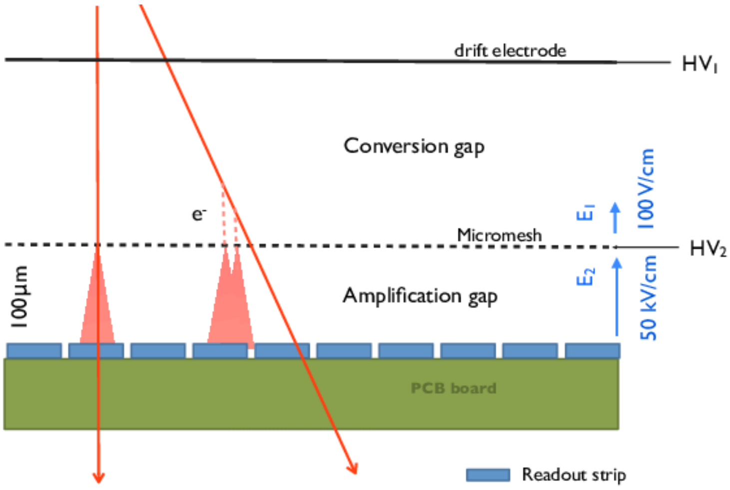

Figure 2.15: Micromega detector operational principle. From [57].

A recently developed device that utilizes MGPD technology for alpha and beta particle imaging is the BeaQuant™ (produced by AI4R company[3]). This instrument provides high resolution and the possibility for fast measurements.

2.6 Indirect β-imaging

2.6.1 Radioluminescence Microscopy

Radioluminescence microscopy (RLM) is an indirect β-imaging technique. This approach provides the capability to visualize the uptake of molecules at the single-cell level by incorporating β- or α-emitting radionuclides.

RLM utilizes a scintillating crystal placed in close proximity to the sample to convert the energy of the ionizing radiation from radioactive β-decay into optical photons. Depending on the specific application, the scintillator can be placed in different positions. A common approach is to grow the cells in an imaging dish, laying the crystal on top of the cells. Alternatively, the cell culture can be grown directly on the scintillator plate itself to enhance the adhesion to the biological sample and thus the imaging performance. The visible-range light produced by the scintillation can be detected using a fluorescence microscope, focusing its objective on the edge of the scintillator plate and as close to the cells as possible [58]. The performance of radioluminescence microscopy relies on the crystal employed: a common choice is cadmium tungstate ($CdWO_4$), which provides high stopping power due to its dense material and optimal light yield [59].

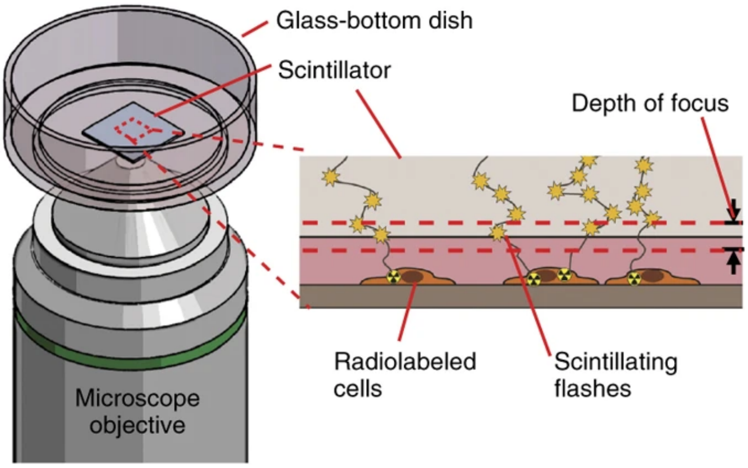

Figure 2.16: Radioluminescence microscopy. From [58].

RLM can outcome an image integrating the total scintillation light produced during a long exposure ($\sim$ 100 s). With the integration approach, the individual scintillation flashes overlap, providing a semi-quantitative measurement that can anyway allow for a rapid assessment of the radioactivity distribution. To obtain better resolution and a fully quantitative image, it is possible to singularly acquire multiple frames of the singular scintillation flashes (each one corresponding to a single β-decay). The frames can be thus processed by exploiting an ad hoc algorithm capable of localizing where the radioactive decay took place based on the position and shape of the corresponding scintillation flash. This technique is known as Optical Reconstruction of the Beta Ionization Track (ORBIT) [60].

Compared to other autoradiography methods, RLM has smaller dynamic range and lower sensitivity but can offer spatial resolution a up to 50 μm [60]. The radioluminescence microscopy technique has been utilized over the last years to image metabolism, proliferation and drug binding in individual cells (commonly in cancerous cells). Figure 2.17 shows a sample image of a radiopharmaceutical ([^{18}F]FDG,

---

[3] https://www.ai4r.com/

commonly used in PET exams) distribution in a cell culture, obtained using RLM.

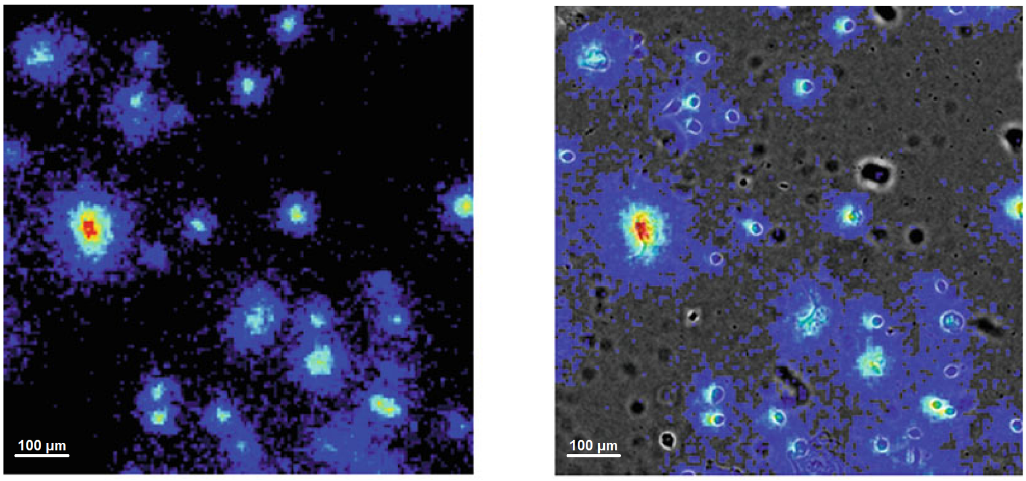

Figure 2.17: A reconstructed sample radioluminescence image (top left) and (top right) the same image overlaid onto brightfield image showing co-localization of [^{18}F]FDG uptake to individual MDA-MB-231 cells. From [45].

Chapter 3

Experimental setup and methodology

3.1 The ISOLPHARM detector for β-imaging

Within the ISOLPHARM collaboration, the Padova group is developing a novel cost-effective instrument to detect beta activity on different types of cell cultures with high spatial resolution. The implementation of this device will exploit a set of ALPIDE chips, Monolithic Active Pixel Sensors (MAPS) designed for the inner tracking system of the ALICE (A Large Ion Collider Experiment) detector at the Large Hadron Collider (LHC), at CERN Laboratories [61]. The beta detector will be made up of four or more ALPIDE devices arranged in a compact planar geometry, to suitably adhere to the cell culture surface and provide 2-dimensional activity images. The detailed structure and design of the beta detector will be further discussed in Chapter 4, which focuses on the description of the simulated system.

In order to understand the design and operation of the described beta detector, the following section will provide a comprehensive description of MAPS detectors and their underlying detection mechanism. Following this brief introduction, a detailed characterization of the ALPIDE chip and its key components will be presented in Section 3.1.2.

3.1.1 MAPS detectors

In the 1980s, silicon semiconductor systems and read-out electronics based on CMOS technology revolutionized the implementation of vertexing and tracking detection in high-energy physics experiments, fulfilling essential requirements in terms of granularity, material thickness, read-out speed, power consumption, and radiation hardness. Nowadays, silicon pixel sensors are widely used in this field, although they often require an interface between the sensor and the read-out electronics, as in the case of the majority of innermost layers of the Large Hadron Collider (LHC) experiments [62]. To construct detection systems with higher granularity and less material thickness, it was necessary to introduce a novel technology, that could integrate both sensor and read-out electronics into a single detection device. This demand was met by Monolithic Active Pixel Sensors (MAPS).

Monolithic Active Pixel Sensors are a type of silicon particle detector that has gained significant attention in the field of particle physics in recent years. Their high spatial resolution, efficiency, low power consumption, and low cost have made them a widely adopted choice for particle tracking in high-energy physics experiments. However, the advantages of MAPS extend beyond just high-energy physics and they have the potential to be utilized in a wide range of applications. The ability to precisely measure the location and intensity of incident radiation makes MAPS appealing in imaging applications [63], [64].

One of the main advantages of MAPS is their high spatial resolution, which can reach up to tens of micrometers [61]. Because each sensor is composed of an array of small pixels (for the ALPIDE, with dimensions as small as ≈ 30 μm [61]), these devices can provide extremely fine-grained measurements of the position of charged particles passing through the detector, making them particularly well-suited for precise position measurements. MAPS are also highly efficient and have a very low power consumption. Finally, because MAPS are made using standard semiconductor fabrication techniques, they can be produced at a relatively low cost compared to other types of detectors. The main constraints of MAPS are generally the limited radiation tolerance and moderate read-out time, due to its charge collection mechanism.

A MAPS detector integrates all the necessary electronics for signal amplification and readout, making it a highly compact sensor. Figure 3.1 displays a cross-sectional view of the ALPIDE chip, which effectively illustrates the typical structure of a MAPS detector divided into its three main components. The substrate layer is a highly doped layer that provides support and mechanical stability to the detector. The epitaxial layer is a thin, lightly doped p- layer grown on top of the substrate layer using the epitaxy process. Highly-doped n-wells are implanted on the upper surface of the device and create small, confined depleted regions around themselves (the white regions in Figure 3.1). The purpose of the n-wells is to collect the charges generated by ionizing particles. Specifically, only the electron-hole pairs produced within the epitaxial layer contribute to the signals detected by the implanted n-wells, while those generated in the substrate layer are not collected. The yielded charge is collected by diffusion within the epitaxial volume and later by drift within the depleted region. The diffusion process significantly slows down the collection mechanism, resulting in an increased recombination probability inside the crystal and a consequent loss of the signal charge. This collection mechanism exhibits limited radiation tolerance and leads to a slow signal [65]. To enhance the spatial resolution of the MAPS, the depletion region is segmented into multiple wells, each corresponding to a pixel in the sensor array.

The generated signal is directly processed by the readout electronics, which are located on the same silicon substrate in the case of a monolithic design. The NMOS transistors are placed in a deep p-well in order to shield the source, drain junctions from the epitaxial layer, and prevent competition between the n-wells hosting transistors and the collection electrode n-wells.

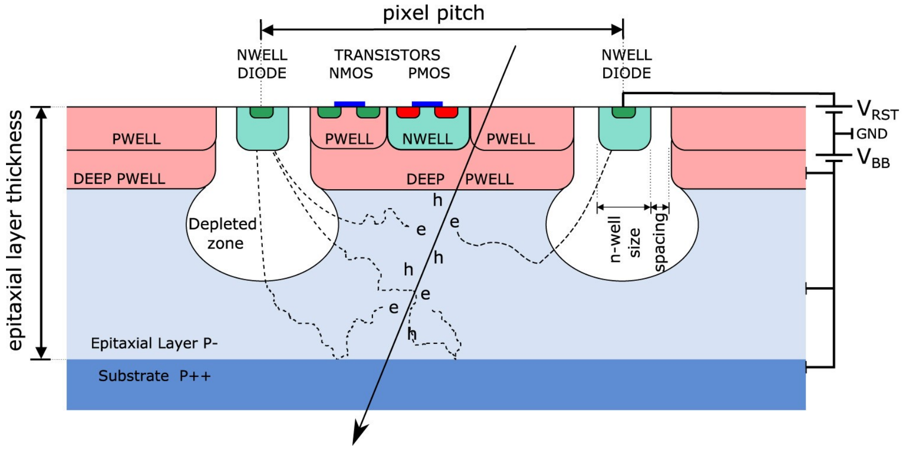

Figure 3.1: Schematic illustration of a MAPS pixel in the TowerJazz 0.18 μm imaging CMOS (used for ALPIDE) cross section and detection mechanism. From [62].

3.1.2 The ALPIDE chip

ALPIDE is a monolithic active pixel sensor designed to meet the requirements of the Inner Tracking System (ITS) of the ALICE experiment at CERN [61]. The pixel chip was developed by a collaboration formed by CCNU (China), CERN, INFN (Italy), and Yonsei (South Korea). The design and development of ALPIDE were carried out during the ALICE Long Shutdown 2 (LS2), with the primary objective of upgrading the detector's ITS (whose layout is depicted in Figure 3.2(a)). The upgrade aimed to enhance the detector capabilities in terms of read-out rate, radiation load, and limits on power consumption: the advancements in CMOS technology allowed these requirements to be met with the design of the ALPIDE MAPS. The compact size and low power consumption of the sensor ensured its integration into the ITS system. The high spatial resolution and fast read-out rate of the device were studied to capture particle collisions in real time. The radiation hardness of the ALPIDE was specifically tailored to withstand the high levels of radiation fluence that are present inside ALICE. Table 3.1 shows the requirements that had to be met in the realization of the ALPIDE detector [62].

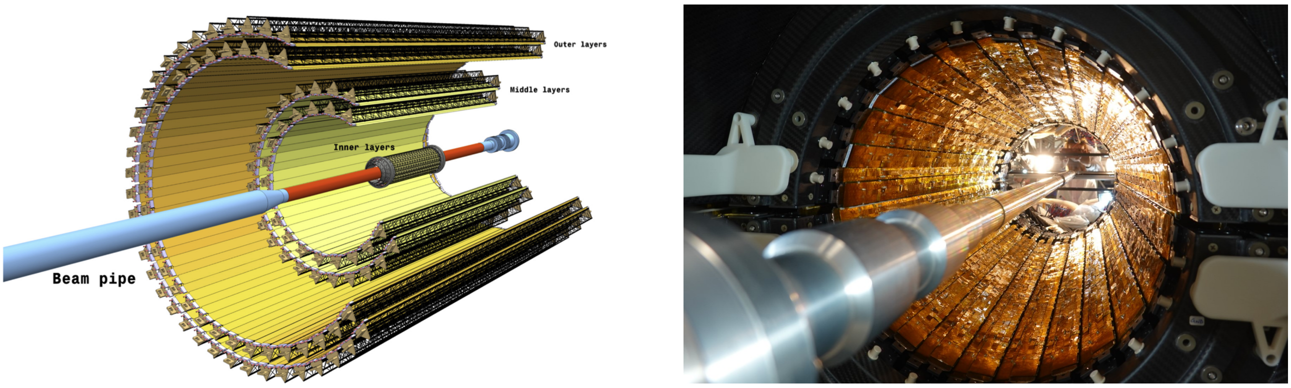

(a) (b)

Figure 3.2: (a) Layout of the ALICE Inner Tracking System upgrade. From [62]. (b) ALICE Inner Tracking Device Outer barrel. From [66].

Parameter	**IB**	**OB**
Sensor thickness (μm)	50	50
Spatial resolution (μm)	5	10
Dimensions ($r\theta \times z$) (mm^2)	15×30	15×30
Power density (mW/cm^2)	300	100
Time resolution (μs)	30	30
Detection efficiency (%)	99	99
Fake hit rate (per pixel)	10^{-5}	10^{-5}
TID radiation hardness (krad)	700	10
NIEL radiation hardness (MeV n$_{eq}$/cm^2)	10^{13}	3×10^{10}

Table 3.1: Sensor requirements for the ALICE ITS Upgrade for Inner Barrel (IB) and Outer Barrel (OB) [62]. TID = Total Ionizing Dose. NIEL = Non-Ionizing Energy Loss. TID and NIEL include a safety factor of 10.

The ALPIDE chip is 1.5 cm × 3 cm × 50 μm in size and features 512 × 1024 pixels (of size 28 μm × 28 μm) that are read out in a binary hit/no-hit fashion. Analog biasing, control, readout, and interfacing functionalities are implemented in a peripheral region of 1.2 mm × 30 mm (showed in Figure 3.3(b)).

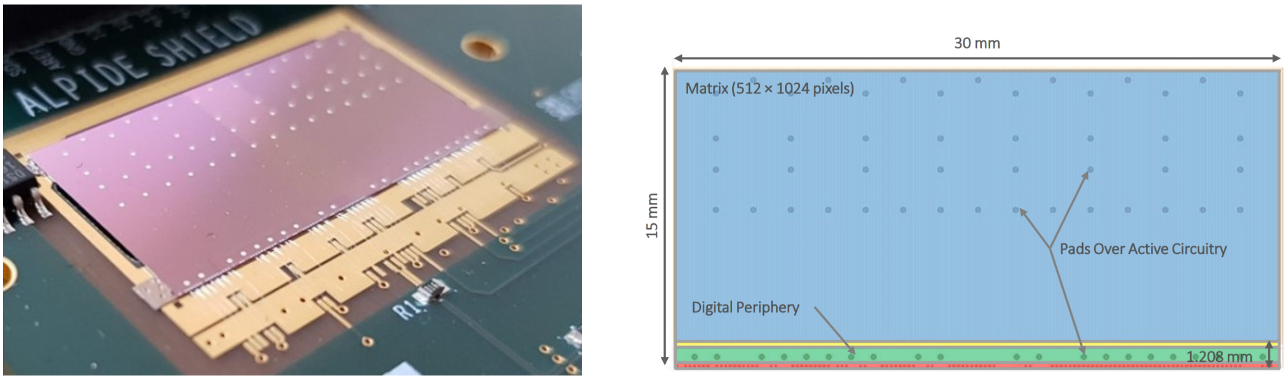

(a) (b)

Figure 3.3: (a) ALPIDE chip. From [67]. (b) The architecture of the ALPIDE floorplan. From [68].

The ALPIDE is implemented using the TowerJazz 180 nm CMOS technology for Imaging Sensors. This technology allows the production of sensors with extremely small structure sizes, as well as the fabrication of deep p-wells necessary to integrate the electronics for the first steps of signal manipulation. As explained in Section 3.1.1, the introduction of deep p-wells enables the read-out PMOS transistors to be fabricated directly onto the p-type epitaxial layer: those wells can in fact shield the n-wells hosting the transistors to prevent a loss in the charge collection. The dimensions of the final structure are illustrated in Figure 3.4(a). The substrate layer has a thickness of 14 μm, the total epitaxial layer measures 25 μm and the superficial electronics introduces a 11 μm thickness. Figure 3.4(b) presents a scanning electron microscope (SEM) image of the cross-section of the ALPIDE CMOS wafer.

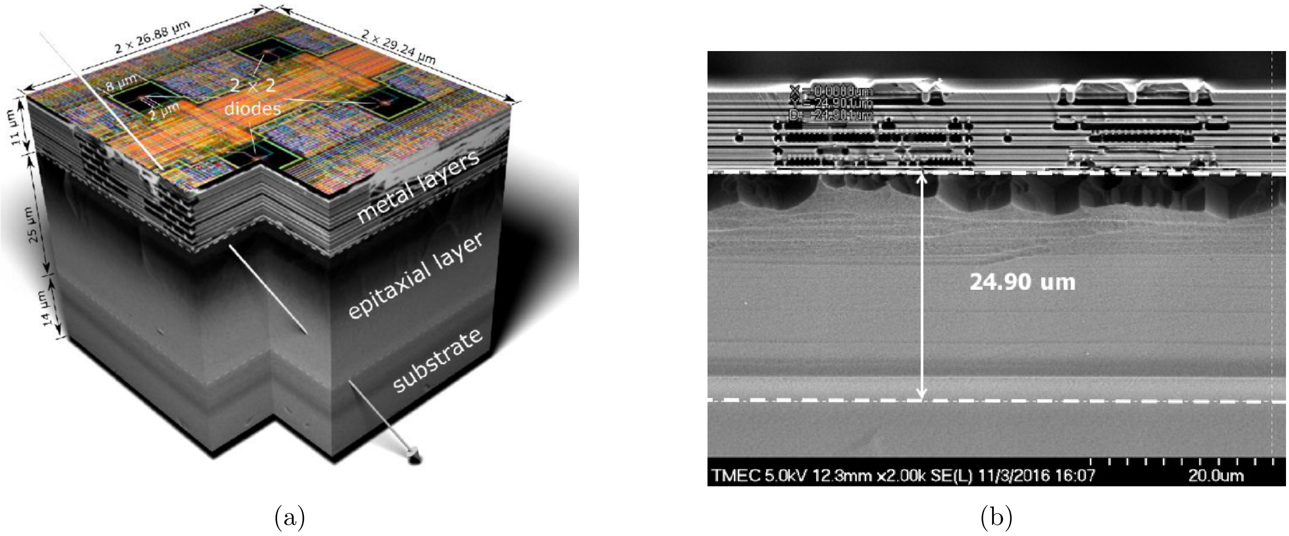

(a) (b)

Figure 3.4: (a) Cross section illustration of the ALPIDE. From [69]. (b) SEM cross-sectional image of ALPIDE chip. The epitaxial layer thickness is shown in white. From [70].

The ALPIDE sensor is segmented into 524,288 unit pixels. The individual pixel contains different parts: a sensing diode, a front-end amplifying and shaping stage, a discriminator, and a digital section. The digital section includes three hit storage registers (Multi Event Buffer), a pixel masking register, and pulsing logic. These components are shown in Figure 3.5.

The front-end and discriminator are always active and provide a non-linear response due to the transistors being biased in weak inversion. The discriminator compares the read-out signal to a pre-defined

threshold level, which is tunable and common for every pixel in the array. The front-end and discriminator act as an analog delay line, introducing a delay in the signal processing path. The delay introduced by the front-end and discriminator is designed to be comparable to the latency of an external trigger signal, so that the ALPIDE can operate in triggered mode.
In the last hit storage stage, a global STROBE signal controls the latching of discriminated hits into storage registers. If the front-end output is above the threshold and a STROBE pulse is applied to the selected cell, a pixel hit is latched into one of three in-pixel memory cells. Three distinct STROBE signals control the storage of pixel hit information in the pixel event buffers; these signals are generated at the matrix periphery and are globally applied to all pixels. The duration of the STROBE pulses is adjustable. The generation of internal STROBE signals can be triggered by a TRIGGER external command or initiated by an internal sequencer [71].

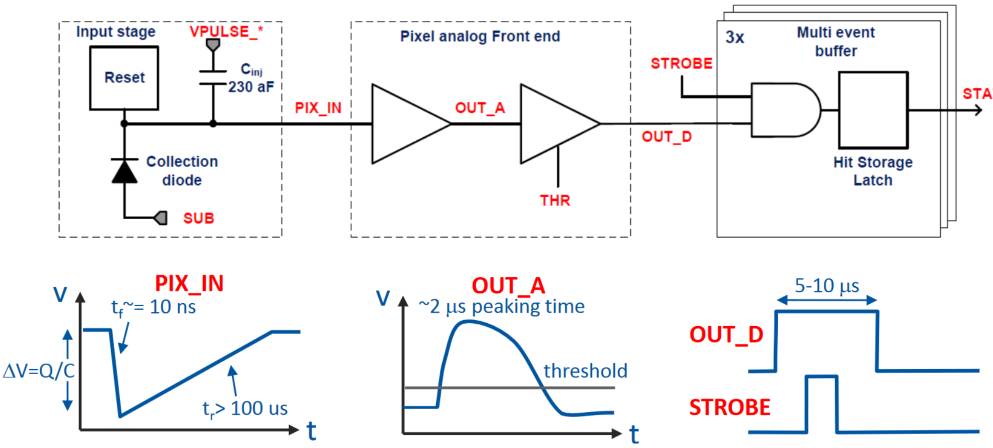

Figure 3.5: Block diagram of the ALPIDE pixel cell circuitry and relative output signals for the different blocks. From [71].

The circuit to read the pixel hit data from the matrix has 512 instances, one for every two pixel columns. It selects the first pixel with a hit in its double column based on a fixed topological priority and transmits its address to the periphery during one hit transfer cycle. The in-pixel memory element is then reset. This process is repeated until all the addresses of pixels with valid hits have been transmitted to the periphery and all the pixel state registers have been reset. The frame data transfer from the matrix to the periphery is thus zero-suppressed, so that only the addresses of pixels that have been hit are transmitted to the periphery, while the information about the pixels that have not been hit is not transferred. This way, only the necessary information is transmitted, reducing the amount of data that needs to be processed and transmitted, and improving the overall efficiency of the system. The readout of the matrix is organized in 32 regions (512 × 32 pixels), each of them with 16 double columns being read out by 16 Priority Encoder circuits. There are 32 corresponding readout modules in the chip periphery, each one executing the readout of a submatrix. The 16 double columns inside each submatrix are read out sequentially, while the 32 submatrices are read out in parallel.

3.2 Cell cultures for ISOLPHARM testing

In the context of the ISOLPHARM experiment, upcoming in-vitro experiments will be carried out to test the prototype radiopharmaceutical under investigation. The in-vitro testing phase is necessary to evaluate the deposit and selectivity of the drug in cell cultures, in particular verifying its internalization exclusively in cancer cell lines. The beta detector investigated in this thesis work will be specifically designed to assess the distribution of the developed radiopharmaceutical in various types of cell cultures. The detector's purpose is to produce a detailed image depicting the dispersion of ^{111}Ag throughout the medium and thus showing where the drug was deposited.

The ISOLPHARM collaboration is concerned with conducting in-vitro testing of the radiopharmaceutical, utilizing both traditional planar cell cultures and hydrogel-based cell cultures (which offer a three-dimensional environment for cell growth and differentiation). Each of these two distinct culture systems has its own strengths and limitations: the possibility to investigate both types of culture allows testing the behavior and effectiveness of the radiopharmaceutical in different cellular environments.

The upcoming sections present a thorough overview of these two types of cell cultures, first explaining cell culture techniques and secondly comparing traditional planar cell cultures to the more recent three-dimensional cultures.

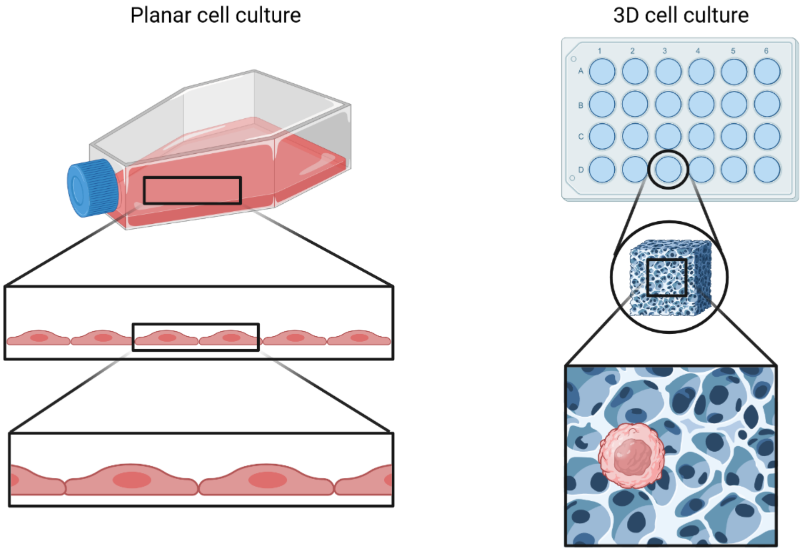

Figure 3.6: Comparison between cell behavior in 2D conventional cell culture (flat shape) and in 3D cell culture (microenvironment similar in-vivo conditions). Inspired from [72].

3.2.1 Cell cultures

Cell culture is a widely used tissue culture technique that represents the most spread-out in-vitro model. Cell cultures consist of a group of eukaryotic cells capable of growing and proliferating in a controlled environment, designed to mimic their native environment. Cell cultures have many applications across diverse scientific research fields, allowing for the investigation of different physiological and pathological processes at a cellular level. These include intracellular activity (such as replication and transcription of DNA), environmental interaction (carcinogenesis, drug action, ...), cell–cell interaction, genetics (such as genome analysis or genetic manipulation), and biotechnology applications [73]. Tissue culture was originally developed as a method to observe the characteristics and responses of animal cells without the influence of systemic factors that might occur in in-vivo experiments. The first studies on tissue cultures were carried out in the early twentieth century: the origin of tissue culture is commonly dated to 1907 and credited to Ross Harrison [74]. The first continuous human cell line was established decades later, after the introduction of antibiotics capable of supporting long-term cell cultures. The HeLa cells were the first human cells to be continuously cultured in a laboratory setting: it consisted of a line of cancer cells that were isolated by George Grey from the cervical tumor of Henrietta Lacks (HeLa) [75]. Figure 3.7 shows a representative traditional cell culture of HeLa cells.

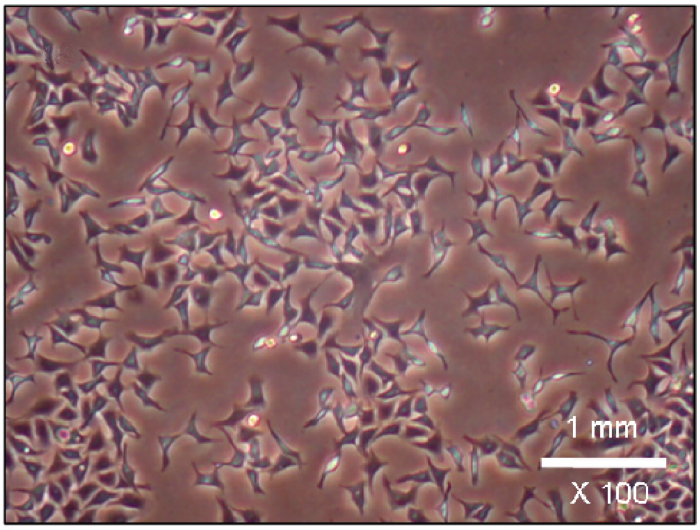

Figure 3.7: HeLa cells cultured on Petri dishes in alpha-minimum essential medium containing 10% fetal bovine serum, 10 mM ascorbic acid, antibiotics, and sodium bicarbonate. From [76].

Cell culture systems can be broadly classified into three main categories based on the method used to initiate the culture [77]:

- **primary cultures** are derived directly from excised animal tissue or organs. Primary cells preserve many characteristics of the original in-vivo cells. However, these cultures can only survive in-vitro for a limited lifespan, undergoing senescence or cell death after a certain number of divisions [77]. For this reason, they are generally only utilized in short-term experiments;
- **secondary cultures** are established by subculturing primary cells before they reach senescence. At the start of their life, secondary cell cultures present chromosomes structurally identical to those of the species from which the culture was derived [78]. Over time, the secondary cells retain some characteristics of the primary culture but might display changes over time due to genetic and phenotypic alterations. This technique extends the longevity of secondary cells, which can proliferate for a longer lifespan with respect to primary cultures [79];
- **continuous cultures** are derived from primary cultures or tissues. Continuous cell lines undergo specific genetic alterations: these modifications can override the checkpoints that regulate cell division and senescence so that the cells can be propagated indefinitely while maintaining their ability to divide and grow. These cell lines are used most often because of faster and longer growth, less nutritional requirement, and high plating efficiency [80] (on the other hand, they are frequently subject to contamination during cell propagation [68]).

In order to ensure optimal proliferation, cell cultures require specific environmental conditions, including controlled temperature, monitored pH and osmolality, a suitable substrate for cell attachment, and an appropriate growth medium. The selection of a suited cell culture medium is crucial for successful in-vitro cultivation. A growth medium is a liquid or gel specifically formulated to support the growth of cells or microorganisms. It comprises energy sources and cell cycle regulators and also helps maintain the required pH and osmolality. A typical culture medium is composed of a complement of amino acids, vitamins, inorganic salts, glucose, and serum, which represents a source of growth factors, hormones, and attachment factors [81].

During their growth phase, cell cultures can exhibit two distinct forms of growth patterns [79]. In suspension cultures, cells tend to grow either as single cells or as small free-floating clusters suspended in the liquid medium. In monolayer cultures, cells attach and grow as a single layer on the surface of a tissue culture flask or disk. The specific growth mode adopted by a cell line depends on the type of tissue from which it originated. Cell lines derived from blood (such as leukemia and lymphoma cell lines), tend to grow in suspension as they mimic the behavior of cells in the bloodstream. Monolayer growth is instead the common growth pattern for cell lines established from solid tissues, such as lung or kidney cell lines.

After the initial seeding of cells in cell culture, their growth proceeds in a predictable pattern with distinct temporal phases (shown in Figure 3.8). The standard growth kinetics of a culture cycle approximately follows a sigmoid pattern, which can be divided into different main phases [82], [79]:

- the **lag phase** is the first stage that occurs immediately after inoculation and represents the period of cell adaptation to a new environment. During the lag phase cells do not divide. The time duration of this stage is affected by the growth phase of the cell line at the time of subculture and by the seeding density;
- during **logarithmic** (or exponential) **phase** cells have already adapted to the environment and undergo rapid multiplication. The cell population increases exponentially over time. The velocity of exponential growth depends on the specific cell line under study and is regulated by the population doubling time parameter;
- the **stationary** (or plateau) **phase** is preceded by a deceleration growth phase during which the cell proliferation slows down due to nutrient depletion or toxic waste accumulation. This stress condition generally triggers the restructuring of the cells to adapt to the hostile environment. The stationary phase begins when the cellular growth rate reaches zero. Cells in the stationary phase become more susceptible to injury or damage;
- the **death** (or decline) **phase** is the final stage of the cell culture growth cycle: at the end of the stationary phase, cells undergo cell death. While some cell death might occur in the plateau phase, cell death becomes more prominent during the decline phase. In this case, cell death is a natural part of the cell life cycle and is not solely caused by a decrease in nutrient availability.

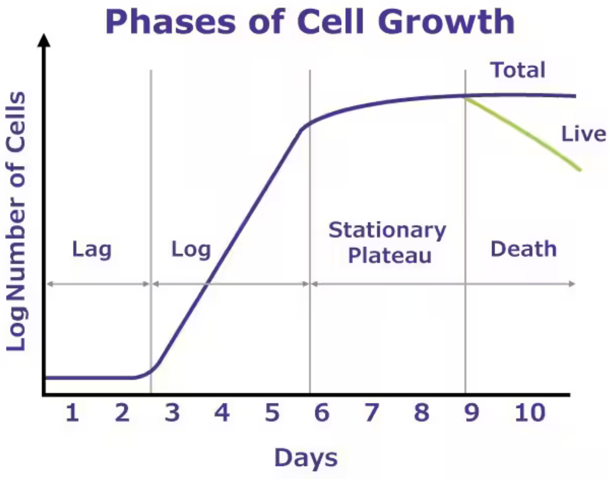

Figure 3.8: Cell culture growth curve. The plot displays the different phases of the cell culture life cycle. From [79].

3.2.2 A comparison of 2D and 3D cell culture techniques

Over the years, two-dimensional monolayer cell cultures have represented the most used method for growing cell cultures. 2D in-vitro techniques, characterized by cells adhering to a flat surface, have been extensively employed in various fields of research, including cancer biology. In two-dimensional cultures, cells grow as a single layer attached to a plastic surface, either in a culture flask or a flat petri dish. This approach provides advantages in terms of simple and cost-effective maintenance, as well as convenient functionality for conducting tests. Planar cell lines also exhibit rapid proliferation and colony formation (minutes to hours) and provide an experimental set-up that is easily reproducible [83], [84].

On the other hand, this culture method has several limitations. Many of the differences in cell behavior observed between traditional in-vitro cell cultures and their natural counterparts in-vivo arise primarily from the transition of cells from a three-dimensional structure to a two-dimensional substrate during propagation [73]. Cells in planar cultures fail to mimic the natural structures and interactions found in tissues or tumors, which can significantly impact complex biological responses. The two-dimensional geometry is unable to replicate cell-cell and cell-environment interactions present in in-vivo tissues. Moreover, the unlimited access to nutrients and other molecules in the culture medium differs from the variable availability in-vivo [85], [84].

Recognizing the limitations of 2D culture systems, there emerged a need to find alternative models that could better replicate the natural architecture of a tissue or tumor mass. This led to the development of 3D culture systems. Various three-dimensional culture methods have been developed to incorporate the spatial organization of cells: the first three-dimensional cultures were created using a soft agar solution and since then numerous different approaches have been investigated in the field.

Three main 3D culture techniques can be distinguished:

- **suspension cultures**, which seed cells on special non-adherent plates with a suitable medium (shown in Figure 3.9(a));
- cultures in **concentrated or gel-like medium**. In this type of three-dimensional cell culture cells grow in a culture medium with gelling properties, such as a Matrigel (multiprotein hydrogel) material (depicted in Figure 3.9(b));
- **cultures on a scaffold**, which is a tissue engineering term to describe a three-dimensional structure that provides support for cells to grow and organize into functional tissues, as shown in Figure 3.9(c). In scaffold cultures cells can migrate among fibres and attach to the scaffold, made of biodegradable material such as silk or collagen. Filling the space among fibers, cells can proliferate.

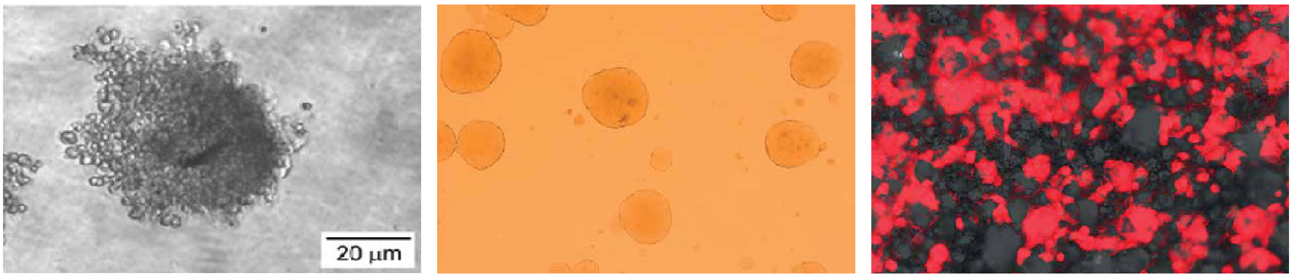

(a) (b) (c)

Figure 3.9: (a) Representative photomicrographs of orospheres arising from ALDH+CD44+Lin– and ALDH–CD44–Lin– cells cultured in ultralow attachment plates. From [86]. (b) 3D structures in soft agar. From [83]. (c) Cells (red) cultured using 3D scaffold a system with visible membrane pores. From [83].

There are some disadvantages associated with 3D cell cultures. The formation of a three-dimensional cell culture can be slower compared to planar cultures, requiring hours to days for proper formation. Additionally, the procedures involved in establishing and maintaining 3D cultures tend to be more complex, necessitating specialized techniques and equipment as well as more expensive reagents and materials. In particular, the accessibility of commercially available tests specifically designed for 3D cultures is limited, requiring the development of customized protocols.

Table 3.2 summarizes the main features of 2D and 3D cell cultures, comparing their advantages and limitations.

	2D cell culture	**3D cell culture**
Time of culture formation	Within minutes to few hours	From a few hours to a few days
Culture quality	High performance, reproducibility, long-term culture, easy to interpret, simplicity of culture	Worse performance and reproducibility, difficult to interpret, cultures more difficult to carry out
In-vivo imitation	Do not mimic the natural structure of the tissue or tumor mass	In-vivo tissues and organs are in 3D form
Cells interactions	Deprived of cell-cell and cell-extracellular environment interactions, no in-vivo-like microenvironment	Proper interactions of cell-cell and cell-extracellular environment
Characteristics of cells	Changed morphology and way of divisions; loss of diverse phenotype and polarity	Preserved morphology and way of divisions, diverse phenotype, and polarity
Essential compounds	Unlimited access to oxygen, nutrients, metabolites, and signaling molecules (in contrast to in-vivo)	Variable access to oxygen, nutrients, metabolites, and signaling molecules (same as in-vivo)
Maintaining costs	Cheap, commercially available tests and the media	More expensive, more time-consuming, fewer commercially available tests

Table 3.2: Comparison of 2D and 3D cell culture methods [83].

Chapter 4

Geant4 Simulation

4.1 Geant4 toolkit

Geant4 (GEometry ANd Tracking 4) is an object-oriented open-source simulation toolkit designed for modeling the passage of particles through matter. Geant4 provides a comprehensive set of software components that can be employed to simulate a wide collection of settings, ranging from basic geometries and phenomena to full-scale detector setups. Geant4 has different application areas, including high energy and nuclear physics, medical physics, accelerator beamline design, and the evaluation of space radiation effects on satellites and planetary bodies [87]. The first version of the Geant4 tool, released in 1998, was developed to enhance its predecessor, Geant3, in response to the demand for more precise Monte Carlo simulations of physics processes within particle detectors [25]. In the following years, several upgraded versions were introduced to increase the accuracy and performance of the software.

Geant4 is written in C++ programming language and was built upon an object-oriented programming paradigm. Thus, the different components of a simulation are encompassed in objects that can interact with one another. This design choice allows users to customize and assemble their simulations according to their specific needs.

Figure 4.1: Geant4 logo. From [87].

Geant4 provides a set of predefined classes designed to address the main aspects involved in the passage of particles through matter (Figure 4.2 collects these classes and their utilization). The software evaluates several key domains, including [25]:

- Geometry and materials: the software provides functionalities to define the shape, size, placement, and composition of the modeled objects;
- Particle interaction in matter: the toolkit can simulate the interactions of particles as they traverse different materials using sophisticated algorithms and physics models;

- Tracking management: GEANT4 includes classes to monitor the trajectories of particles as they move through the simulated materials, keeping track of their positions, momenta, and other parameters;
- Digitization and hit management: GEANT4 allows for the conversion of physical interactions within the simulation into a response from particle detectors. It specifically provides tools for the management of the recorded hits, so that the simulated data can be consistent with the one experimentally achievable;
- Event management: the software includes ad hoc methods to manage simulated events that involve multiple particles, handling all the information coherently;
- Visualization: GEANT4 offers a visualization framework to graphically represent the detector geometries and the simulated data, in an interactive way;
- User Interface: The toolkit facilitates the user interaction to configure simulation parameters, execute commands and extract results. GEANT4 includes command-line interfaces, graphical user interfaces (GUIs), and scripting interfaces.

In summary, GEANT4 allows users to create complex geometric models with components of specific shapes and materials, specifically defining the sensitive elements that record information required for simulating detector responses. The generation of primary particles can be controlled and the software provides a large set of physics processes to model particle behavior, offering the flexibility to select from different approaches. The toolkit also offers different user interfaces for interaction and visualization.

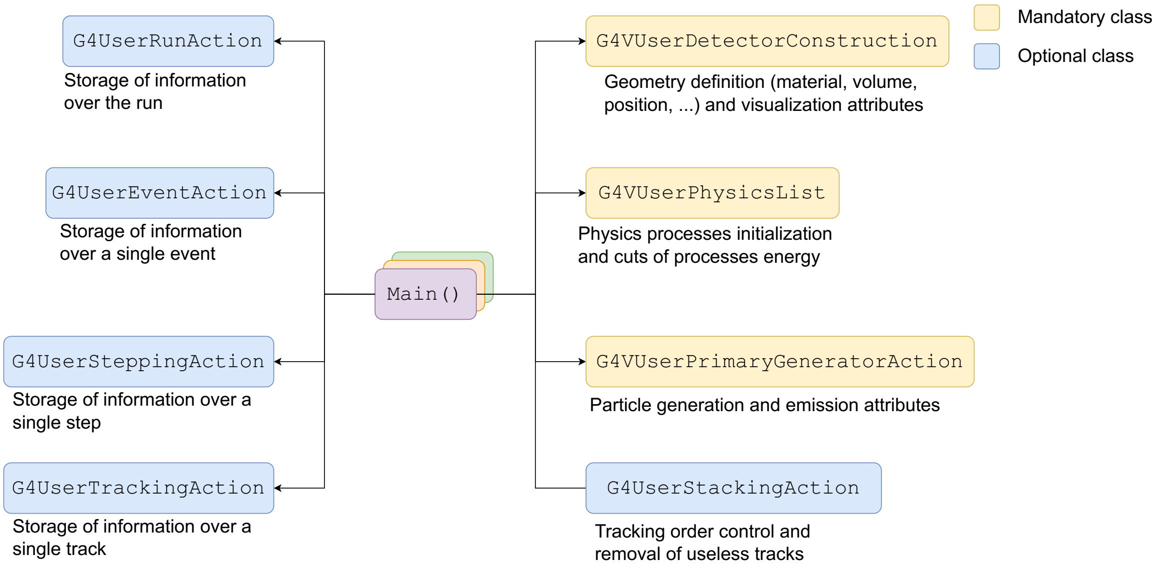

Figure 4.2: Mandatory and some optional classes needed by a GEANT4-based application. Inspired from [88].

4.2 Physic processes in Geant4

The GEANT4 toolkit presents the possibility to include a wide variety of complementary physics models that describe the physics of photons, electrons, muons, hadrons and ions from 250 eV up to several PeV [25].

In GEANT4, particles interact with materials through a series of steps, which are the basic length unit in the transportation process. During the transportation process, various physical processes co-work along the particle's step, performing interactions and calculations. The transportation process is implemented as a looped process consisting of the following stages:

1. A particle is generated and "transported" through the simulation;
2. Each process associated with the particle proposes a geometrical step length based on its cross-section;
3. The process that proposes the shortest step length is selected, and the particle is moved to its destination;
4. All processes along the step, such as ionization, are executed;
5. After the step, the post-step phase of the process that limited the step is executed. This phase involves updating dynamic properties and eventually producing any secondary particle;
6. If the kinetic energy of the particle reaches zero, all at-rest processes are executed or, if the particle is stable, its track is terminated. Otherwise, the process repeats with a new step, starting from stage 2.

This looped process allows for the simulation of particle transport and the execution of various processes along the particle's trajectory.

4.2.1 Electromagnetic processes in Geant4

When a particle undergoes interaction or decay in GEANT4, the software distinguishes between the physical process, which defines the initial and final state of the interaction, and the model implemented to simulate that process, which is responsible for controlling the production of secondary particles resulting from the interaction. GEANT4 provides a wide variety of physics models that can be selected: depending on the simulation and the precise physics phenomena that need to be simulated, users can choose the most appropriate models for their purpose.

In GEANT4 the implementation of these models often relies on pre-defined physics configurations, known as *physics lists*. Physics lists are collections of models, algorithms, and data libraries that govern particle interactions with matter. By selecting a specific physics list, users can determine the nature of physical phenomena that will be included in the simulation, including electromagnetic, hadronic, and optical interactions [89], [90]. Moreover, GEANT4 offers the flexibility to modify or integrate predefined physics lists with additional desired physical processes.

To include electromagnetic (EM) interactions in the simulation, GEANT4 offers various possible physics lists. One of the most used physics lists to model EM physics is the `G4EmStandardPhysics` library, which encompasses a wide range of electromagnetic phenomena (including electromagnetic scattering, ionization, bremsstrahlung, multiple scattering, and electron-positron pair production). `G4EmStandardPhysics` employs interaction models based on theoretical physics and experimental data, providing a generic and versatile approximation of electromagnetic processes. This physics list provides five distinct options for simulating electromagnetic processes, ranging from simpler and faster models (option 0 represented by the standard `G4EmStandardPhysics` physics list) to more accurate but computationally intensive ones (`G4EmStandardPhysics_option4`), allowing users to choose the level of precision required for their simulations. A common standard to simulate electromagnetic processes for high-energy physics (HEP) or nuclear physics applications is to adopt one physics list among the `G4EmStandardPhysics`, the `G4EmStandardPhysics_option1` and the `G4EmStandardPhysics_option2` [91]. `G4EmStandardPhysics_option3` and `G4EmStandardPhysics_option4` are more often chosen in simulations that require a high degree of precision, such as medical or space applications, since they generally demand extremely long computational times. However, for the specific system studied in this work, focusing on interactions between beta particles and photons with a semiconductor detector at low energy ranges (<6 MeV for electrons released in ^{111}Ag decay and <500 keV for γ produced in ^{111}Cd de-excitation), the selection of a physics list from the available options in the `G4EmStandardPhysics` library does not have a strong impact on the employed EM process models. As shown in Table 4.1 and 4.2, many of the models used by the possible options coincide within the energy range under investigation.

Physics List	**Rayleigh**	**Photoelectric**	**Compton**	**γ conversion**
Opt0	Livermore-Rayleigh 0-100 TeV [92]	Livermore-PhElectric 0-100 TeV [92]	KleinNishina 0-100 TeV [93]	BetheHeitler 0-80 GeV [94]
Opt1	none	Livermore-PhElectric 0-100 TeV	KleinNishina 0-100 TeV	BetheHeitler 0-80 GeV
Opt2	none	Livermore-PhElectric 0-100 TeV	KleinNishina 0-100 TeV	BetheHeitler 0-80 GeV
Opt2	none	Livermore-PhElectric 0-100 TeV	KleinNishina 0-100 TeV	BetheHeitler 0-80 GeV
Opt3	Livermore-Rayleigh 0-100 TeV	Livermore-PhElectric 0-100 TeV	KleinNishina 0-100 TeV	BetheHeitler 0-80 GeV
Opt4	Livermore-Rayleigh 0-100 TeV	Livermore-PhElectric 0-100 TeV	LowEP-ComptonModel 0-20 MeV [95]	Penelope-Conversion 0-20 MeV [96]

Table 4.1: Models used for γ processes for different GEANT4 EM physics constructors. From [97].

Physics List	**Coulomb scattering**	**Multiple scattering**	**Ionization**	**Bremsstrahlung**
Opt0	eCoulomb- Scattering 100 MeV-100 TeV [98]	UrbanMsc 0-100 MeV [99]	MollerBhabha 0-100 TeV [100]	eBremSB 0-1 GeV [101]
Opt1	eCoulomb- Scattering 100 MeV-100 TeV	UrbanMsc 0-100 MeV	MollerBhabha 0-100 TeV	eBremSB 0-1 GeV
Opt2	eCoulomb- Scattering 100 MeV-100 TeV	UrbanMsc 0-100 MeV	MollerBhabha 0-100 TeV	eBremSB 0-1 GeV
Opt3	none	UrbanMsc 0-100 MeV	MollerBhabha 0-100 TeV	eBremSB 0-1 GeV
Opt4	eCoulomb- Scattering 100 MeV-100 TeV	Goudsmit- Saunderson 0-100 MeV [102]	MollerBhabha 0-100 TeV	eBremSB 0-1 GeV

Table 4.2: Models used for electron processes for different GEANT4 EM physics constructors. From [97].

Additionally, it is possible to observe that the difference in terms of electron stopping power among the possible `G4EmStandardPhysics` options (and also other physics lists that can model EM interactions) is negligible, as depicted in Figure 4.3.

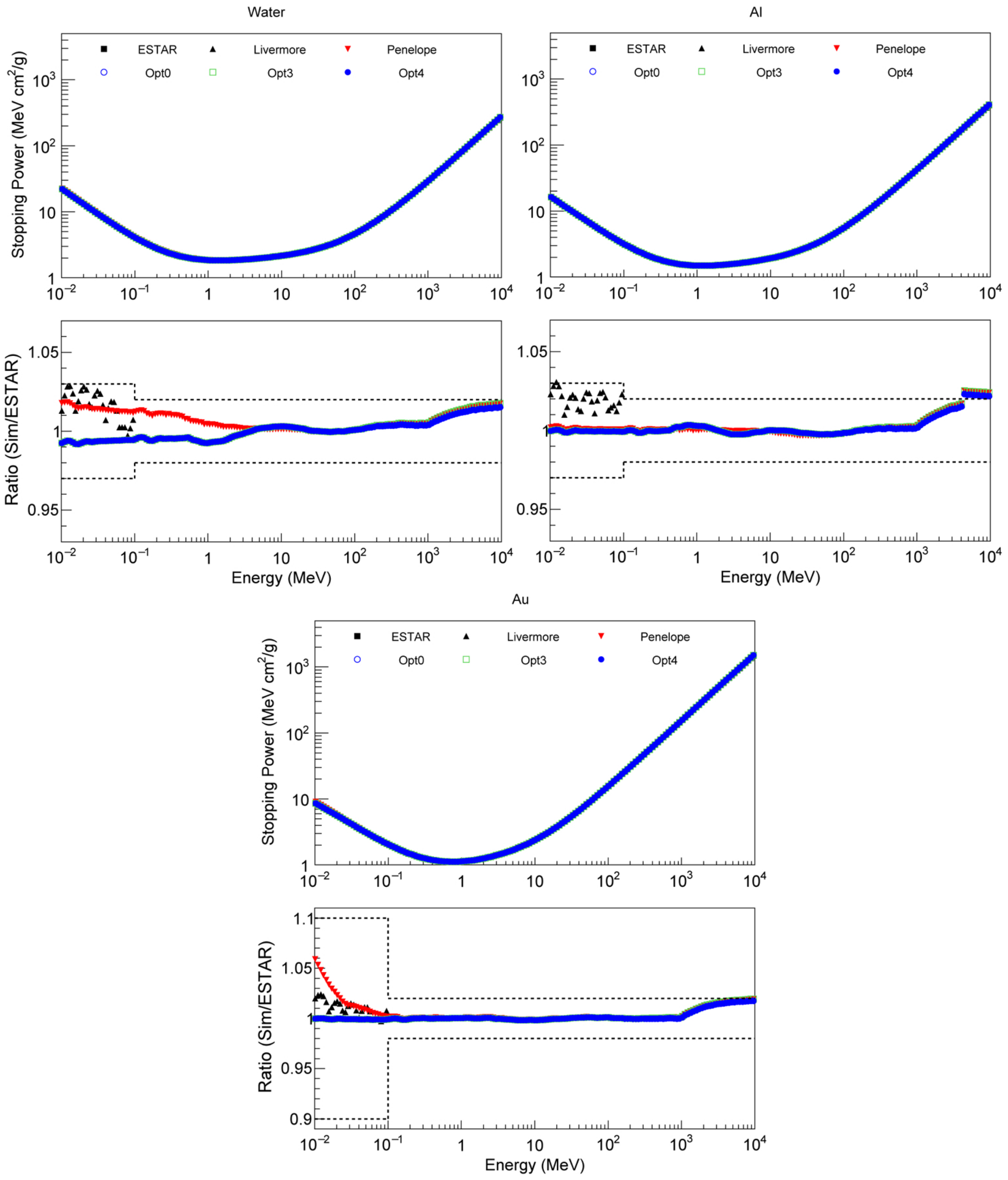

Figure 4.3: Electron electronic stopping power in three different materials (water, aluminum, and gold) calculated by means of different GEANT4 EM physics constructors, compared to the ESTAR reference data [30]. The lower plots show the ratio of the GEANT4 simulation results and ESTAR data (the dashed lines represent the uncertainty of the reference data). From [103].

From the previous information, it can be observed that options 0, 1, and 2 of the `G4EmStandardPhysics` library essentially employ the same models for electron and photon interactions. In the GEANT4 application developed in this study, it was thus chosen to select the standard `G4EmStandardPhysics` library to achieve a compromise between computational efficiency and accurate modeling of electromagnetic processes. This decision resulted in an elastic and relatively fast Monte Carlo simulation, while still ensuring a faithful representation of EM interactions.

4.2.2 Radioactive decay in Geant4

GEANT4 provides a dedicated physics list for implementing the decay of radioactive isotopes, both in-flight and at rest, through α, β^+ and β^- emissions, and electron capture. The simulation of radioactive decay is primarily handled by the `G4RadioactiveDecay` class, along with other associated classes, which sample secondary particles on a per-decay basis. The adopted simulation model relies on data obtained from the Evaluated Nuclear Structure Data File (ENSDF) [104]. This data source provides essential information such as nuclear half-lives, nuclear level structure for the parent or daughter nuclide, decay branching ratios, and the energy associated with the decay process. De-excitation emissions, including γ-rays and conversion electrons, as well as fluorescence emissions resulting from electron-capture and beta decays, are handled by specific classes (`G4PhotonEvaporation` and `G4AtomicDeexcitation`, respectively) [105], [106].

In the context of the studied application, it is worth briefly presenting the implementation of beta decay in GEANT4. Beta decay is a three-body process, which results in the emission of a beta particle, an anti-neutrino or neutrino, and a recoil nucleus of either $Z+1$ or $Z-1$. The electron or positron features a continuous emission spectrum. The energy spectrum of the released electron or positron is accurately described by [106]:

$$\frac{\mathrm{d}^2 n}{\mathrm{d}p\mathrm{d}E} = (E_0 - E)^2 pEF(Z,E)S(Z,E,E_0),$$

where E and p are the total energy and total momentum of the beta particle, E_0 is the end-point energy of the β-emission, $S(Z,E,E_0)$ is a shape factor, and $F(Z,E)$ is the Fermi function, a parameter which incorporates corrections for the Coulomb interaction between the charged nucleus and the beta particle.

`G4RadioactiveDecayPhysics` exploits the most performant approximation of the Fermi function, which is described by [107], [108]:

$$F(Z,E) = \left(A + \frac{B}{E-1}\right)^{1/2},$$

where Z is the β-emitter atomic number, while A and B are two empirical parameters derived from an experimental dataset [109]. The two parameters can be calculated as [107], [108]:

$$A = \begin{cases} 1 + 0.405\exp(0.073Z) & \text{for } Z \leqslant 16 \\ 0.073Z + 0.94 & \text{for } Z > 16 \end{cases}$$

$$B = aZ\exp(bZ),$$

with

$$a = \begin{cases} 0.006 & \text{for } Z \leqslant 56 \\ 0.001 & \text{for } Z > 56 \end{cases}$$

$$b = \begin{cases} 0.077 & \text{for } Z \leqslant 56 \\ 0.101 & \text{for } Z > 56. \end{cases}$$

It can be proven that this Fermi function approximation yields results within a 1% margin of error when compared to the tabulated experimental values [108].

If a specific set of parameters is computed for the first time, an energy distribution is calculated and used to determine the energy of the particles emitted. Subsequent occurrences of the same parameter set will directly draw particle energies from this distribution, reducing processing time.

4.3 Geant4 application: simulated geometry

The development of the Geant4 simulation required accurate modeling of the geometry of all the components of the investigated setup. The system under analysis is composed of two main elements: the beta detector being studied and the biological radiation source, consisting of two possible types of cell cultures for the ISOLPHARM radiopharmaceutical prototype testing. The geometry developed for the radiation detector is described in Section 4.3.1, while the geometry for the radiation source is presented in Section 4.3.2.

To validate the designed Geant4 detector model, preliminary measurements were conducted using the ALPIDE chip along with collimated laboratory sources. These tests aimed to ensure that the developed detector model's response aligned with the actual detector's behavior. In addition to modeling the in-vitro system for future experiments, a Geant4 simulation was created to replicate the geometry of the experimental setup used for these measurements. This model will be described in detail in the next Section 4.4.2.

4.3.1 Detector geometry

The ISOLPHARM beta detector currently under construction will consist of 4 or potentially 8 ALPIDE MAPS chips arranged in a flat geometry. To precisely replicate the behavior of this instrument within the Geant4 framework, a comprehensive model of the detector's structure was designed. The Geant4 geometry was modeled starting from the implementation of an individual ALPIDE chip. The focus then shifted to the assembly of multiple ALPIDE detectors to create the complete device geometry.

The first step in the realization of the detector structure was the creation of the ALPIDE chip. As explained in detail in Section 3.1.2, ALPIDE consists of numerous single pixels organized in a 1024 × 512 matrix. In order to represent the segmented structure of the detector in Geant4, a modular approach was adopted. A single pixel was modeled and it was replicated (utilizing the `G4PVReplica` class) along the columns, with 512 replicated modules per column. In turn, each column was replicated for 1024 rows to obtain the final geometry. Figure 4.4 schematizes this process.

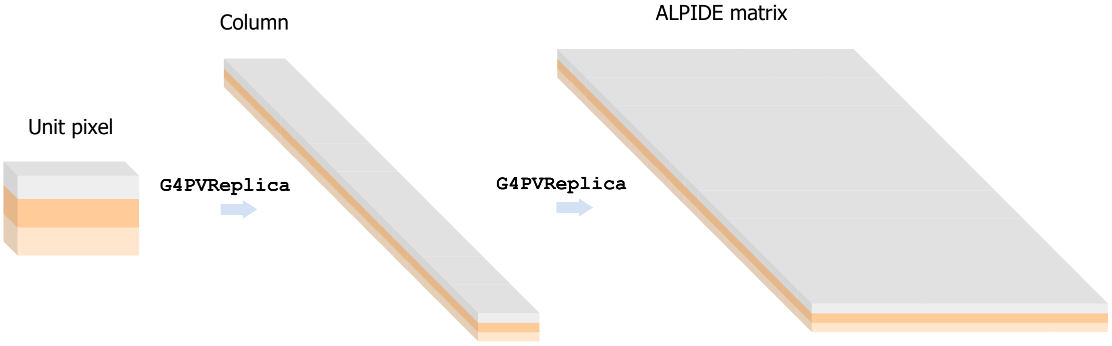

Figure 4.4: Geant4 simulation approach for constructing an ALPIDE chip using `G4PVReplica` class.

The unit ALPIDE pixel was modeled according to a multi-layer structure that reflects the composition of the ALPIDE chip itself. As depicted in Figure 4.5, the geometry of each 28 μ × 28 μ pixel can be divided into three main components:

- The bottom region represents the non-sensitive **substrate** of the MAPS detector, depicted as a

14 μm thick silicon layer;

- the intermediate volume reproduces the silicon **epitaxial layer**, which serves as the sensitive part of the ALPIDE chip. Interactions of incoming radiation with this layer create electron-hole pairs that are collected to determine the hit pixel. The epitaxial region has a total thickness of 25 μm;
- the upper layer models the built-in **electronics** embedded in the MAPS chip for signal collection and manipulation. This region is represented by an 11 μm thick SiO_2 volume.

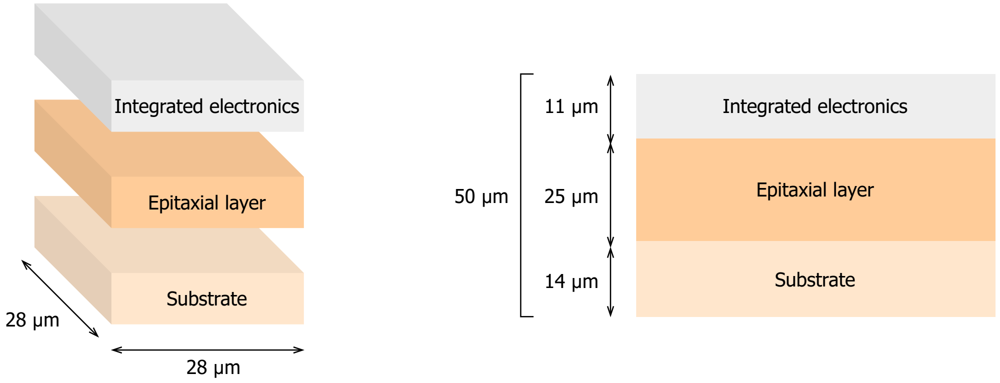

Figure 4.5: Geant4 simulation structure of a unit ALPIDE pixel. The diagram illustrates the three layers that compose the pixel.

Inside the pixel, only the epitaxial layer represents the sensitive volume. In Geant4, the `SetSensitiveDetector`() method is used to assign sensitivity to specific volumes within the modeled geometry. In the developed application, the sensitive region of each pixel was defined by setting the epitaxial layer as the "sensitive detector" using `SetSensitiveDetector`(). This guarantees that only particles interacting with this layer are considered to produce a hit in the simulation. By designating the epitaxial layer as the sensitive part, Geant4 focuses its tracking and analysis efforts on interactions that occur within this layer.

In the final design of the geometry replicating the experimental system to be used in in-vitro experiments, the source will be positioned above the surface of the detector that incorporates electronics for initial signal processing. As a consequence, the ionizing radiation traverses the built-in electronics before interacting with the sensitive volume. This choice is made in line with the common approach employed in the use of the MAPS ALPIDE. It can be observed that the layer integrating the electronics is thinner than the substrate. Furthermore, the built-in electronics are specifically designed to withstand high levels of radiation hardness, ensuring proper functionality even when subjected to radiation exposure.

A single ALPIDE chip is obtained by replicating the pixel object as previously explained. The resulting structure consists of a 1024 × 512 matrix that represents the whole MAPS detector.

To construct the complete beta detector, multiple instances of these modeled ALPIDE were positioned in planar geometry. Since two possible arrangements were considered for the final detector geometry, both dispositions were reproduced in the Geant4 simulation.

In the first configuration, the ALPIDE chips are arranged in a 2 × 2 grid, with the external circuitry positioned outward. As illustrated in Figure 3.3(b), each ALPIDE detector has an additional non-sensitive area (1.2×30 mm^2) that contains the necessary electronics for signal readout and other functionalities, and it is situated on one of its long sides. To eliminate this dead volume from the sensitive region, the long sides are oriented outward. This arrangement optimizes space usage while maintaining a compact size. Figure 4.6 shows the implemented geometry for the 2 × 2 configuration.

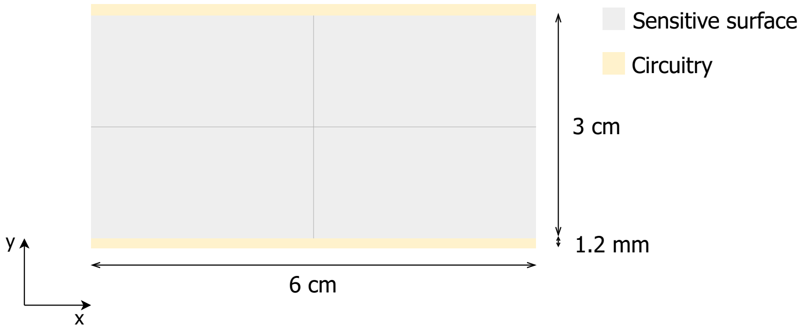

Figure 4.6: Geometry of the 2 × 2 configuration for the beta detector.

The second design features a 4 × 2 arrangement, where the chips are positioned in two rows facing each other along their long sides (as shown in Figure 4.7). This design choice enables the removal of electronics from the central region of the detector, resulting in a larger overall size of the sensitive surface. By minimizing the presence of dead space in the central measurement area, this configuration provides the opportunity to utilize a more extensive detector area, with one dimension significantly larger than the other. A larger sensitive region can accommodate a larger radiation source, especially in the case of hydrogel-based cell cultures where there are no limitations imposed by culture dishes' dimensions. This expanded area could allow for the inclusion of more cells and different types of cell lines in a single acquisition.

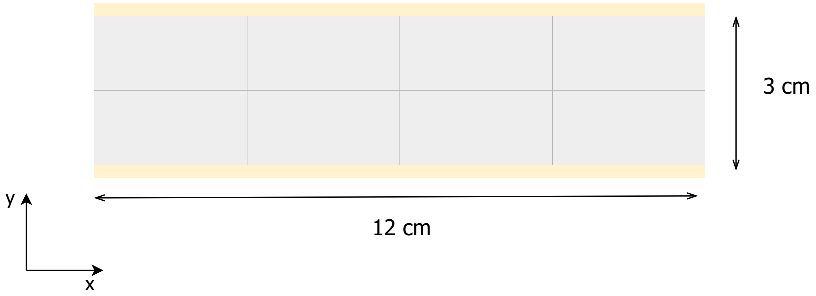

Figure 4.7: Geometry of the 4 × 2 configuration for the beta detector.

It is worth noting that additional arrangements that utilize a 4 × 2 geometry can be considered. These alternative 4 × 2 configurations, where the chips in each row face each other along their short sides, would introduce dead zones within the sensitive region. The dead zones can vary from a minimum of 2 (if centrally located with respect to the detector's surface and with double the thickness of the peripheral circuitry) to a maximum of 4 (if positioned less centrally but distributed across multiple locations). Figure 4.8 provides a comparison of these two potential dead layer arrangements. Throughout the discussion regarding the final implementation, all possible options for the 4 × 2 configuration were considered. The ultimate choice favored the design that maximized the detector's sensitive area, avoiding the presence of dead spaces within the acquisition area. Specifically, the preference was given to the first described 4 × 2 configuration, as it also enables harnessing the potential of asymmetric three-dimensional cultures. Exploiting hydrogel-based cultures with a geometry specifically designed for the set purpose, it becomes possible to utilize surfaces with vastly different dimensions from each other.

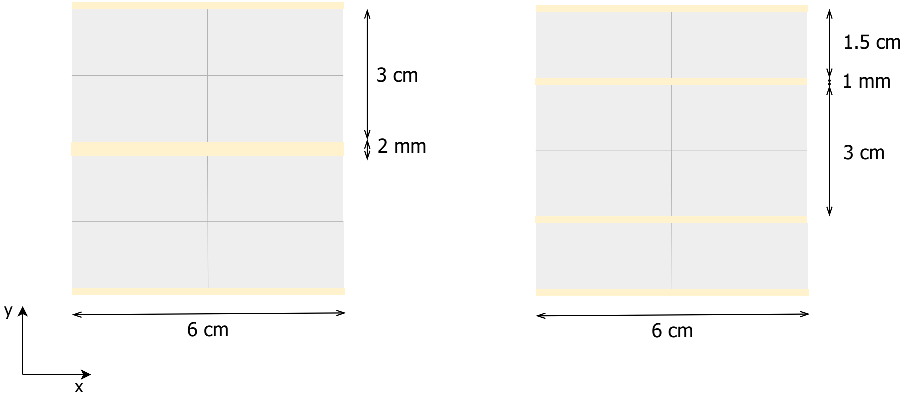

Figure 4.8: Comparison of dead layer arrangements in the alternative 4 × 2 configuration of the beta detector.

Both implemented detector geometries in Geant4 were incorporated into a Printed Circuit Board (PCB). The PCB is made of FR4 material, which is a widely used substrate material in the electronics industry to produce PCBs. FR4 is a type of fiberglass-reinforced epoxy laminate that provides good electrical insulation properties, mechanical strength, and heat resistance. The PCB volume in Geant4 was modeled to fully enclose the detector, ensuring that only one of its surfaces is exposed. In this case, it is the surface where the integrated electronics of the MAPS detector are located.
Figure 4.9 showcases the geometry of the complete beta detector object (in the 2 × 2 configuration) as developed in Geant4. The visualization is achieved through the Geant4 graphical user interface (GUI) and depicts both the detector on its own and its inclusion within the printed circuit board in the simulation.

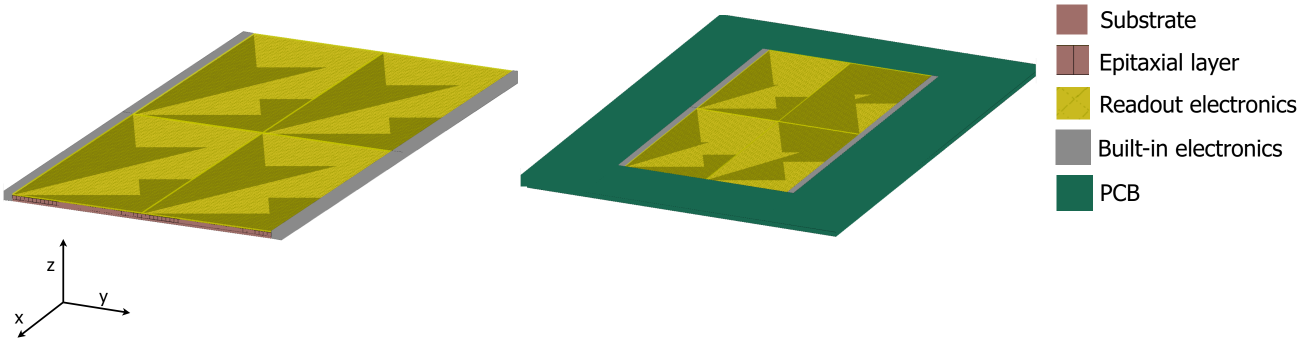

Figure 4.9: Geant4 modeling of the beta detector under investigation in its 2 × 2 configuration, with and without the printed circuit board.

4.3.2 Radiation source geometry

In the coming years, the beta detector under analysis will be used for in-vitro experiments aimed at evaluating the internalization of the prototype ^{111}Ag-based radiopharmaceutical. The ISOLPHARM collaboration is currently exploring two different types of cell cultures to employ in these experiments: a traditional two-dimensional culture and a three-dimensional hydrogel-based culture. Both cell culture types were modeled in the Geant4 simulation. Each of them represents a specific scenario to test the detector's performance and assess its potential in future in-vitro tests.
For the type of application being studied, the cells are modeled with a simplified approach as aqueous

spheres with a radius of 10 μm. The precise cellular radius may vary depending on the specific cell line chosen, but an average cell size of 20 μm was considered [110]. In the context of ionizing radiation interactions, water is commonly considered a suitable material for simulating the cellular composition due to its similar properties and response to radiation [111]. To simulate the deposition of the radiopharmaceutical within the cellular volume, the decay of ^{111}Ag was modeled exclusively within that spherical volume, with a random point inside the volume selected as the decay site.

The traditional two-dimensional cell culture was modeled by incorporating a petri dish, a common laboratory tool used for culturing cells. A petri dish is a lidded cylindrical container that provides a controlled environment for cell growth. In this scenario, petri dishes with the thinnest possible bottoms were considered to minimize the distance between the source and the detector, while simultaneously reducing the attenuation of electrons generated during the decay of ^{111}Ag. This choice was made to improve the accuracy of determining the emission position by the beta detector. By reducing the thickness of the petri dish, the emitted electrons have a higher probability of reaching the detector without significant scattering. This allows for a more precise localization of the decay event. Commercially available petri dishes with bottoms made of mylar or similar materials offer thicknesses around 25 μm, which are suitable for this purpose [112]. The simulation included a cylindrical petri dish with polystyrene walls and a thin mylar bottom. The petri dish had an external diameter of 35 mm, an internal diameter of 32 mm, and a height of 1 cm.

To simulate the cell culture within the petri dish, the cells are dispersed in an appropriate aqueous medium. For the purpose of the analysis, the medium is modeled as a water volume inside the petri dish, with a layer of cells dispersed within it. The cells are randomly distributed within the medium, ensuring that each cell is placed at a random position that is sufficiently distant from other cells and the walls of the petri dish to avoid overlapping. This random placement of cells aims to mimic the natural distribution of cells within a culture and avoids any biased or ordered arrangement that could affect the simulation results.

Figure 4.10 illustrates the geometry of the two-dimensional cell culture system as developed in Geant4.

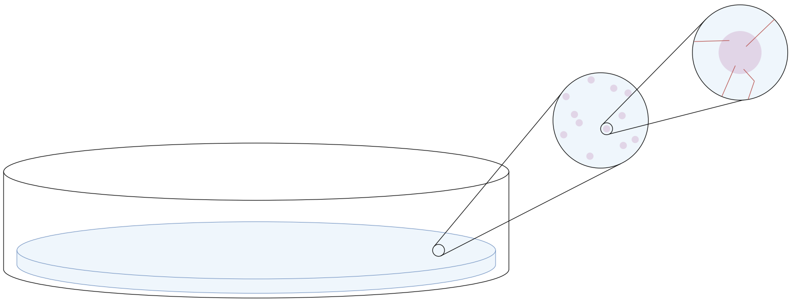

Figure 4.10: Geant4 modeling of two-dimensional cell culture system with a zoomed-in view of a single cell.

The three-dimensional hydrogel-based culture was included in the Geant4 simulation modeling a hydrogel matrix. Hydrogels are three-dimensional networks of crosslinked hydrophilic polymer chains that have the ability to absorb and retain significant amounts of water while maintaining their structural integrity [113], [114]. The production of hydrogel-based cell cultures for the future experiments of the ISOLPHARM project is in collaboration with the BIOtech (Center for Biomedical Technologies) research center of the University of Trento [3]. The material used by BIOtech for culture production is composed of a mixture of water (95%) and GelMa (Gelatin Methacryloyl, 5%), a type of hydrogel derived from gelatin, which is modified through the addition of methacrylic anhydride ($\approx$ 30%). GelMa exhibits properties such as biocompatibility, biodegradability, and tunable mechanical properties, making it suitable for various biomedical applications [115]. In particular, this type of cell culture system offers great flexibility in shaping the volume for the desired application. For the current study, the goal was to minimize the thickness of the culture to reduce the distance between the surface of the detector and the cell culture. Collaborating with the BIOtech, it was determined that the minimum achievable thickness for a semi-solid three-dimensional structure was 500 μm. Therefore, in all the evaluated applications, the hydrogel volumes were created with this thickness.

In the developed GEANT4 application, the 3D cell culture was incorporated by utilizing volumes of hydrogel in which cells, modeled as described earlier for two-dimensional cultures, were randomly dispersed. Figure 4.11 depicts the geometry implemented in GEANT4 to model these cultures.

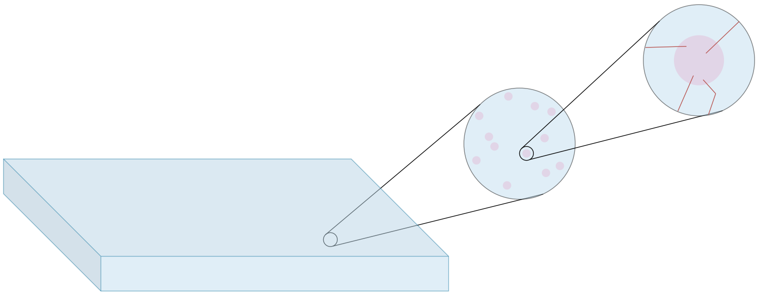

Figure 4.11: GEANT4 modeling of three-dimensional cell culture system with a zoomed-in view of a single cell.

4.4 Geant4 application: testing and validation of the developed simulation

The aim of the developed modeling is to conduct Monte Carlo simulations in GEANT4 to understand the features and potential of the setup that will be used in the future in-vitro testing of the ISOLPHARM drug prototype. To achieve reliable results, the developed GEANT4 model seeks to closely replicate the scenario that will be encountered. It is thus of interest to assess the simulation's ability to predict results attainable in a realistic scenario utilizing the ALPIDE detector.

Currently, the University of Padova has access to several ALPIDE chips, which have enabled preliminary experimental tests. By utilizing individual chips within acquisitions with known external sources, it becomes possible to investigate whether the characterization of the ALPIDE detector in GEANT4 yields results consistent with those obtained experimentally.

On the other hand, the possibility of working with cell cultures to test their reproduction in GEANT4 is still premature within the ADMIRAL context [5]. For this reason, in the past months, it was not possible to work with biological sources. The decision was made to select laboratory sources that could provide valuable data for future applications. Unfortunately, a source of ^{111}Ag was not available during this very preliminary experimental phase. As explained in Section 1.3, until the SPES facility becomes operational, the production of ^{111}Ag must rely on conventional methods, which require longer times and higher costs. At the moment, the ISOLPHARM project relies on the reactor within the Laboratorio Energia Nucleare Applicata (LENA [116], shown in Figure 4.12) to obtain the necessary quantities of the silver radioisotope through the irradiation of natural or enriched palladium [21]. This approach does not provide large quantities of the radioactive nuclide, directing what is obtained to the experimental phases that require it most. Nevertheless, the use of laboratory sources has allowed the attainment of results relevant to the purpose of these preliminary tests: to handle and operate the ALPIDE detector for the first time and to put the developed simulation to the test.

The experimental setup used to obtain the necessary measurements is described in Section 4.4.1, while the simulation developed to replicate this setup is presented in Section 4.4.2. The final analysis is discussed in Section 4.4.3.

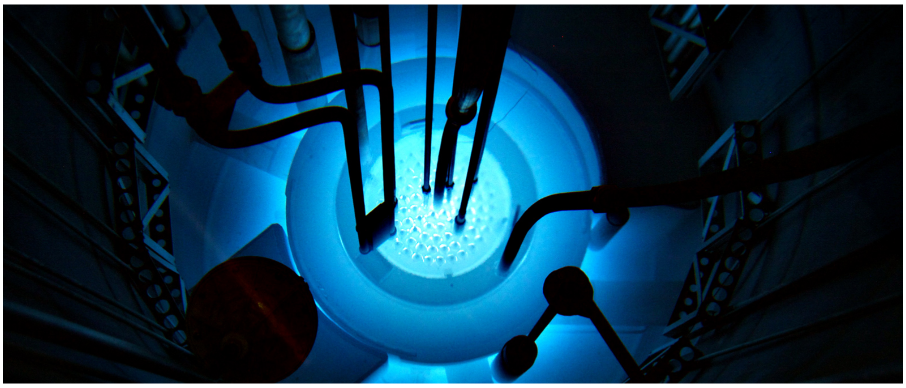

Figure 4.12: Cherenkov light produced within the reactor located at LENA. From [116].

4.4.1 Experimental setup

The experimental setup comprises two main components: the available ALPIDE chip and two laboratory radioactive sources.

The MAPS ALPIDE chip had been previously encapsulated within a printed circuit board to create an integrated system that could be easily managed. This assembly was seamlessly interfaced with a Field-Programmable Gate Array (FPGA) board, on which a custom-built firmware was installed to facilitate the operation of the detector. The resulting system, consisting of the detector and FPGA, is depicted in Figure 4.15(a).

The utilized firmware was designed by the ISOLPHARM research group at the University of Padova and enabled the activation and configuration of the ALPIDE chip, as well as initiating and managing data acquisition. Despite being preliminary at this stage, the available firmware supported the essential functions required for the initial operation of the detector. In particular, the firmware allowed adjustment of the trigger necessary for ALPIDE's operation. Although the event rate of the laboratory sources did not necessitate triggering, the dead times were adapted to prevent memory saturation and ensure proper data transmission. The data were channeled to a host computer through a local area network, facilitating their retrieval in a digitized form, ready for subsequent analyses.

The laboratory sources used are two, both produced by Spectrum Techniques [117].

The first one considered is a $\beta-$ source of ^{90}Sr. ^{90}Sr decays $\beta-$ in 100% of cases into ^{90}Y (in its ground state), with half-life of $T_{1/2}^{^{90}\text{Sr}} = 28.91(3)$ years. The electron emitted in the decay of the strontium isotope has an average energy of 195.7(5) keV and an end-point energy of 545.9(14) keV [24]. The daughter isotope ^{90}Y is unstable, decaying $\beta-$ to ^{90}Zr (99% of the time, in its ground state) with a mean lifetime of $T_{1/2}^{^{90}\text{Y}} = 64.05(5)$ hours. The energy spectrum associated with the beta particle released in the decay of the yttrium nuclide has an end-point energy of 2278.5(16) keV, while the average energy is 932.4(7) keV [24]. For simplicity, the information associated with the two isotopes involved in the decay of this source is summarized in Table 4.3, and a comparison between the two energy spectra is presented in Figure 4.13(a) and 4.13(b).

Transition	$\boldsymbol{T_{1/2}}$	$\boldsymbol{< E_{e-} >}$	$\boldsymbol{E_{e-}^{\text{end-point}}}$
$^{90}\text{Sr} \xrightarrow{\beta-} {}^{90}\text{Y}$	28.91(3) y	195.7(5) keV	545.9(14) keV
$^{90}\text{Y} \xrightarrow{\beta-} {}^{90}\text{Zr}$	64.05(5) h	932.4(7) keV	2278.5(16) keV

Table 4.3: Information about the decay of ^{90}Sr (parent nuclide) and ^{90}Y (daughter nuclide). Data from [24].

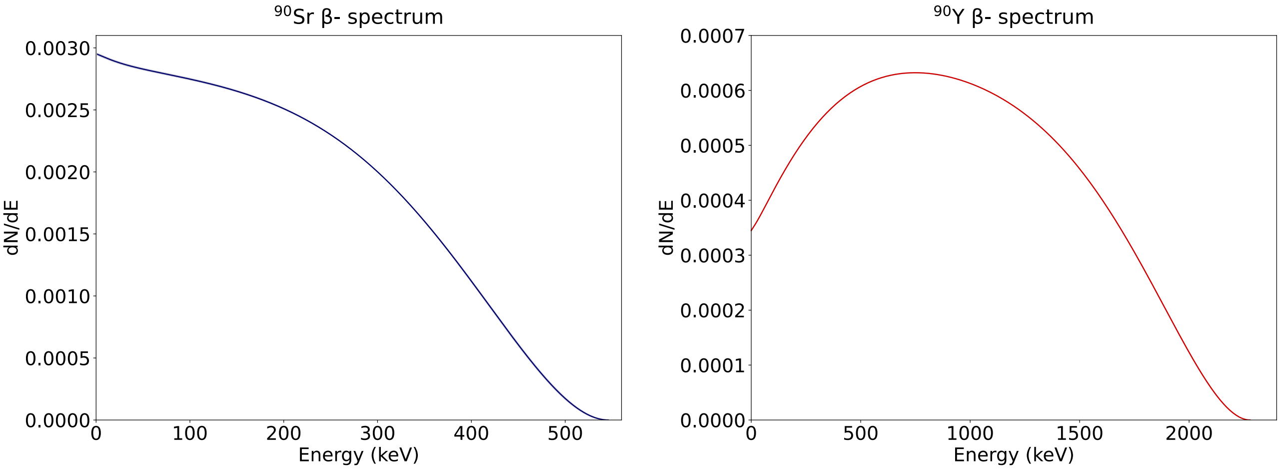

(a) (b)

Figure 4.13: Energy spectrum of the $\beta-$ particles emitted in the decay of (a) ^{90}Sr and (b) ^{90}Y. Data from [24].

The ^{90}Sr isotope was chosen because it allows the study of a γ-free β-emitter to test the detector's response to the beta radiation. The electrons produced in the decay of ^{90}Y generate a total spectrum that is more energetic for a ^{90}Sr source compared to ^{111}Ag. An initial test of the ALPIDE chip with a strontium source allows verification of whether and how the beta radiation produced is detected by the device, providing initial insight into the detector's ability to interact with energetic electrons.

The second chosen source is ^{137}Cs. ^{137}Cs is also a $\beta-$ source that decays to ^{137}Ba with half-life of 30.08(9) years. In 94.6% of cases, this decay leads to an excited metastable state of barium (^{137m}Ba) which de-excites to the ground state with a half-life of 156 s through the emission of a 661.6 keV γ-ray. This decay is characterized by an energy spectrum with an end-point energy of 513.97(17) keV and a mean energy of 174.32(6) keV. The remaining 5.4% of cases directly lead to the ground state of the barium isotope (the β-emission has an end-point energy of 1175.63(17) keV and a mean energy of 416.26(8) keV). The energy spectra associated with the decay of ^{137}Cs are shown in Figure 4.14.

The de-excitation emission from the metastable state of ^{137}Ba dominates the energy spectrum of a ^{137}Cs source. Despite the emitted γ-rays being monoenergetic, these photons tend to deposit only part of their total energy in the detector through a Compton scattering interaction, creating a characteristic continuous spectrum in the energy region corresponding to the beta emission of ^{137}Cs.

At times, ^{137m}Ba tends to lose energy through internal conversion as well, transferring the excess energy to an electron of the innermost atomic shells which is released from its atomic binding. The resulting hole in the atomic shell is then filled by electrons from higher shells, leading to the emission of characteristic X-radiation of barium (particularly the K_α line at 32.19 keV).

All the information related to the described decays is summarized in Table 4.4.

Transition	$T_{1/2}$	**Final state**	$< E_{e-} >$	$E_{e-}^{\text{end-point}}$
$^{137}\text{Cs} \xrightarrow{\beta-} {}^{137}\text{Ba}$	30.08(9) years	^{137}Ba (0 keV)	416.26(8) keV	1175.63(17) keV
		^{137m}Ba (661.6 keV)	174.32(6) keV	513.97(17) keV
Transition	τ	**Final state**	E_γ	
$^{137m}\text{Ba} \xrightarrow{\gamma} {}^{137}\text{Ba}$	156 s	^{137}Ba (0 keV)	661.6 keV	

Table 4.4: Information about the decay of ^{137}Cs (parent nuclide) and ^{137m}Ba (daughter nuclide). Data from [24].

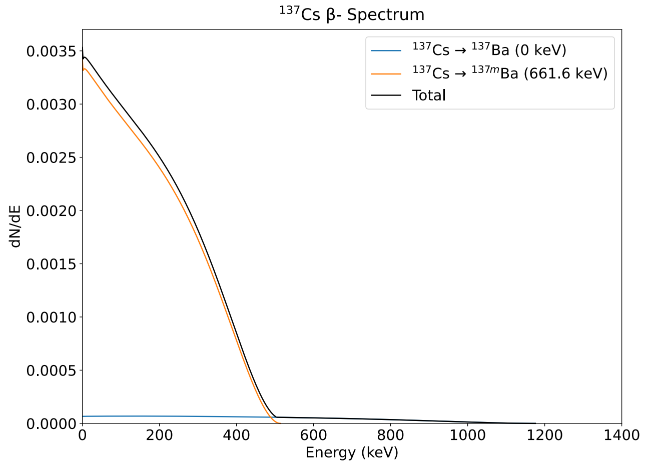

Figure 4.14: Energy spectrum of the $\beta-$ particles emitted in the decay of ^{137}Cs. Data from [24].

In the case of ^{137}Cs, most electrons produced and detectable by the ALPIDE detector are accompanied by a γ-emission. Consequently, the acquired images will exhibit a significant component associated with photons interacting with the device. The purpose of utilizing this source is to verify whether the ALPIDE detector modeled in GEANT4 can accurately describe photon interactions.

To facilitate the used sources and collimate the emitted beta radiation as much as possible, a small aluminum support was employed. The support's geometry was designed to integrate seamlessly with the setup. The support consists of a 2 mm thick aluminum bar held in place by 4 screws that attach to an external box enclosing the setup. The plate is drilled with a hole of diameter 1.5 mm to create a collimated beam with known geometry. The plate is placed at a distance of 2 mm from the device, ensuring that the exposed micro-bondings connecting the ALPIDE to the PCB are not damaged. The thickness of the collimator material is insufficient to completely shield the electrons released in the decay of the sources. Nonetheless, it enables a cost-effective creation of the necessary support.

In conclusion, the employed experimental setup consists of the operational ALPIDE detector connected to an FPGA that enables the execution of an acquisition firmware, along with two laboratory sources (^{90}Sr and ^{137}Cs). These sources are positioned at a fixed distance from the detector using a support designed for the system. Once the setup is ready, it is covered with a black sheet designed to absorb ambient photons, aiming to minimize background sources as much as possible. Figure 4.15(b) depicts the utilized setup.

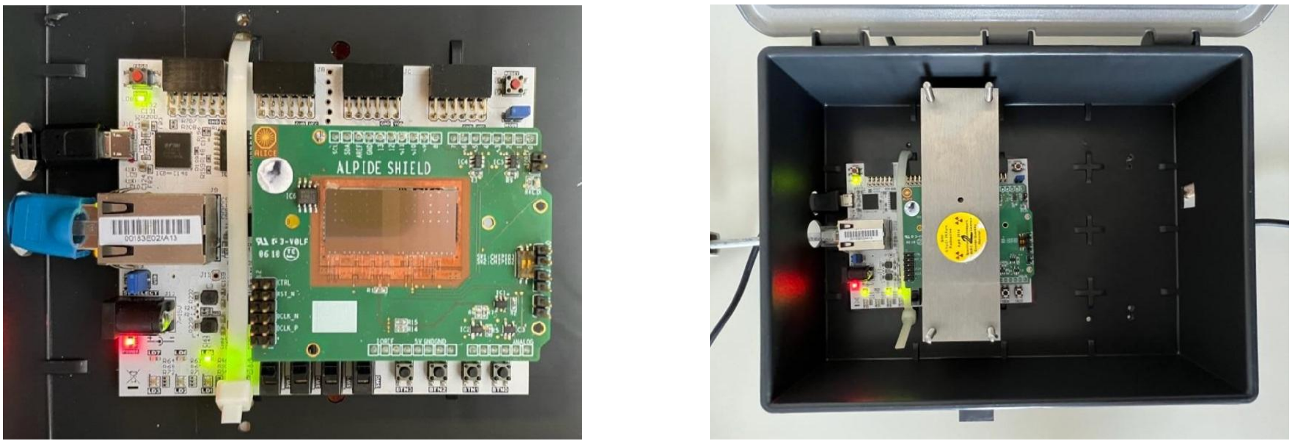

(a) (b)

Figure 4.15: Experimental setup employed in the initial tests involving ALPIDE. The detector is operated with an FPGA to implement an acquisition firmware (a). The radioactive sources are positioned using custom-designed support (b).

4.4.2 Experimental setup modeling

The initial stage in analyzing the images obtained during data acquisition involved the development of a comprehensive modeling of the setup used, encompassing both the sources' geometry and their positioning. The two sources were simulated based on the information provided by the manufacturer (Spectrum Techniques [117]).

The ^{90}Sr source is a laminate disk source with aluminized mylar windows: it consists of a thin cylinder of radioactive material with a diameter of 6.25 mm encapsulated within a disk made of high-strength laminate material, and one of its sides is covered with a thin layer (0.127 mm) of aluminized mylar (80 μg/cm^2). This type of source is designed for situations where a low degree of attenuation is required for emitted particles. In the case of β sources, this helps ensure that electrons do not interact frequently with the protective material before reaching the detector.

In Geant4, this geometry was modeled by considering two cylindrical volumes, one containing the other. The innermost volume simulates the ^{90}Sr deposit, while the outer volume is made of laminated plastic material (PET). On one of the two surfaces, a layer of aluminized mylar adapted to the source's dimensions was introduced.

The ^{137}Cs source is a classic laminate disk source. Designed as a γ source, the cesium deposited in the source is encapsulated in high-strength laminate material that enhances attenuation effects. In this case, the supplier does not provide precise information about the size of the radioactive deposit volume, but only about the protective capsule.

In Geant4, the ^{137}Cs source is constructed similarly to the strontium source, with some modifications. In this case, the radioactive material is placed inside a PET cylinder that simulates the protective coating. Cesium is distributed within a volume with a height equal to half the total thickness of the protective layer and a diameter of 6.25 mm, similar to the case of ^{90}Sr. Since specific measurements were not provided and the source could not be handled, these measurements were assumed as reasonable hypotheses.

A schematic representation of the modeling implemented for the two sources is presented in Figure 4.16.

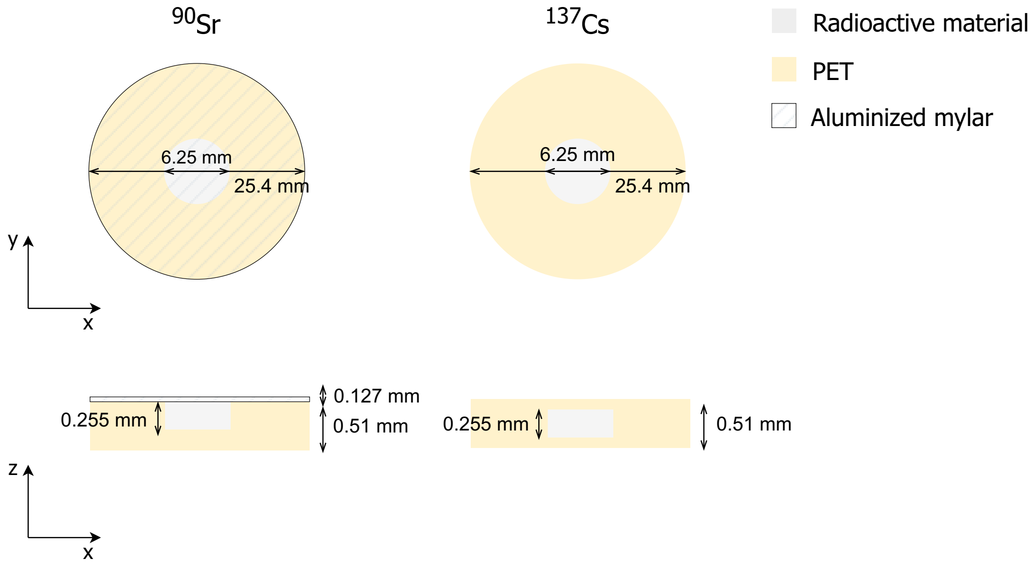

Figure 4.16: Schematic representation of the modeling of the radioactive sources (^{90}Sr and ^{137}Cs) used during the experimental activity.

In the experimental setup, the used source is placed on a specifically perforated support to reduce attenuation in a region with a known cross section. The collimator is represented in Geant4 as an aluminum plate, and its dimensions have been accurately replicated. To model not only the presence of the support but also the positioning of the hole and its placement relative to the surface of the detector, all necessary dimensions were measured before introducing the source. The gathered information was incorporated into the support's modeling and is illustrated in Figure 4.17, which presents a schematic diagram of the geometry model considered to replicate the setup.

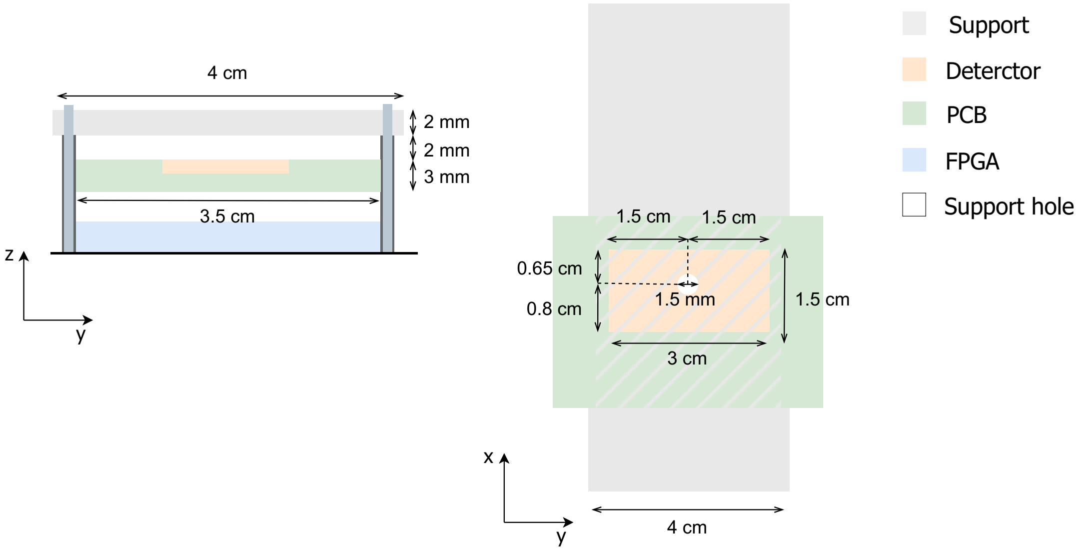

Figure 4.17: Schematic representation of the used setup (cross-sectional and orthogonal view). The illustration shows the relevant distances for simulation purposes.

To simulate the setup under examination, a single ALPIDE chip was incorporated within the developed Geant4 application. The detector has been modeled as described in Section 4.3.1 and is placed inside a PCB. In the simulation, the volumes of the FPGA and the outer box have been omitted: given their sufficient distance, particles interacting with these volumes should not interfere with the ongoing measurements.

4.4.3 Data analysis and simulation testing

The output of the ALPIDE detector provides information about the positions of the recorded hits during the acquisition. As it consists of a tracking detector, the chip is not designed to extract energy information and consequently only provides the coordinates of the observed hits. The programmed firmware rearranges this information in terms of pixel hit coordinates: when the trigger is active, a pair (x, y) is saved for each detected hit, where $x \in [0, 1023]$ represents the pixel ID along the longer axis of the detector, and $y \in [0, 511]$ along the shorter axis.

From all the collected hits, it was possible to reconstruct a final image as a two-dimensional histogram summing all the individual short acquisitions that were carried out. During the experimental activity, it was observed that the local network was relatively unstable, preventing too prolonged acquisitions. Therefore, the approach was to divide the image production into several short measurements, which were then combined into a single image.

The images were obtained for both the ^{90}Sr and ^{137}Cs sources. For each of these cases, a specific analysis was conducted to study the obtained outcome and compare it with the predictions from Geant4 simulations.

The first case under examination involves measurements with the strontium beta source. As previously mentioned, ^{90}Sr is of interest because it is a beta source (with almost negligible γ production probability) with relatively high energy electrons. The raw image obtained when the source is positioned 2 mm from the detector is shown in Figure 4.18. In this image, the counts obtained are normalized, ensuring that the most populous bins have a unit frequency, and all other bins are filled proportionally, resulting in counts always within the range [0, 1]. This choice enables the visualization of an image while capturing the trend beyond the specific number of total hits recorded, and it is adopted for all subsequent plots.

The image allows not only the visual identification of the area where the electron beam interacts with the chip but also the investigation of the corresponding distribution, determining its center and width. To meticulously study the obtained image, the projections along the two axes, x and y, were analyzed. The profile of the image along one axis is computed by selecting a range along that direction and projecting the 2D histogram along the other axis. For each of the projections, it was decided not to consider a single position along the projection axis but to integrate along a narrow range to increase the counts considered. The performed operation is visually summarized in Figure 4.18, which also displays the profiles inferred using this approach.

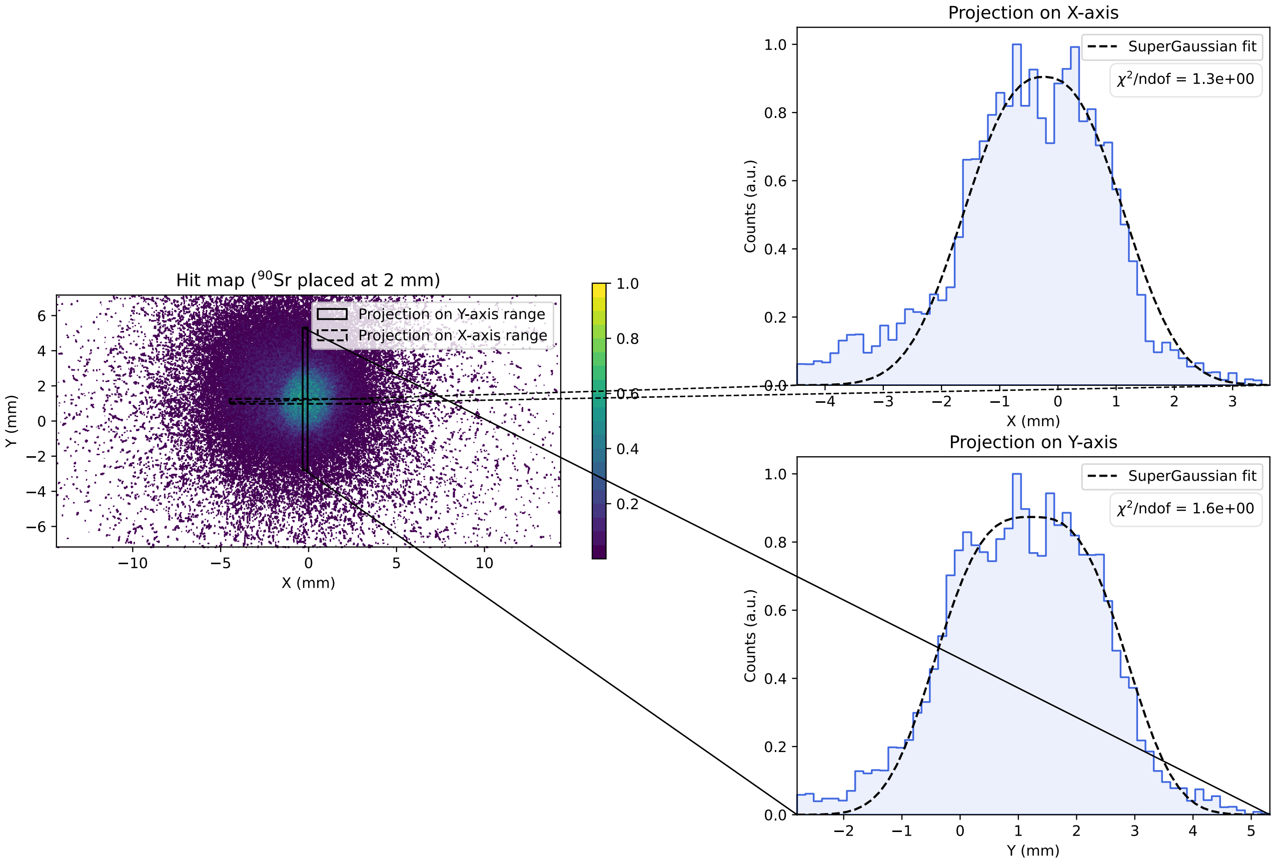

Figure 4.18: Profiles (and projection ranges) of the 2D image obtained using a ^{90}Sr source during the ALPIDE detector tests. The source is positioned 2 mm away from the detector surface. The two profiles are fitted using a super-Gaussian distribution (generalized Gaussian function).

The figure allows for some considerations. The image displays a high-count region, with the highest counts corresponding to the cross-section of the electron beam collimated onto the detector surface. However, in the surrounding area, there is a low-count region produced by scattering effects of the emitted particles with the materials present between the emission point and the detector, particularly the support itself. Due to the thinness of the collimator, it was expected that it would not entirely prevent beta particles from reaching the detector. It is interesting, though, to observe that in areas covered by the supporting plate, the count rate is significantly lower, allowing for a possible post-processing procedure to eliminate these regions.

Around the high-count region, there appears to be an intermediate-count region. The presence of this area can be attributed to two main hypotheses. On one hand, the radioactive surface of the source might not have been perfectly aligned with the collimator aperture. Since the source was positioned manually, it is possible that it was not perfectly centered with respect to the hole, causing a portion of the strontium volume to be shielded by aluminum. On the other hand, it is possible that the radioactive material is not uniformly distributed throughout the source volume. This inhomogeneity could result in areas with lower activity. In both of these cases, the count rate is significantly reduced, but the area can still be visually identified.

The calculated projections also facilitate the verification that the area described by the collimated beam is well distinguishable from the background. It can be observed that the profiles exhibit distinct flat peaks that stand out to the low-count surrounding areas.

To extract the relevant information the two obtained projections were fitted using a super-Gaussian distribution. This type of distribution aims to generalize the Gaussian curve even in cases where the data has a flatter distribution at the peak. The super-Gaussian function is defined as [118]:

$$F(x, A, \mu, \sigma, n) = A \exp\left[-\left(\frac{|x-\mu|}{\sigma}\right)^n\right].$$

The fit appears to adequately match the data, as also indicated by the χ^2 statistical test. The performed interpolation easily yields the center and amplitude that characterize the fitted distributions, summarized in Table 4.5. The amplitude of the curves can be estimated by calculating the Full Width Half Maximum (FWHM). Specifically, in the case of a super-Gaussian distribution, the FWHM can be calculated as [118]:

$$\text{FWHM} = 2\sqrt[n]{\ln(2)}\sigma.$$

The associated error is inferred using error propagation theory.

The information extracted from the conducted analysis is summarized in Table 4.5.

	Center (mm)	**FWHM** (mm)
Projections onto *x*	-0.24 ± 0.04	3.0 ± 0.1
Projections onto *y*	1.22 ± 0.03	3.37 ± 0.07

Table 4.5: FWHM and center coordinates of the profiles of the 2D image obtained using a ^{90}Sr source during the ALPIDE detector tests. The source is positioned 2 mm away from the detector surface.

A brief observation can be made regarding the amplitude of the two studied projections. As evident from Table 4.5, the FWHM of the obtained profiles are different from each other and larger than the diameter of the collimator hole. The first difference can be partly explained by statistical effects (a larger number of events would have allowed for a more stable trend) and partly by potential manufacturing limitations of the support, which may not be perfectly symmetric. The fact that the obtained image has a larger diameter than expected can be trivially explained by the effect of the distance between the source and the detector. Being placed on top of the support at a distance of 2 mm, with a similar thickness, the electrons passing through the collimator hole traverse a layer of air around 4 mm thick. This distance may result in a significant increase in the beam's cross-section when it impacts the detector. However, this effect can be further studied and confirmed through the Monte

Carlo simulations performed.
The same image was in fact reproduced by simulating the experimental setup as described above. A relevant parameter to extract was the number of decays observed during the acquisition period. The total acquisition time was 26 minutes. As previously mentioned, unfortunately, the instability of the setup allowed only for short measurements with a sufficiently long dead time set at 98%. The system's fragility thus limited the data collection to a narrow time window. Fortunately, the available source had a nominal activity of 0.1 μCi (equivalent to 37 kBq), allowing the observation of a total of 1,154,100 events. Although only a fraction of all produced particles reaches the detector surface due to scattering effects, the total number of observed events is adequate to generate a meaningful image. The Monte Carlo simulation was conducted using a total of 1.1×10^6 events and based on the discussed experimental setup modeling.
The raw image simulated via Geant4 is collected in the Appendix: Figure 6.1 shows a direct comparison between the original and the simulated images with a source of ^{90}Sr. For a more comprehensive comparison between the two images, the profiles of the simulated two-dimensional image were analyzed. The projections along the x and y axes were obtained using the same approach described earlier. The curves resulting from the performed projection procedure are shown in Figure 4.19 and compared with the profiles extracted from the original ^{90}Sr image.

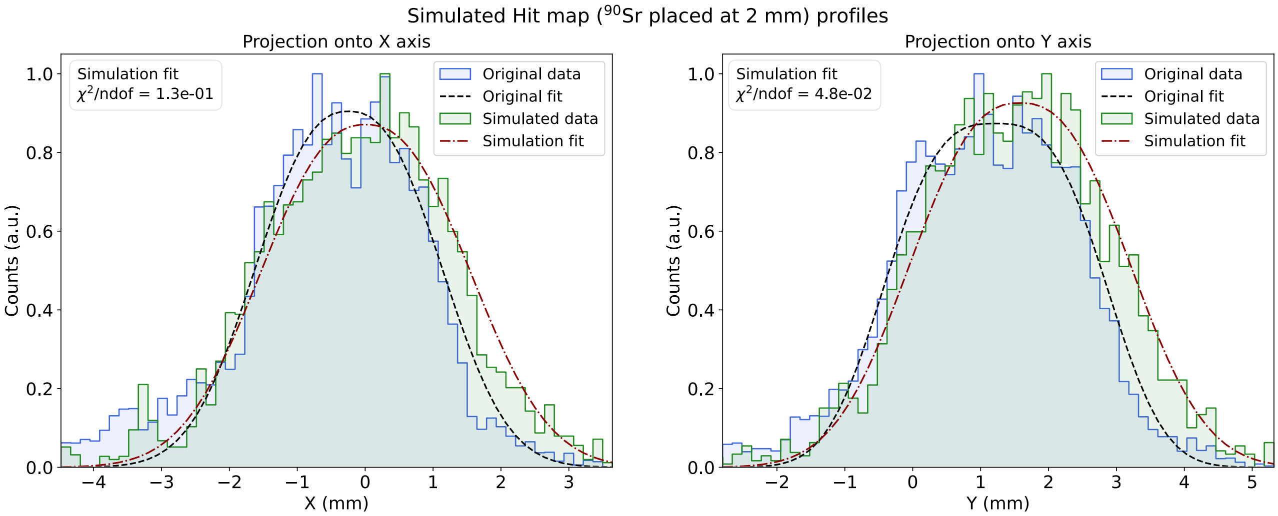

Figure 4.19: Comparison between the profiles of the original and simulated ^{90}Sr images. The developed Geant4 simulation replicates the setup of tests performed with the ALPIDE detector using a ^{90}Sr source. The source is positioned 2 mm away from the detector surface. The profiles are fitted using a super-Gaussian distribution (generalized Gaussian function).

The comparison between the obtained results allows for the observation of differences between the real and simulated outcomes.
It is immediately evident that the positioning of the source relative to the collimator aperture appears to be inaccurate in the performed simulation. In the Geant4 modeling, it was assumed that the source was centered with respect to the opening in the aluminum support, but this is not confirmed by the experimental measurements. During data acquisition, it was not feasible to identify and measure the exact position of the source relative to the collimator aperture due to safety reasons. Although the positioning was carried out to align the source and collimator as accurately as possible, a misalignment between the two is evident. Therefore, it is logical to expect that the simulation may not replicate the emission area precisely due to this misalignment.
Nevertheless, the simulation predicts the data trend quite accurately both in the vicinity of the electron

beam cross section and in the surrounding area, which defines the entire source surface, except for the alignment issue with the collimator aperture. The simulation reproduces, with sufficient precision, the noisy background around the high-count region.

To conclude the visual comparison, a quick observation can be made on the difference present in the raw images (Figure 6.1) related to the counts in the surface describing the impacting beam. In the high-count region, the simulation predicts relatively higher frequencies compared to the experimental data. This behavior is hypothesized to be connected to an imprecise determination of the total number of observed decays during the measurement. In particular, the calculation of events required for the Monte Carlo simulation utilized the nominal activity of the used source. This estimation might be imprecise for two reasons. Firstly, the source is uncertified, introducing a potential error of ± 20% in the actual activity. Secondly, the source was purchased years ago and has experienced gradual degradation in its activity over time. Therefore, this variation could plausibly explain the observed difference.

To conclude the comparison between the image obtained with ^{90}Sr and the simulated image, it is interesting to compare the predictions provided by the performed super-Gaussian fits on the image projections. The interpolation appears to accurately describe the trend of the original and simulated data, and provides information about the center and width of the curves, as described earlier. While the information gathered for the experimental image is already presented in Table 4.5, Table 4.6 summarizes the data collected from the simulated image.

	Center (mm)	**FWHM** (mm)
Projections onto $\boldsymbol{x}$	-0.01 ± 0.03	3.37 ± 0.09
Projections onto $\boldsymbol{y}$	1.58 ± 0.03	3.48 ± 0.07

Table 4.6: FWHM and center coordinates of the profiles of the 2D image obtained through Monte Carlo simulations. The developed GEANT4 application replicates the setup of tests performed with the ALPIDE detector using a ^{90}Sr source. The source is positioned 2 mm away from the detector surface.

The comparison between the projections obtained from the simulated image and the profiles of the original image (Figure 4.18) reveals a reasonable agreement between the simulations and the data. Apart from some statistical fluctuations, the simulated profiles seem to closely mirror the experimental observations. Particularly noteworthy is the fact that, for both projections (along the y-axis and along the x-axis), the estimated FWHM values of the real and simulated distributions are compatible within 3σ. However, there is a notable discrepancy in the estimates of the centers. This discrepancy can be attributed to an underestimation of the error, which does not account for the uncertainty in the measurements used to determine the positioning of the collimator and the source with respect to the detector. The dimensions of the simulated setup inherently carry errors due to the measurement process, which affects the positioning of the electron beam relative to the detector surface. Hence, the difference observed between the experimental case and the simulation appears to be explained by these factors.

The simulation developed to analyze the setup with a ^{90}Sr source seems to provide a good prediction of the experimental results. However, an additional analysis was carried out using data obtained with a ^{137}Cs source, known for its γ component, to further verify the accuracy of the simulations in a different scenario.

The image obtained using the previous experimental setup with the introduction of the cesium source is depicted in Figure 4.20. To further examine the image obtained with the ^{137}Cs source, the same analysis as that carried out for the strontium source was applied. It is interesting to study the profiles of the obtained distributions to assess parameters of interest such as the center and amplitude. Figure 4.20 highlights the projection ranges and illustrates the obtained projections, including the super-Gaussian fits applied in analogy to what was done previously.

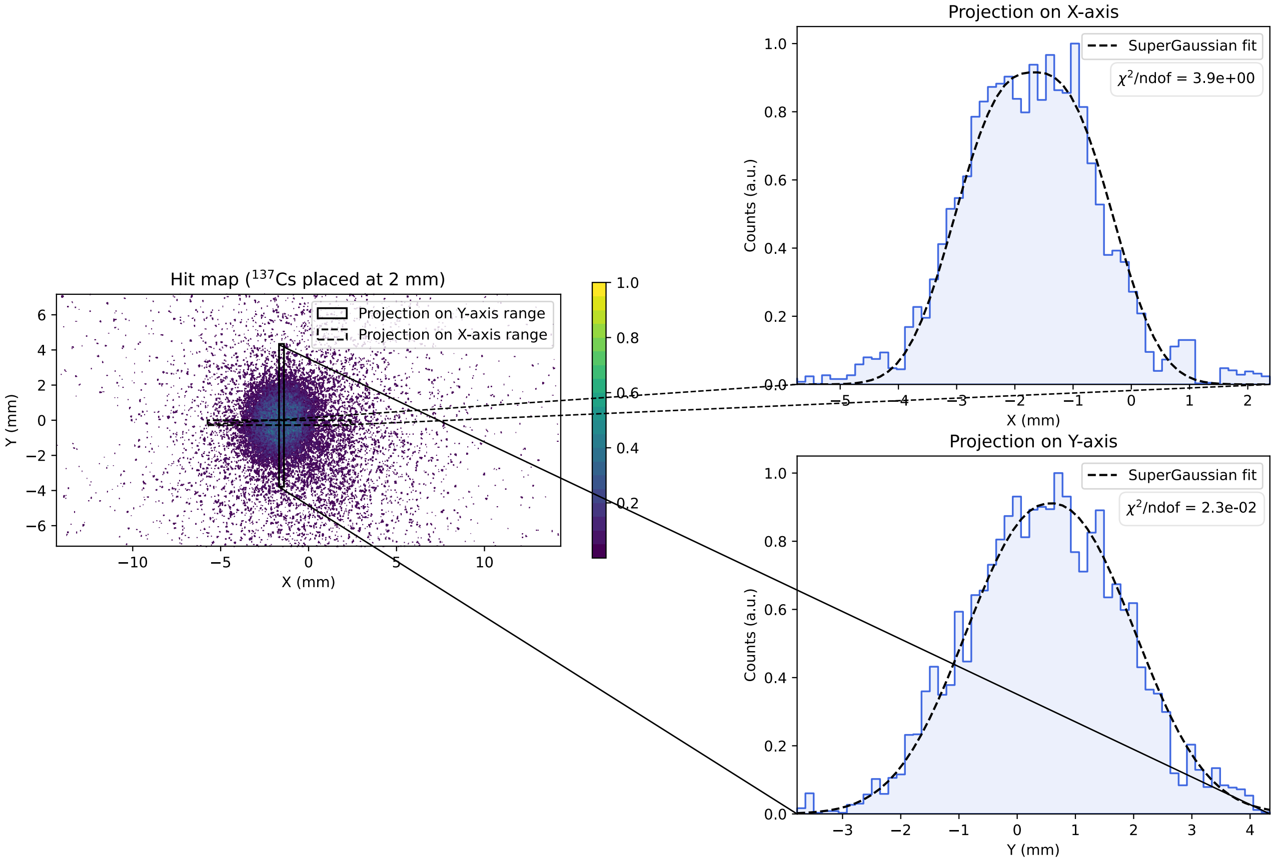

Figure 4.20: Profiles (and projection ranges) of the 2D image obtained using a ^{137}Cs source during the ALPIDE detector tests. The source is positioned 2 mm away from the detector surface. The two profiles are fitted using a super-Gaussian distribution (generalized Gaussian function).

The two-dimensional image appears much sharper than the previous case with ^{90}Sr. In the middle of the image, a marked high-count region is present, associated with the surface where particles that manage to pass through the collimator aperture reach the detector. From the image, it can be inferred that the positioning of the source is more centered compared to the setup with the ^{90}Sr source, even though in the region to the right of the high-count area, a higher density background is observed. This could be justified by a misalignment of the source itself.

The area produced by the direct beam is clearly distinguishable from the background, which exhibits a lower concentration compared to the previous image. This behavior can be explained by a combination of effects. The particles emitted by the cesium source, in particular the photons that can more easily pass through the protective volume of the source compared to beta particles, are on average less energetic than the electrons produced by the ^{90}Sr source. This energy difference means that the collimator shields more efficiently particles in the unperforated volume. In addition to this dynamic, it must be considered that the source is of a different type than that of strontium. In this case, the radioactive material is shielded by a protective volume that attenuates the ionizing radiation produced, affecting the energy of the particles and preventing some electrons from exiting the plastic volume itself. This different behavior can justify the difference in terms of background observed between cesium and strontium sources and can be tested and verified through subsequent Monte Carlo simulations.

The profiles of the experimental image along the x and y axes have been interpolated with a super-Gaussian function that allows the description of the flat peak present in the two histograms. Despite the limited statistics available, one can observe that the super-Gaussian distribution can provide a good description of the data's behavior, especially in high-count regions. The performed interpolations estimate the center and FWHM of the two curves, providing insight into the position and, most importantly, the width of the studied image. The data are summarized in Table 4.7.

	Center (mm)	**FWHM** (mm)
Projections onto x	-1.67 ± 0.02	2.84 ± 0.06
Projections onto y	0.57 ± 0.03	3.26 ± 0.08

Table 4.7: FWHM and center coordinates of the profiles of the 2D image obtained using a ^{137}Cs source during the ALPIDE detector tests. The source is positioned 2 mm away from the detector surface.

The estimated center is noticeably distant from the computed center in the case of the ^{90}Sr source. This difference is justified by a shift in the setup that occurred during the time interval between the two measurements. Likely, in the days between the two data acquisitions, the detector slightly shifted its position within the box, altering its relative position to the collimator, which is soldered to the box. This clearly affects the beam's position in relation to the detector, making the measurements with the ^{90}Sr and ^{137}Cs sources independent from each other.

On the other hand, the width of the extrapolated distributions is consistent (within 3σ) with what was observed in the strontium case, confirming, along with the simulations, that the diameter of the beam section almost doubles when particles interact with the chip.

The image was reproduced through GEANT4 simulation. As mentioned earlier, the setup was slightly (and inadvertently) modified during the ^{137}Cs measurements. This difference had been observed during the data collection, prompting measurements of the setup components' dimensions to update the simulation. The modeling of the cesium source setup was developed taking into account a different geometric configuration compared to the strontium scenario and incorporating the measured modifications.

In this scenario, it was necessary to compute the total number of decays observed during the measurements, following a procedure similar to that described for the ^{90}Sr source. The nominal activity of the cesium source is 0.05 μCi (equivalent to 18.5 kBq). In this case, the total measurement time is 91 minutes, broken down into a series of short acquisitions to ensure system stability. However, a high dead time fraction of 98% had to be maintained. Under these conditions, the total number of observed ^{137}Cs decays is 2,020,200 events, which provided a clear image with good statistics.

The Monte Carlo simulation hence utilized the updated setup model, considering 2×10^6 events. The resulting image is compared with the experimental results in the Appendix, in Figure 6.2.

A more comprehensive and quantitative comparison can be obtained by studying the projections of the two two-dimensional images along the x and y axes. By superimposing the extrapolated profiles, it is possible to verify more directly the differences between the experimental image and the simulated one. In addition, the plots also include super-Gaussian fits performed for both curves so that the comparison between the interpolations on the data can also be visualized. The comparison between the experimental and simulated projections computed for the ^{137}Cs setup is presented in Figure 4.21.

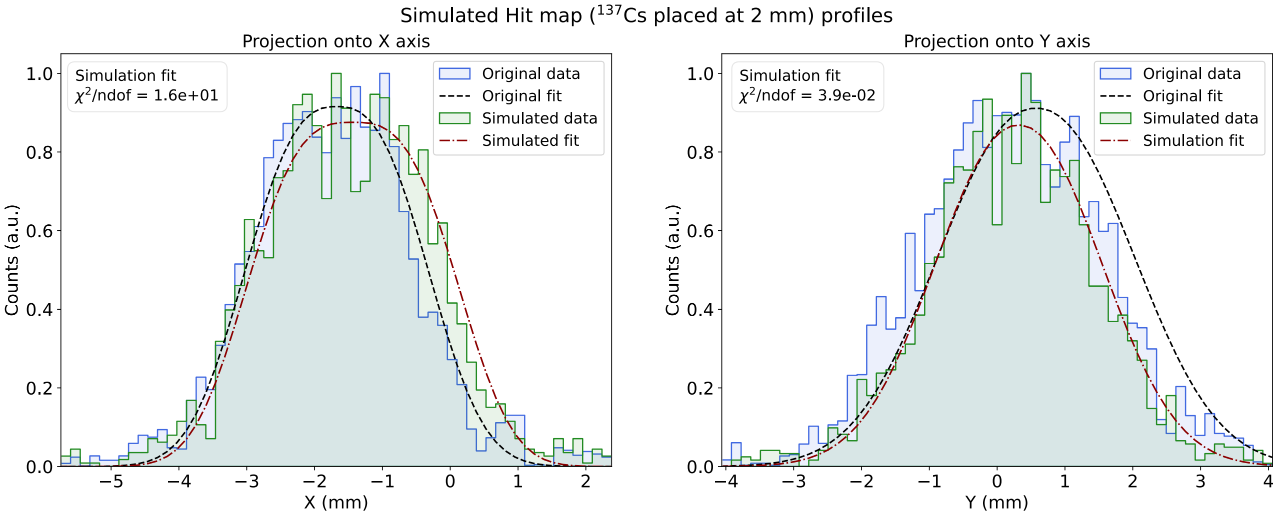

Figure 4.21: Profiles (and projection ranges) of the 2D image obtained through Monte Carlo simulations. The developed GEANT4 application replicates the setup of tests performed with the ALPIDE detector using a ^{137}Cs source. The source is positioned 2 mm away from the detector surface. The two profiles are fitted using a super-Gaussian distribution (generalized Gaussian function).

From the comparison between the two images, it can be observed that the simulation can replicate the experimental data. In this case, there is excellent adherence between the experimental data and the simulated data. The simulated histogram successfully reproduces the region of hits corresponding to the beam incidence area and the low-count background. The greatest distance seems attributable to a misalignment along the y-axis between the simulated and real setup.

The fit super-Gaussian function describes the simulated data, as confirmed by statistical tests. The fit parameters, provided in Table 4.8, enable an investigation of the acquired distribution and its comparison with the experimental data.

	Center (mm)	**FWHM** (mm)
Projections onto x	-1.41 ± 0.03	3.20 ± 0.08
Projections onto y	0.32 ± 0.03	2.91 ± 0.09

Table 4.8: FWHM and center coordinates of the profiles of the 2D image obtained through Monte Carlo simulations. The developed GEANT4 application replicates the setup of tests performed with the ALPIDE detector using a ^{137}Cs source. The source is positioned 2 mm away from the detector surface.

The information extracted from the simulated distributions allows for a direct comparison with the profiles of the experimental image, whose center and width have been summarized in Table 4.7. Similar to the case of the ^{90}Sr source, the simulation shows an inability to precisely predict the center of the experimental data. However, this limitation can be attributed to an error introduced during the measurement of the setup dimensions, which is challenging to include in the process.

On the other hand, the amplitude of the curve is well reproduced by the simulation, providing a distribution with a FWHM compatible within 3σ with the experimental one. This is an interesting aspect that confirms the simulation's capability to model the trajectories of the particles reaching the detector and the processes of hit generation in that region, even when dealing with γ-rays interacting with the device.

The analysis conducted allows for some conclusive considerations on the obtained results. The

ALPIDE acquisitions have achieved two main objectives. On one hand, the ALPIDE detector was successfully integrated into a functioning DAQ system, with custom firmware designed for the chip's characteristics. It was observed during the conducted measurements that the system is still unstable and requires further improvements for secure and more manageable data acquisition. On the other hand, the designed simulation was tested with real data. As discussed, the modeling of the detector developed in GEANT4 provides a good reproduction of the object under investigation. The simulated images appear capable of replicating the experimentally derived information in the most relevant aspects. One limitation of the simulations lies in the inability to precisely know all the aspects that characterized the setup, both in terms of the dimensions of the various components, subject to errors and regarding the information about the available sources. By incorporating these constraints, it can be verified that the designed GEANT4 software provides accurate modeling of the ALPIDE chip and allows predictions about its behavior in the context of future experiments that ISOLPHARM will develop.

Chapter 5

Detector characterization through Monte Carlo simulations

In the upcoming years, the beta detector under investigation will be employed in in-vitro experiments as part of the ISOLPHARM project. ISOLPHARM aims to develop a comprehensive radiopharmaceutical that can be utilized in clinical settings, requiring specific tests to ensure product effectiveness and study potential side effects. Selective deposition at the tumor site is a crucial requirement for any Targeted Radiation Therapy drug. Therefore, the forthcoming in-vitro ISOLPHARM experimental campaign seeks to evaluate the selectivity of the studied prototype by examining the drug distribution within a cell culture containing cancerous regions. To obtain information regarding this distribution, the analyzed beta detector must accurately determine the location of the ^{111}Ag radioisotope. The objective is to produce high-resolution two-dimensional images, which can be compared to microscopy images to identify the regions where the radiopharmaceutical has deposited.

The purpose of the developed Geant4 application is to investigate the capabilities of the beta detector under development. The main objective is to characterize the detector-cell culture system to understand its features and potential limitations. To achieve this, a model of the future detector and two distinct types of cell cultures (2D and hydrogel-based) were implemented in Geant4. Through the use of Monte Carlo simulations, it is possible to reproduce the deposition of the radiopharmaceutical at the cellular level, simulating the decay of ^{111}Ag within the cellular volumes where the drug is hypothesized to be internalized. This approach allows for the study of the instrument's response and performance within an in-vitro experimental scenario.

This chapter presents the results obtained from the study of the performance of the investigated detector using Monte Carlo simulations. It aims to provide insights into the detector's behavior, advantages, limitations, and potential design considerations for future experiments.

5.1 Energy deposition and threshold optimization

As initial analysis to examine the beta detector performance, it was necessary to evaluate the potential benefit related to the introduction of an energy threshold for the collected signal, and eventually infer which threshold should be considered. To investigate this possibility, a single ALPIDE chip was modeled in the Geant4 simulation to assess its response in relation to the deposition of ^{111}Ag within a single cell. The objective was to study the energy distribution deposited by electrons generated in the decay of the ^{111}Ag radioisotope (and potentially by photons produced in the subsequent decay of ^{111}Cd) within a single ALPIDE pixel, and understand how the imposition of a threshold may affect the single-cell image produced by the detector. The same analysis was conducted for both two- and three-dimensional cell cultures to determine the most suitable setup for each alternative.

5.1.1 Threshold optimization for the two-dimensional cell culture scenario

The initial scenario under analysis consisted of the traditional cell culture setup, modeled as described in Section 4.3.2. The first step of the analysis involved assessing the amount of energy deposited by the generated electrons (and potentially photons) within the beta detector's pixels. For each hit pixel, the energy released by the interacting particles within its volume was evaluated. The histogram representing the distribution of the energy deposited within every hit individual ALPIDE pixel is illustrated in Figure 5.1. To ensure sufficient statistics, a total of 10^7 events, which correspond in the analyzed simulation to 10^7 decays of the ^{111}Ag radioisotope within the cellular volume, were simulated. Regardless, in the subsequent analyses, it was preferred to normalize the obtained histograms by ensuring that the bin with the highest count in each histogram was associated with an arbitrary unit of one: in Figure 5.1 (and subsequent figures), these units are indicated as a.u. (arbitrary units).

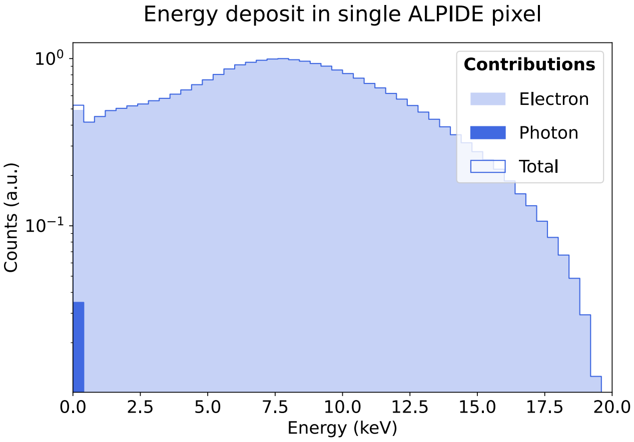

Figure 5.1: Energy deposited by the particles produced in the ^{111}Ag decay in every hit ALPIDE pixel. The ^{111}Ag radioisotope is contained in a single cell placed at the center of a two-dimensional cell culture. The single contributions from electrons and photons are plotted separately.

The distribution of energy exchanged between the interacting particles and the sensitive material reflects the contributions of the two particle types that can be produced in the decay of ^{111}Ag, *i.e.* electrons in silver decay and γ-rays produced during the de-excitation of ^{111}Cd.

The energy histogram indicates that the energy released by particles traversing the detector thickness constitutes a relatively reduced fraction of their total energy. Considering that the average β-emission energy for the ^{111}Ag decay is 360 keV and the two most probable γ de-excitations of ^{111}Cd have energies of 245 and 342 keV [22], only a few percentage units of the energy with which the particles under analysis are produced are lost in the detector material. This observation is consistent with the design intent of the ALPIDE detector, which aims to minimize energy variations for particles passing through it by employing a very thin total thickness.

It can be observed that the distribution of energy deposited by electrons exhibits a central peak around 7.75 keV. The shape of this distribution can be explained by the deceleration that electrons undergo as they traverse the material, including the SiO_2 layer for integrating the read-out electronics, between the emission point and the sensitive volume. As the kinetic energy of beta particles decreases, the stopping power increases, leading to a higher exchange of energy during interactions within the pixel's sensitive volume.

Conversely, photons tend to exchange smaller amounts of energy with the traversed media. It is expected that the energy deposition associated with photons interacting with the sensitive volume is lower than that of beta particles. This hypothesis is supported by the distribution shown in Figure 5.1, where it can be observed that photons produce hits with lower fractions of energy released in the pixel. The number of hits caused by photons is extremely reduced compared to those produced by electrons. Monte Carlo simulations have shown that in most cases (i.e., 90% of the time) photons interacting with the ALPIDE detector do not deposit energy within the sensitive volume and pass through the chip undetected.

This behavior can be explained by considering two principal factors. Firstly, the type of detector under analysis is not designed and optimized for photon detection. The ALPIDE is a silicon detector (low atomic number) characterized by an extremely thin thickness (50 μm) and an even thinner sensitive region(25 μm when considering the entire epitaxial layer). The cross section associated with photon interactions with the detector medium is very low. Consequently, in most cases, γ-rays traverse the MAPS volume with negligible energy deposition within the instrument. Excessively small energy depositions are treated as negligible by the Monte Carlo simulation, resulting in no hit registration.

On the other hand, in some instances, photons produced during the de-excitation of ^{111}Cd can interact via photoelectric effect or Compton scattering with the materials they traverse before reaching the detector. By altering their trajectory, such γ-rays might go undetected. GEANT4 can model photon-matter interaction processes in detail, simulating also the trajectories of the beta particles released in the interaction processes. The electrons that absorb the photon's energy can reach the ALPIDE, influencing the simulated distribution of the recorded energies. Therefore, the photon can remain unrevealed, even though a portion of its energy is released within the detector.

The distribution of the energy exchanged between the detected particles and the device provides insight into the threshold levels that can be introduced without removing a significant number of relevant hits. The inclusion of an energy threshold is a useful parameter to eliminate hits caused by external noise sources and electron scattering processes between different pixels of the ALPIDE. Due to their light mass, electrons are particles that tend to easily deviate from their trajectory when interacting with media. For the application under analysis, it is interesting to limit the number of multiple hits generated by a single electron emitted from the source. The following study aims to comprehend how the introduction of a threshold influences image production and whether it can impact the reduction of scattering effects within the sensitive volume.

To analyze how the introduction of a threshold affects the number of ignored hits, the percentage of recorded hits that would be discarded when a given threshold is imposed was calculated. Figure 5.2 illustrates which regions of the energy deposition distribution would be eliminated by the introduction of a range of possible thresholds and the corresponding percentages of removed hits.

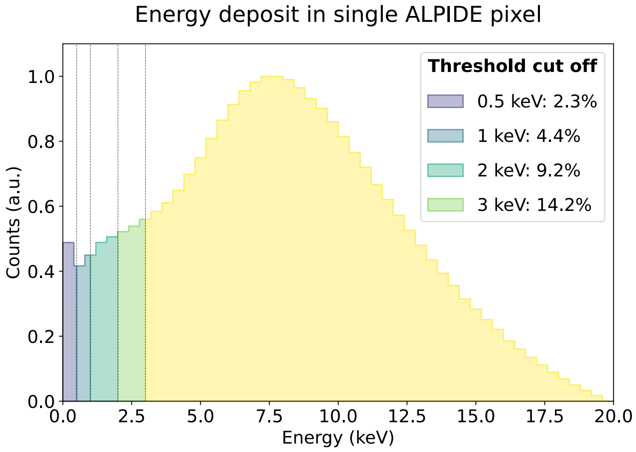

Figure 5.2: Energy deposited by the particles produced in the ^{111}Ag decay in every hit ALPIDE pixel. The ^{111}Ag radioisotope is contained in a single cell placed at the center of a two-dimensional cell culture. The threshold cut-off describes the percentage of hits that would be discarded by selecting the corresponding energy threshold.

By maintaining low threshold values (a few keVs), it can be observed that the percentage of ignored hits remains relatively low, exceeding 10% only when considering 3 keV. However, it is necessary to consider that in a real application of the detector for in-vitro measurements, acquisition times will not allow for a very high count rate. The ability to eliminate low-energy hits needs to be balanced with the avoidance of discarding too many potentially interesting events.

To understand how much the introduction of a threshold would affect the quality of the produced image, Monte Carlo simulations applying different energy thresholds for the ALPIDE detector were carried out. The objective was to characterize how the image produced by a single cell would have been affected by the chosen threshold and the corresponding events cut-off.

For each selected energy threshold, a simulation was conducted that disregarded all hits caused by particles depositing an amount of energy lower than the chosen threshold level. For each simulation, a two-dimensional histogram was saved, collecting the number of hits recorded for each pixel during the acquisition. The result is an image of a single cell present in a two-dimensional culture produced by a single ALPIDE chip.

Figure 5.3 shows a comparison between the different outcomes considering the distinct threshold options in the case of a two-dimensional culture source.

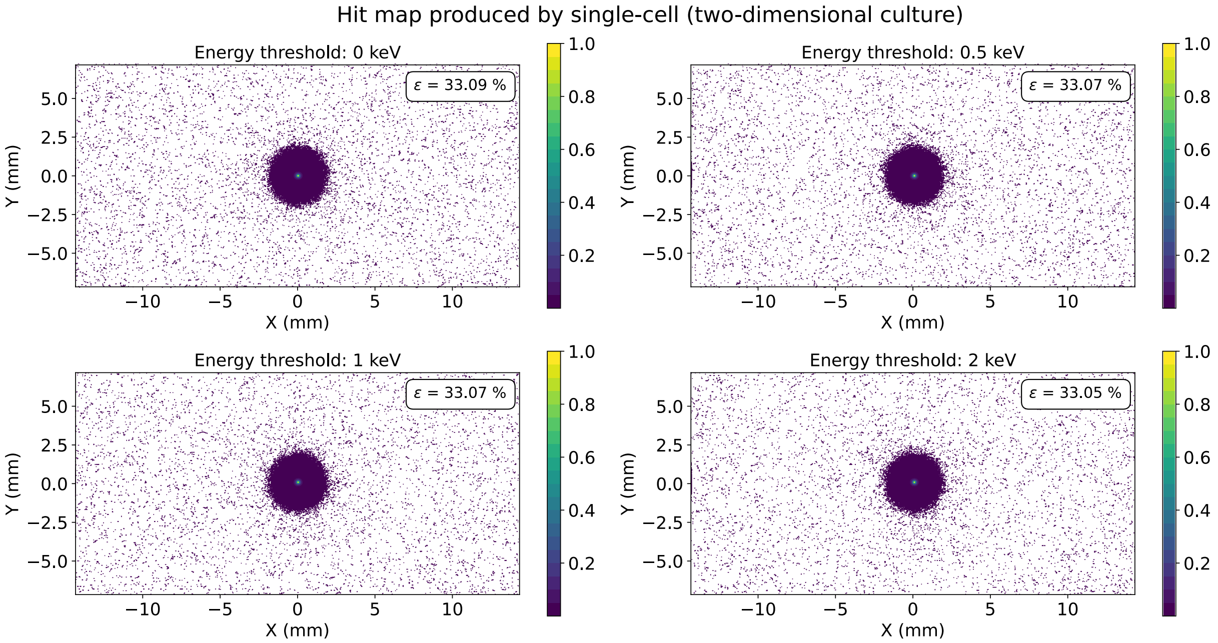

Figure 5.3: Comparison between single-cell images obtained setting different thresholds in the case of a single cell placed in a two-dimensional cell culture. ε represents the fraction of effectively detected particles with respect to the total number of particles produced in the ^{111}Ag decays (both electrons and photons, while antineutrinos are neglected).

The obtained images consist of two-dimensional histograms that allow for the localization of the position of the emitting cell. The peak produced by the individual cell is highly pronounced and surrounded by a wide region of smaller counts.

It can be observed that the introduction of a threshold does not significantly affect the type of image produced. In an ideal acquisition with a sufficient number of events to achieve statistical significance, it can be noticed that the obtained result is visually the same for the tested thresholds.

The exhibited plots also include a computation of the total detector efficiency, denoted as ε, which represents the ratio between the number of particles produced in the decays of ^{111}Ag and the number of particles detected.

The total number of produced particles includes both the electrons emitted during the decay of the

^{111}Ag radioisotope and the photons released during the possible subsequent de-excitation of ^{111}Cd (while the antineutrinos emitted during the $\beta-$ decay are excluded from the sum because of the extremely unlikely probability to detect them). Considering that the images are generated by simulating a total of 10^7 events and the probability of producing the excited state of ^{111}Cd is 8.1% [22], this results in a total number of released particles as the sum of 10^7 electrons and 0.081×10^7 photons (a total of 108.1×10^5).
The information provided by ε reveals that the introduction of a threshold (up to 2 keV) does not significantly affect the number of particles that the detector is capable of effectively detecting. The total efficiency of the individual ALPIDE chip remains unchanged at around 33%. This observation may appear contradictory to the cutoff percentages observed in Figure 5.2; however, this difference can be explained by considering the scattering processes that occur within the detector.
When traversing a material, electrons interact with the atoms present in the medium, altering their trajectory. Due to their low mass, beta particles experience significant deflection when interacting with other particles, resulting in a non-linear and highly segmented path. Thus, it cannot be ignored that the various scattering processes that the particle undergoes within the sensitive volume may result in the activation of multiple pixels. As previously mentioned, one of the potential benefits of applying an energy threshold is to reduce the occurrence of the multiple hits effect caused by a single interacting particle. To analyze this possibility, the simulations evaluated the number of hits recorded for each individual event (corresponding to the decay of a ^{111}Ag radioisotope). Figure 5.4 compares the distributions of the number of hits observed per single event in the absence of a threshold and in the case of an energy threshold of 1 keV.

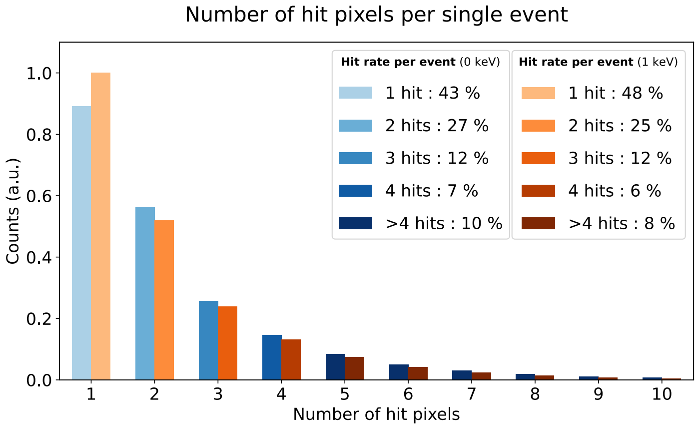

Figure 5.4: Comparison between the number of pixels activated per single event (^{111}Ag decay) generated in the case of an energy threshold of 0 and 1 keV. The ^{111}Ag radioisotope is contained in a single cell placed at the center of a two-dimensional cell culture. For one or more hits the number of hits rate per event is presented.

When no threshold is applied to the detector, it can be observed that in over 50% of cases, a single beta decay is associated with the observation of two or more hits within the detector. While in 8.1% of cases, the decay of the ^{111}Ag radioisotope also results in the production of a γ particle that could lead to the detection of both particles, the fractions of events associated with two hits in the detector cannot be solely explained based on this observation. It is evident that scattering effects within the volume of the ALPIDE cause the majority of the particles to produce two or more hits within the detector.
This behavior can explain the effect of the introduced threshold on the total efficiency of the detector, ε. When observing the distribution of deposited energy per hit within the detector (Figure 5.2), it is essential to consider that a single hit does not necessarily correspond to the detection of a single particle. Consequently, in over half of the cases where the passage of a particle is registered, more

than one hit is produced due to scatterings in the materials. The cutoff percentages inferred in Figure 5.2 refer to the number of hits discarded in an acquisition when a given threshold is introduced. On the other hand, when studying the trend of the total efficiency in relation to the applied threshold (ε in Figure 5.3), one obtains information about the number of particles effectively observed, regardless of whether they activated only one pixel or more.

To quantitatively understand the impact of introducing an energy threshold on the elimination of multiple hits associated with a single cell, one can directly compare how the distribution of the number of hits recorded per event varies with the threshold, as shown in Figure 5.4. The plot compares the conditions of no threshold and a threshold set at 1 keV. It can be immediately observed that the 1 keV threshold reduces the frequency of hits equal to or greater than 2 by more than a few percentage points. This demonstrates that the implementation of even a low threshold affects the number of pixels activated per particle, eliminating hits due to scattering phenomena within the device and increasing the number of single hits. This effect is interesting and represents the main advantage of introducing an energy threshold.

The possibility of reducing particle scattering processes within the MAPS pixels by applying an energy threshold needs to be balanced with the need for sufficiently fast acquisitions to facilitate in-vitro measurements. For this reason, when considering the implementation of a threshold, the possibility of not eliminating an excessive number of total events that could represent meaningful measurements should also be evaluated.

To summarize, the study conducted on single-cell two-dimensional culture has provided information about the behavior of particles interacting with the detector and the potential advantages and limitations of applying an energy threshold to the device. It was observed that the introduction of a threshold allows for the partial exclusion of multiple hits caused by particle scattering within the sensitive volume, which leads to the activation of numerous pixels for a single particle.

Based on the observations made so far, it was chosen a threshold of 1 keV for the two-dimensional cell culture scenario. This choice specifically allows the removal of multiple hits produced by the same particle that activates multiple pixels, without significantly reducing the actual number of detected particles. This threshold will be applied to all subsequent analyses.

5.1.2 Threshold optimization for the three-dimensional cell culture scenario

A similar analysis was carried out to determine an appropriate threshold for the three-dimensional cell culture scenario. In the case of three-dimensional cell culture, a hydrogel-based culture model has been developed, which is the culture model selected by the ISOLPHARM project for future in-vitro experiments. The culture was modeled as a hydrogel volume deposited on an aluminized mylar film, which aims to prevent possible contaminations of the detector and simultaneously screen it as much as possible from background photons. The mylar layer introduced a thickness of 50 μm between the instrument and the cell culture. Further details on the type of material that can be used and how the introduction of a protective film impacts image quality are discussed in Section 5.3.

When considering a three-dimensional cell culture, it is important to note that the cells, in addition to being deposited at various points in the plane parallel to the detector (xy plane), have an additional degree of freedom as they can move along the direction perpendicular to the detector (z-axis). The depth of the cell's position relative to the hydrogel thickness affects the distance between the emission volume and the detector surface, thereby altering the distance that particles must traverse before being detected. The distance that beta particles must traverse can affect the resolution of the produced image due to the increased probability of scattering in the medium. As already observed, being low mass particles, electrons (and potentially photons) tend to significantly alter their trajectory during interactions, leading to a degradation in image quality. Therefore, in the case of three-dimensional culture, the discussed analysis was conducted to evaluate two antithetical scenarios: one where the cell is in contact with the lower surface of the volume and at minimum distance from the ALPIDE (0 μm depth) and another where it is in contact with the upper surface and at maximum distance from the detector (500 μm depth).

For both examined setups, the analysis performed was similar to the one carried out for the two-dimensional cell culture. The first step involved verifying the observed energy deposition in each hit. Again, the same simulation conditions were considered (10^7 total events), studying the contributions associated with the two relevant particles in play, *i.e.* electrons and photons (while still neglecting the contribution of antineutrinos). Figure 5.5(a) illustrates the distribution of energy deposited in individual pixels under the condition of cell adherence to the lower surface of the hydrogel volume (0 μm depth), while Figure 5.5(b) represents the case with a depth of 500 μm.

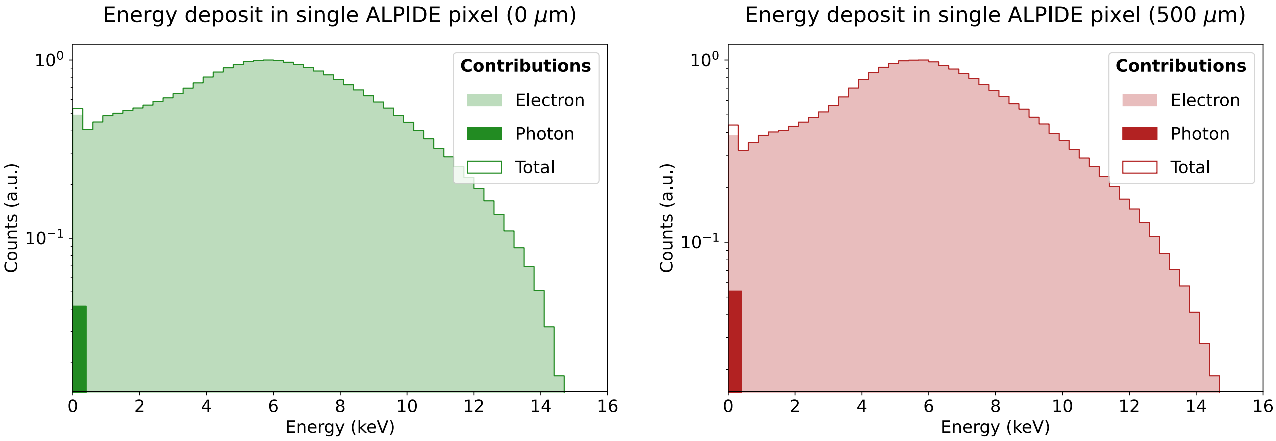

(a) (b)

Figure 5.5: Energy deposited by the particles produced in the ^{111}Ag decay in the ALPIDE pixel closest to the emission point. The ^{111}Ag radioisotope is contained in a single cell placed in contact with the (a) lower or (b) upper surface of a three-dimensional cell culture. The single contributions from electrons and photons are plotted separately.

Even in the case of a cell source included in a hydrogel-based culture environment, it is observed that all particles produced in the decay of ^{111}Ag deposit only a very small portion of their total energy (to the maximum of few percentage points with respect to the total). As discussed earlier, this behavior is justified by the type of detector under consideration and does not negatively impact the ALPIDE's application objective.

Compared to the previous two-dimensional cell culture case, slightly different distributions are observed, with a more pronounced peak shifted to relatively lower energies (around 6 keV). In the three-dimensional case, it can be highlighted that the range of observed energies is different: while previously the maximum deposited energies reached up to 20 keV, in these two plots, the distributions stop around a maximum of 15 keV. This difference in terms of the amount of energy exchanged with the detector is most likely attributable to the analyzed materials, which are different and/or have different thicknesses compared to the two-dimensional cell culture scenario.

When comparing the two plots obtained for cell positions closer and farther from the detector, a broader distribution is observed around the peak in the case of the cell positioned at 0 μm depth in the hydrogel volume. It can be noticed that a shorter distance of the emission point from the surface of the detector causes the energy deposited in the pixels of the device to fluctuate more.

Similarly to the two-dimensional scenario, it can be noticed that the fraction of hits produced by a non-zero energy deposition within the pixel is extremely small for photons. The behavior is very similar to what was discussed earlier. Due to the type of material and the thin geometry of the MAPS, the interaction processes between photons and the detector medium are characterized by extremely low cross-sections and exchanges of very small amounts of energy. The simulation thus confirms what was expected, namely very low energy deposits associated with photons and only a small percentage of gamma radiation interacting and releasing non-zero energy within the sensitive volume.

The energy deposition distributions per pixel provide insights into which values are more suitable for selecting an energy threshold that does not remove an excessive number of useful hits. As in the previous case, the effect of an introduced threshold on the number of hits that would be discarded has been analyzed. Since the energy distributions are similar to the previous scenario, the energy threshold values selected are analogous to what was previously studied for two-dimensional cell culture. Figure 5.6(a) illustrates the regions of cut-off hits in the case of a cell in contact with the lower surface of the hydrogel matrix, Figure 5.6(b) the opposite condition.

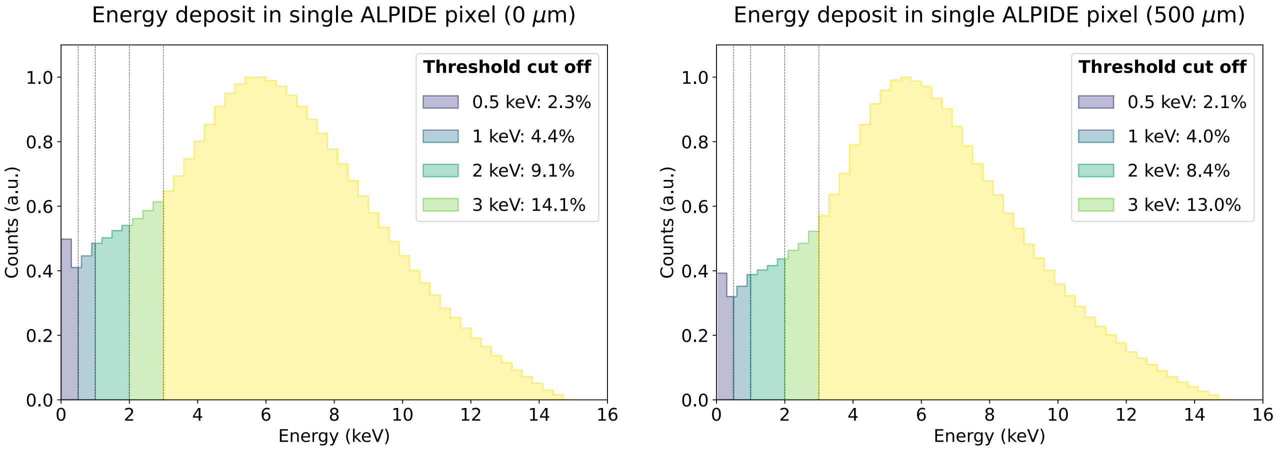

(a) (b)

Figure 5.6: Energy deposited by the particles produced in the ^{111}Ag decay in the ALPIDE pixel closest to the emission point. The ^{111}Ag radioisotope is contained in a single cell placed in contact with the (a) lower or (b) upper surface of a three-dimensional cell culture. The threshold cut-off describes the percentage of hits that would be discarded by selecting the corresponding energy threshold.

The observed cut-off percentages for the configuration with the cell adhering to the lower surface of the culture are very similar to the two-dimensional culture setup. The selected thresholds do not remove an excessive number of hits, allowing for a balance between the utility of introducing a threshold and the need to have a sufficient number of data points in a realistic acquisition scenario.

On the other hand, there is a variation, including in terms of the shape of the distribution, when the emitting cell moves away. As the energy distribution associated with a source placed at maximum distance exhibits a more pronounced peak, the fraction of hits at low energies tends to be lower compared to the minimum distance case. In this scenario, the percentages of eliminated hits are slightly lower than the compared condition.

The next step of the analysis was to assess the impact of introducing thresholds on the produced images and the detector's efficiency for the two studied scenarios. The objective of this study is to investigate whether and how the energy threshold affects the type of map produced and to understand, through an initial comparison, how the position of the cell within the hydrogel impacts the type of image created. Figure 5.7(a) and 5.7(b) depict the single-cell images obtained by applying various energy thresholds for the two antithetic scenarios of a three-dimensional cell culture, *i.e.* the condition where the cell is in contact with the lower and upper wall of the hydrogel matrix, respectively.

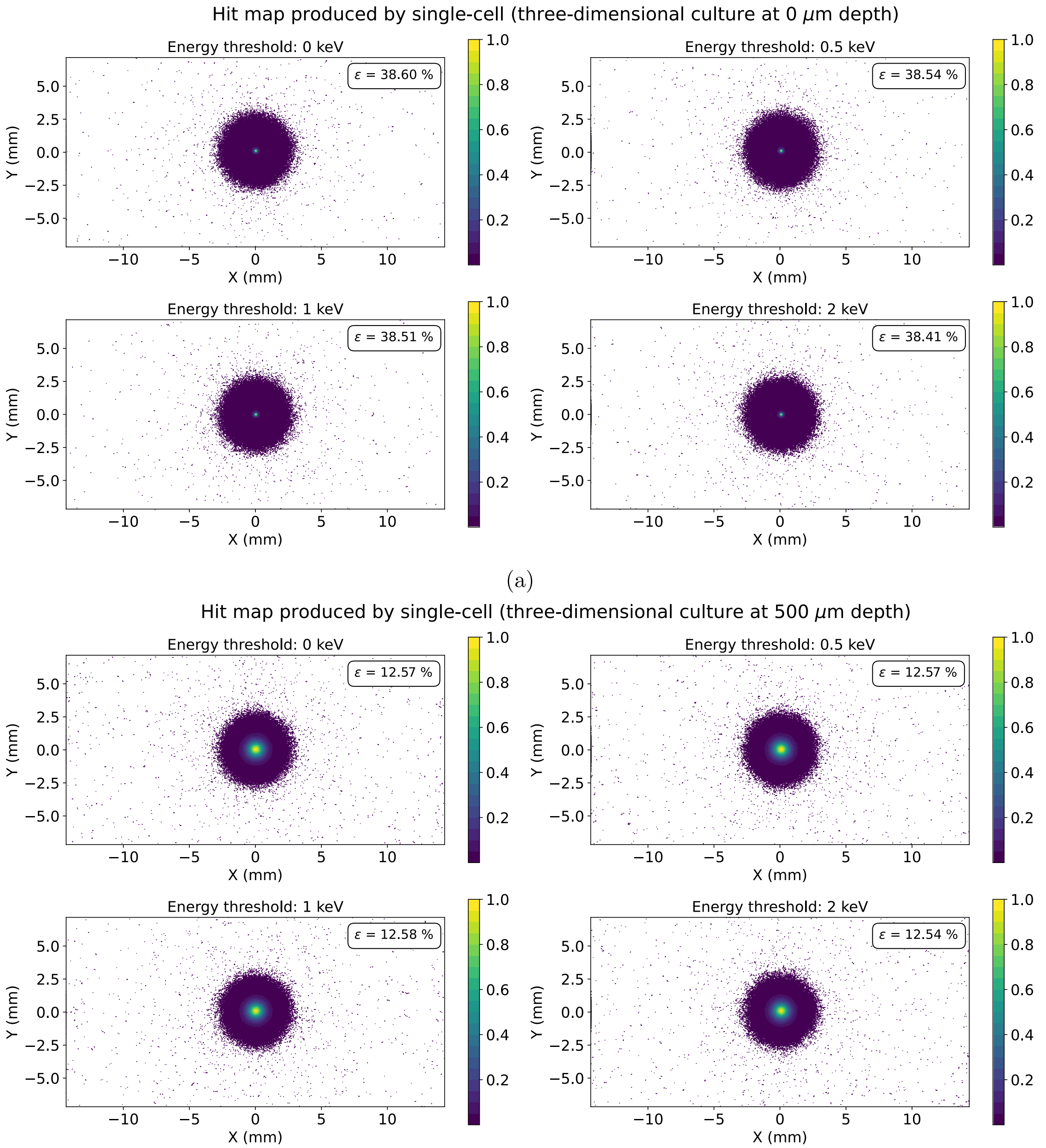

(a)

(b)

Figure 5.7: Comparison between single-cell images obtained setting different thresholds in the case of a single cell placed in contact with the (a) lower or (b) upper surface of a three-dimensional cell culture. ε represents the fraction of effectively detected particles with respect to the total number of particles produced in the ^{111}Ag decays (both electrons and photons, while antineutrinos are neglected).

As expected, when the emission point moves away from the detector's surface, the resulting image exhibits a flatter and more extended peak that makes more challenging the accurate determination of the emission point. On the other hand, images of cells adhering to the lower surface of the hydrogel allow for a better prediction of the cell volume's position, even at a glance. In the condition of null depth, an image very similar to that observed in the two-dimensional cell culture is obtained, but with some interesting differences. The first observation concerns the background counts present at the periphery of the central region: in the three-dimensional case, the frequency of these counts is much lower compared to the two-dimensional case, where the unprocessed image appears noticeably "noisier". However, images obtained from hydrogel-based cell culture exhibit a larger diameter of the central region. Specifically, when directly comparing the images of the two-dimensional and zero-depth three-dimensional cases, there is an approximately 0.5 mm difference in the radius of the produced two-dimensional region. These effects are likely related to the type and thickness of the materials involved in the different scenarios. For instance, it is hypothesized that all the peripheral counts present in the images of the previous traditional cell culture case could be attributed to the presence of walls in the petri dish container required to enclose the culture medium, making laterally emitted electrons more likely to backscatter.

Each of these plots includes the estimation of the total detector efficiency when the indicated threshold is applied. ε is calculated using the same approach discussed for the two-dimensional cell culture case. Once again, in this circumstance, it can be observed that the total detector efficiency decreases much less significantly compared to the cut-off percentages anticipated for the number of detected hits. This phenomenon can only be justified by considering the incidence of multiple hits associated with a single decay event of ^{111}Ag.

To quantitatively examine the hypothesis of the dependence of the number of multiple hits per single event on the energy threshold set for the detector, the distribution of the number of activated pixels for each ^{111}Ag decay was analyzed. Distributions corresponding to the absence of a threshold and a threshold set at 1 keV are compared for both positions considered for the emitting cell. The distribution of the number of hits generated per event for cells at zero depth is shown in Figure 5.8(a), while in the case of cells adhering to the upper culture wall in Figure 5.8(b).

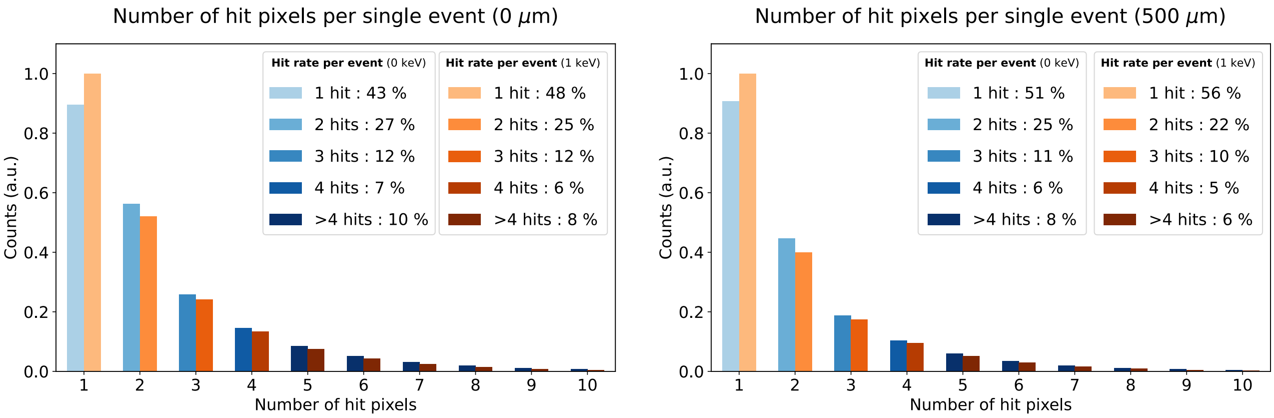

(a) (b)

Figure 5.8: Number of pixels activated per single event (^{111}Ag decay) generated. The ^{111}Ag radioisotope is contained in a single cell placed in contact with the (a) lower or (b) upper surface of a three-dimensional cell culture. For one or more hits the number of hits rate per event is presented.

In this scenario as well, approximately half of the decays show that particles interacting with the chip activate more than one pixel. In both conditions evaluated (0 and 500 μm depth), it is impossible to neglect the contribution given by those events where more than one hit is registered (more than 50% of the cases for cells in contact with the lower surface of the hydrogel, slightly less for cells in contact with the upper surface).

Figures 5.8(a) and 5.8(b) compare the incidence of multiple hits per single event in the case of energy thresholds set at 0 and 1 keV, allowing for an understanding of how the inclusion of an energy threshold affects the distribution. It can be observed that even a reduced threshold of 1 keV decreases the number of hits greater than one for each decay of ^{111}Ag. This modification increases the fraction of events producing a single hit by a few percentage points, eliminating secondary hits generated by particle scattering effects within the detector. Thus, in the three-dimensional culture scenario as well, the direct effect of applying an energy threshold on the frequency of multiple hits is observed.

In conclusion, the analysis conducted on the three-dimensional cell culture scenario has also allowed the evaluation of the interactions that occur between emitted particles and the detector, and to understand the effects of an embedded threshold in the beta detector. Similar to the previous case, the impact of γ-rays produced during the de-excitation of ^{111}Cd and the behavior of particles inside the ALPIDE were studied, observing the frequency of multiple hits for individual events. It has been concluded that introducing an energy threshold tends to mitigate effects related to scattering processes occurring within the sensitive volume by removing hits that are not associated with events of interest but are due to such behavior. In selecting a threshold for subsequent analyses, consideration was given to the need not to remove an excessive number of events that could be meaningful, so as not to excessively impact acquisition times. Evaluating the outcomes of the carried out analysis, it was chosen to adopt the same threshold as for traditional cell cultures, *i.e.* 1 keV. Based on the obtained results, this decision lowers the instances of multiple hits while preserving the detection efficiency of the investigated device. The selected threshold of 1 keV will be employed in all subsequent simulations.

5.2 Detector resolution

Spatial resolution is a critical parameter for detectors employed in imaging applications. Spatial resolution measures the detector's capacity to produce images where two closely spaced objects are separated (*i.e.* resolved) for the human eye. As highlighted in Section 2.3.2, there is no unique method to determine the resolution of an imaging system.

5.2.1 Detector resolution analysis: Point Source Function

A widely employed technique to investigate the resolution of an instrument involves examining how it portrays a point source, usually through an analysis of its point spread function (PSF). The Full Width Half Maximum (FWHM) of the PSF is a commonly used measure, valued for its immediacy, to estimate spatial resolution. While this parameter does not offer information about the shape of the curve that the system generates to represent the point source, it can give an intuitive idea of the width of the function produced. Specifically, it helps predict the extent covered by the point source within the two-dimensional image.

For a preliminary assessment of the resolution potential of the investigated beta detector in the upcoming experimental setup, the FWHM of single-cell images generated by the chip was analyzed. While a cell possesses a distinct volume and cannot be considered a true point source, investigating the device's response to the type of source it will interact with during in-vitro experiments yields practical insights into its performance. The conducted analysis first examines the scenario of traditional cell cultures, followed by the three-dimensional cell culture scenario.

5.2.1.1 Two-dimensional cell culture scenario

In the scenario of two-dimensional cell culture, the modeling of the setup is the same as described in the previous sections. The single cell considered for studying the resolution is located within a thin layer of culture medium, contained inside a petri dish. By evaluating a deposition of ^{111}Ag within the entire cell volume, the images of single cells were analyzed to examine the corresponding PSF.

When examining an image, a more convenient approach to characterize the PSF and its properties involves investigating the projections of the two-dimensional distribution along the two spatial axes. Analyzing the profiles of the image enables the extraction of relevant PSF information and enhances the visualization of the resulting distribution. For each of the acquired images, the profiles of the central peak along both axes (x and y) have been examined. The procedure for extracting the projected distributions of these images follows a similar method as discussed in Section 4.4.3. The profiles are derived by projecting the two-dimensional image along one of the axes. A range of values encompassing the single-cell image is selected along the axis of interest, and the resulting two-dimensional histogram is projected along the other axis.

To enhance the statistics of the analyzed projections, rather than focusing on a single position along the projection axis, integration is performed across a narrow range to increase the counts considered. When studying a projection along the y axis, the procedure involves first integrating the 2D histogram along the y axis and then performing the projection operation along the y axis. This method is visually summarized in Figure 5.9, explaining the approach used to extract profiles of the examined peaks from all the subsequent images. The chosen ranges for obtaining projections along the two axes are depicted in the figure.

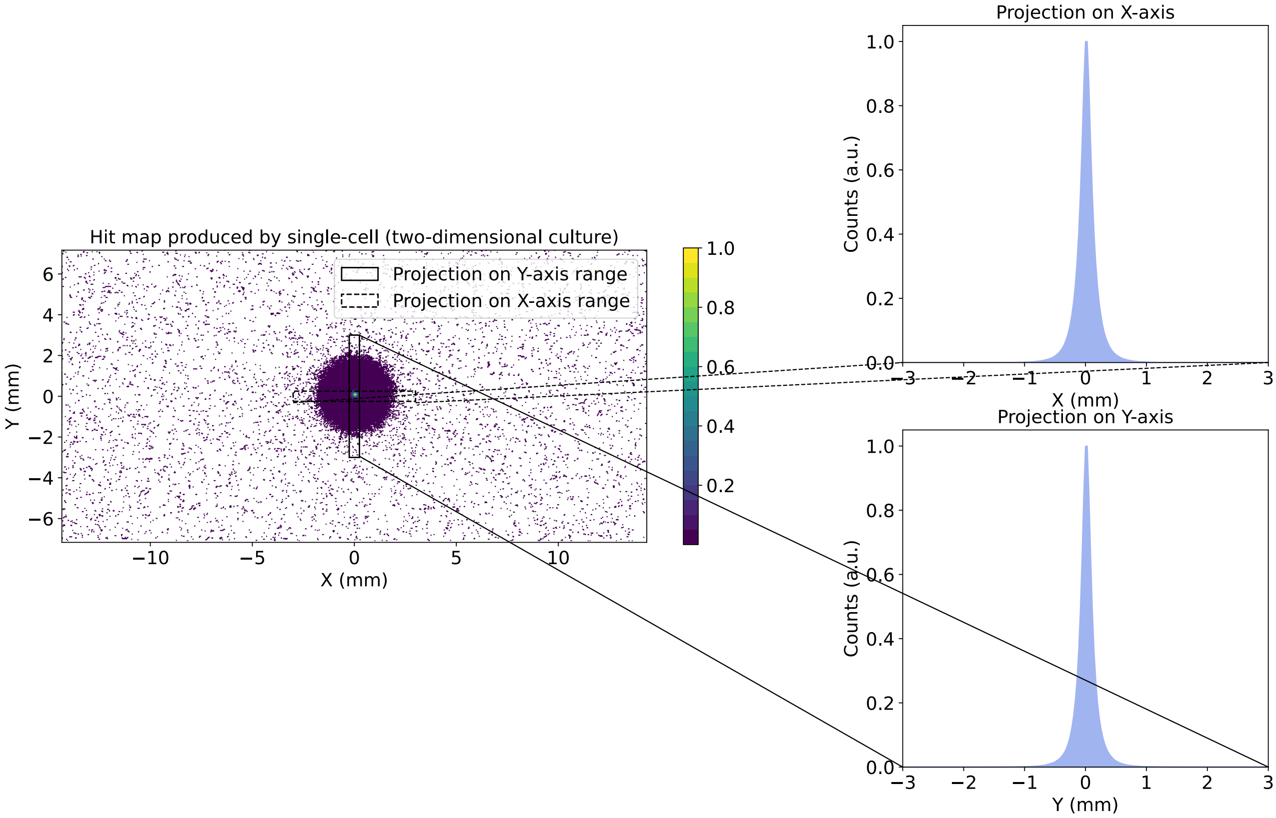

Figure 5.9: Image of a single cell in two-dimensional cell culture and projections of the image along the two axes, x and y. The ranges of projection evaluated to obtain the two profiles on the right are depicted within the two-dimensional histogram.

The provided description seeks to summarize the calculation procedure employed to assess the examined projections carried out to characterize the distribution of individual cells. This approach simplifies the analysis of data distribution along both spatial axes, potentially facilitating the detection of any underlying asymmetries.

This projection methodology is uniformly applied to all subsequent analyses concerning the exploration of image profiles obtained via the ALPIDE detector.

To evaluate the single-cell resolution within the two-dimensional culture scenario, profiles of interest along the x and y axes were extracted. For each one-dimensional distribution, the calculation of its FWHM is calculated. This parameter is estimated by considering the number of bins with heights exceeding half of the maximum height. Figure 5.10 presents the derived profiles and highlights the height where the FWHM condition is met, precisely when $f = f_{\max}/2$.

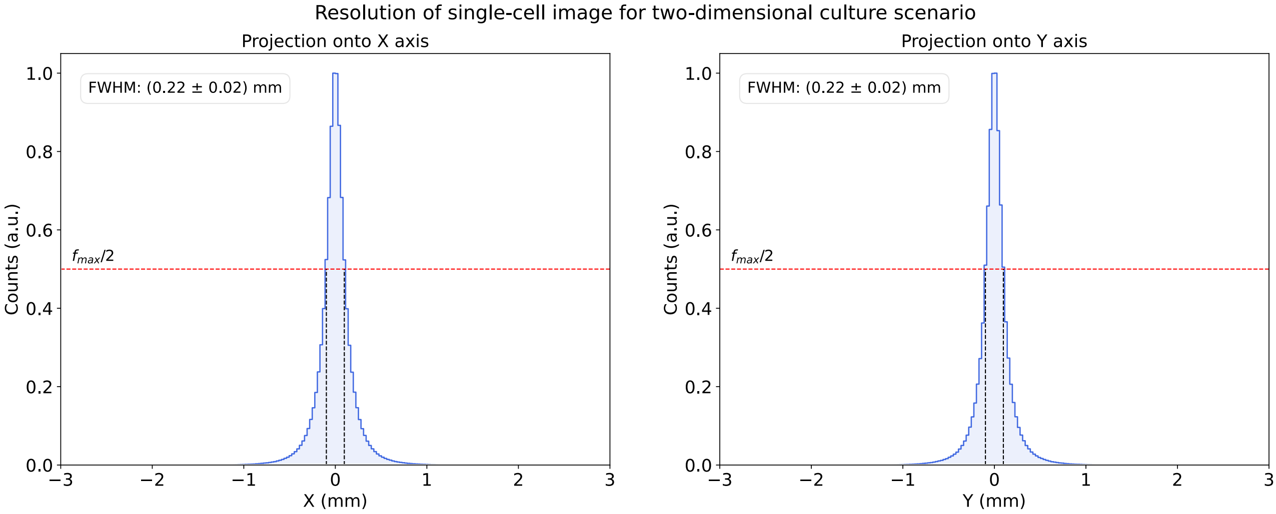

Figure 5.10: Projections of the single-cell image onto the x and y axes respectively for a two-dimensional cell culture scenario. The ^{111}Ag radioisotope is contained in a single cell placed at the center of the cell culture medium. In each plot, the height corresponding to half of the maximum of the histogram is indicated, and the associated FWHM is reported.

Being a spherical source, the profiles projected along the two axes are identical, except for some differences at the level of individual bins due to statistical fluctuations. In both cases, it can be observed that the FWHM associated with the projections is 0.22 ± 0.02 mm, the same for both functions. The error on the parameter was estimated by taking the maximum error as twice the amplitude of a bin (equal to 28 μm, the size of the ALPIDE pixel) and assuming a uniform distribution. When characterizing the FWHM, the amplitudes of the bins with counts equal to or greater than half of the maximum height are added together. Since the curves obtained are subject to fluctuations due to the stochastic nature of the examined simulations, the estimation of FWHM may be influenced by these variations and include a bin or not on one of the two sides of the curve. These considerations led to selecting the described maximum error. The choice of the uniform distribution represents a conservative approximation, aiming to ensure that all effects related to the randomness of the simulations under study are fully encompassed.

In conclusion, the resolution estimation via FWHM indicates that the instrument can provide a resolution of 0.22 ± 0.02 mm for a single-cell source. Given that the chosen radius for modeling cells within the culture is 10 μm, it becomes evident that the estimated resolution signifies the instrument's inability to resolve an individual cell. However, the detector is capable of resolving micro-regions within the cell culture. Despite lacking the ability to generate images at the individual cell level, the device under investigation offers a satisfactory resolution for identifying even very small areas of internalization of the experimental radiopharmaceutical. It is essential to consider that in a real-world scenario, each cell line features specific dimensions, and cellular volumes can vary individually from one cell to another. Furthermore, the patterns exhibited by cancerous tissue can significantly differ based on the studied tumor line. As such, the resolution provided by the instrument could be possibly suitable for visualizing emitting cells at an individual level or can offer sufficient resolution to resolve clusters of tumor cells.

5.2.1.2 Three-dimensional cell culture scenario

A similar analysis to the one conducted for traditional cell culture has also been carried out for hydrogel-based cell culture. To determine the FWHM resolution of the PSF produced by a single source cell, the type of culture under examination must be taken into account. As mentioned before, in the case of three-dimensional cultures, cells can be positioned at different depths in the hydrogel volume and consequently at different distances from the detector. The source-detector distance significantly influences the produced image and modifies the resolution that the instrument can provide for the single cell. To fully understand the detector's response to the different positions that the cell can assume, it was decided to compare the resolution obtained for a range of different distances between the source and ALPIDE. The hydrogel-based culture was modeled as described earlier, and for each potential depth in the hydrogel volume, a simulation was conducted in which ^{111}Ag was deposited inside the cell volume. For each of the examined distances, projections along the x and y axes were analyzed to study the FWHM as the cell's position varied. All the obtained profiles are shown in Figure 5.11, along with the corresponding FWHM estimates.

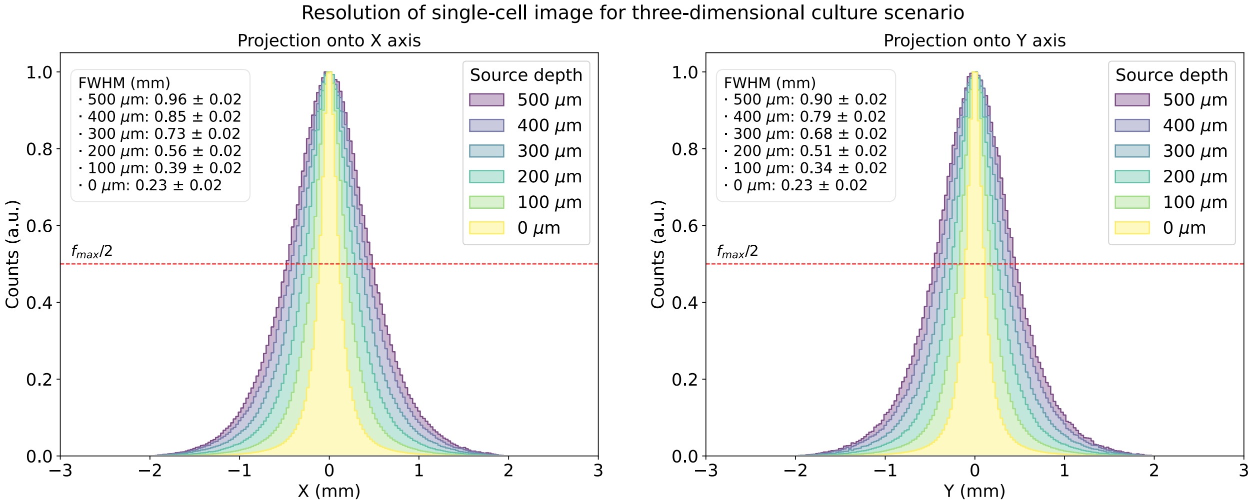

Figure 5.11: Projections of the single-cell image onto the x and y axes respectively for a three-dimensional cell culture scenario. The ^{111}Ag radioisotope is contained in a single cell placed at different depths inside the culture hydrogel volume. In each plot, the height corresponding to half of the maximum of the histogram is indicated, and the associated FWHM is reported.

The first consideration that can be made regarding the obtained curves is a comparison between the two profiles, particularly between the derived FWHM values. As observed, the parameters obtained for the projections along the two axes do not match at certain depths of the source position. This difference is explained by the statistical fluctuations present in the performed simulations and is completely included in the estimated error, confirming the assumption made in the selection of the error itself.

An additional consideration can be made to observe how the increase in distance between the source and the detector impacts resolution. The worsening effect on resolution becomes evident as the cell moves away, both when observing the data distributions and their corresponding FWHM. Even small distances significantly influence the performance the instrument can provide. In particular, when comparing the estimated resolution in terms of FWHM between the most optimistic and the most pessimistic conditions (minimum and maximum distance, respectively), it is observed that the resolution quadruples.

The information extracted from the single-cell image profiles enables a quantitative investigation into how the position of the emitting cell within the hydrogel impacts the resolution. By simulating various scenarios and deducing the FWHM of all generated profiles in each case, it becomes possible to examine the behavior of the FWHM parameter concerning the cell's distance from the detector. The obtained data points provide a visualization of the resolution increase and infer the trend followed by the data. The relationship between the calculated resolution for each profile and the cell's depth within the hydrogel is depicted in Figure 5.12.

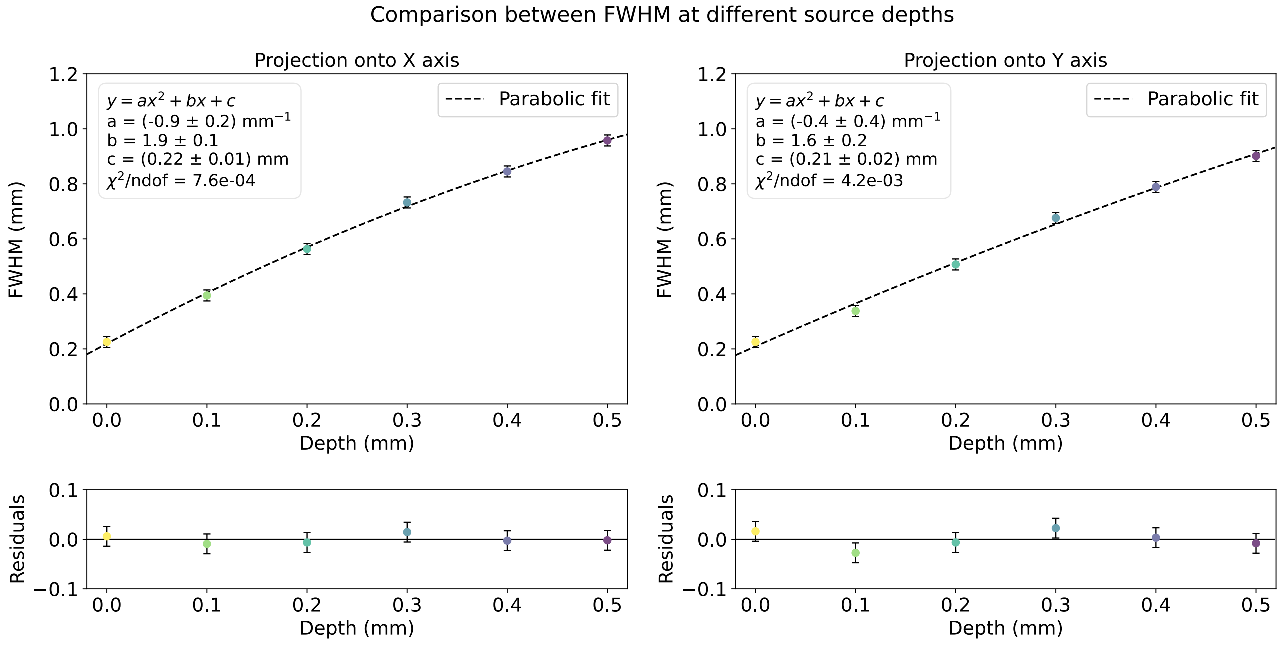

Figure 5.12: FWHM characterizing the examined projections (along x and y axes) as a function of the depth of the emitting cell's position within the hydrogel volume, simulating the environment of a three-dimensional cell culture. The points are fitted with a parabolic function.

Observing the distribution of the obtained data points, it was hypothesized that a good model to describe the trend they follow is represented by a parabolic function ($y = ax^2 + bx + c$). This function was interpolated to the data points to test its ability to predict the variation of resolution as a function of the distance from the detector. The proposed parameterization can interpolate the data, allowing for a good estimation of the FWHM that would be obtained for cell depths not simulated. The computed fit parameters and the associated χ^2 are directly included in the presented plots. It can be observed that the chi-square test confirms a good agreement with the hypothesis of a quadratic trend. However, it is important to note that the error associated with the calculated points was selected with a cautious approach, possibly overestimated. This choice influences the results of the χ^2 test, even though the fit seems to adhere well to the analyzed data, with parameters subject to a moderate error. It should be noted that the interpolated curve can provide a prediction of the FWHM for depths greater or intermediate to those selected; however, it would fail to estimate resolutions at smaller distances. In that case, one should consider a difference in the protective film used between the hydrogel and the beta detector, thus modifying the thicknesses and materials that the particles pass through before being detected.

In conclusion, the analysis of images produced in a three-dimensional cell culture setup allowed the estimation of the instrument's resolution, following a similar approach to that employed in the two-dimensional scenario. Resolution is determined by calculating the FWHM of the image projections along both axes. This parameter is significantly influenced by the depth of the cell's position within the hydrogel, leading to a rapid degradation in resolution as the cell's distance from the detector increases. While at zero depth the resolution corresponds to that of the traditional culture scenario, the resolution's increase follows a quadratic trend with distance, eventually quadrupling at the maximum distance. In this context, the instrument's capacity to distinguish between distinct regions is limited to larger portions within the hydrogel. Consequently, precise identification of the tiny volumes where the radiopharmaceutical is deposited becomes more challenging, though characterization of emission areas remains feasible.

5.2.2 Detector resolution analysis: Rayleigh criterion

In addition to the discussed straightforward approach to deduce the resolution of the analyzed instrument, the response of the ALPIDE detector in the presence of a pair of emitting cells was investigated to understand the point at which a pair of cells can be distinguished and resolved. To assess the device's resolving power in the case of two distinguishable point sources, the Rayleigh criterion (previously introduced in Section 2.3.2) was evaluated. The application of this criterion involves studying the profiles produced in the two-dimensional images by a pair of point sources placed at a known distance. Specifically, the single cell represents the reference point source for which the associated PSF is studied. In this analysis, different distances between pairs of emitting cells were considered to determine the point at which the Rayleigh resolution limit is reached, thus deducing the estimated resolution.

5.2.2.1 Two-dimensional cell culture scenario

The verification analysis of the Rayleigh criterion was first carried out for the traditional cell culture scenario. To simulate this setup, the GEANT4 model described earlier was reproduced. However, in this case, two cells were placed instead of a single one. The positions of the two cells are centrally located within the volume of the culture medium along the y and z directions, while their position along the x axis is varied to test at what distance the two cells can be considered resolved according to the Rayleigh limit. An example of a two-cell image obtained with this setup is presented in the Appendix (Figure 6.3).

From each of the 2D images produced at different distances, the profiles of the resulting curves were studied by projecting the images along the y axis following the procedure described earlier. In this case, it was not of interest to analyze the peak sections along the y axis since only the projection on the x axis includes the necessary information. A comparison of all the profiles associated with the performed simulations is presented in Figure 5.13.

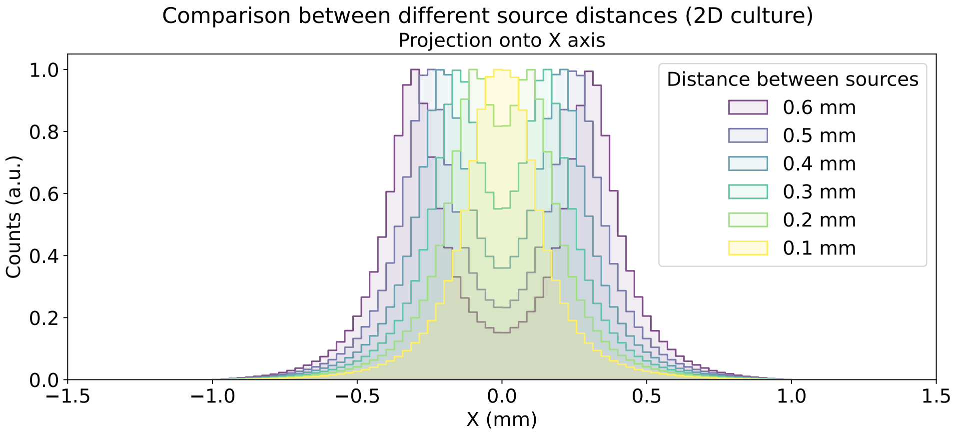

Figure 5.13: Projections onto the x axis of the two-cell image obtained in a two-dimensional cell culture with two cells positioned at a variable distance along the x axis.

The resulting function from the projection process is the sum of the Point Spread Functions (PSF) of the two individual sources. These individual distributions can be approximated by fitting the total histogram. Considering a function that is the sum of two identical trends allows obtaining a model for the behavior of the individual PSFs. For the type of system under examination, a Gaussian approximation was chosen for the produced PSFs, as it provided a better description of the data under investigation compared to other options evaluated (such as Lorentz and Voigt distributions). Although a Gaussian trend is expected when analyzing a point source, the curves do not perfectly adhere to the normal distribution. The deviation from a Gaussian behavior can be attributed to different reasons. The main factor behind the deviation from a Gaussian behavior is related to the behavior of beta radiation inside matter, which is characterized by a high probability of scattering and deflecting its trajectory when interacting with a medium such as silicon. The scattering processes that electrons undergo with the materials they traverse alter the produced image, leading to a broader profile that exhibits a combination of Gaussian and non-Gaussian components. Furthermore, it is important to remark that the type of source being treated is not an actual point source, but the emission volume occupies a defined space. This modifies the final image and distorts the observed distribution.

Despite these constraints, the Gaussian assumption has offered a reasonably accurate approximation of the projection trends, enabling the effective identification of PSF maxima.

For each of the images obtained by evaluating a set of different distances between the emitting cells, a sum of two Gaussians was fitted. The resulting functions allow approximating the PSFs of the two sources, identifying their peaks, and estimating their slopes. Figure 5.14 shows an application of the sum fit, highlighting the single inferred Gaussian distributions and the identification of the maximum points.

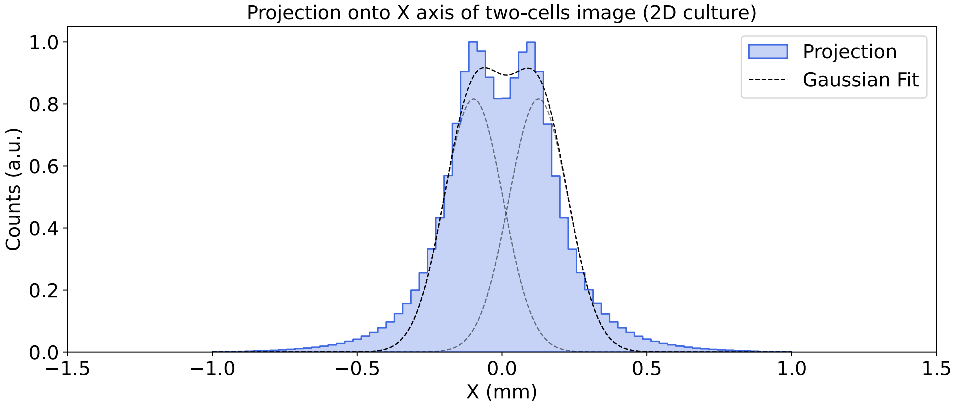

Figure 5.14: Projections onto the x axis of the two-cell image obtained in a two-dimensional cell culture with two cells positioned at the center of the culture medium. The cells are separated along the x axis with a predetermined distance of 0.2 mm. The profile is fitted with a function that is the sum of two Gaussian distributions, each of which is also represented individually.

From the presented plot, it is evident that the Gaussian assumption struggles to describe the tails of the two single-cell curves. The Gaussian model fails to approximate the descending trend of the analyzed PSFs, making the direct application of the Rayleigh criterion (which requires the difference between the maximum of one PSF and the minimum of the other to be zero, $x_{max} - x_{min} = 0$) too uncertain.

To overcome this issue, it was decided to exploit an additional condition that occurs when examining the criterion. When the two sources are at a distance corresponding to the limit of the resolution power, the profile produced in the image satisfies:

$$\frac{I_{\text{mid}}}{I_{\text{max}}} = \frac{8}{\pi^2}.$$

To test when the selected distance between the two cells corresponds to the Rayleigh criterion's limit condition, it is possible to verify if the examined projection meets this requirement. For each of the evaluated distances between the two source cells, the estimation of this ratio was performed. To more easily deduce the most interesting distance values to simulate, a plot was created to study how the ratio $I_{\mathrm{mid}}/I_{\mathrm{max}}$ varies with the source positions. Figure 5.15 shows the points obtained using this approach, including the distance that best satisfies the Rayleigh criterion. The plot includes a parabolic fit applied to the available data points.

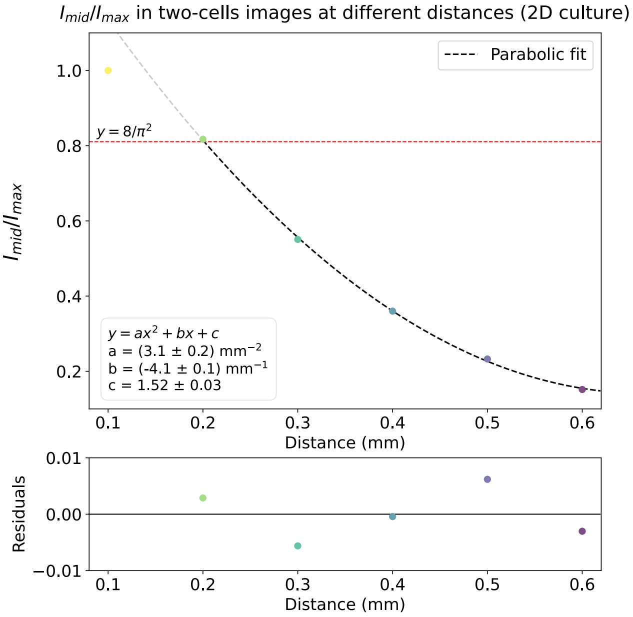

Figure 5.15: $I_{\mathrm{mid}}/I_{\mathrm{max}}$ ratios characterizing the examined two-cell images' profiles (two-dimensional cell culture scenario) as a function of the distance between the two sources. The points are fitted with a parabolic function.

Observing the calculated points, it was observed that the described trend can be accurately approximated by a parabolic function. By applying a fit using a subset of the available data points, it is possible to obtain an analytical curve that provides a reasonable description of the overall behavior. The parabolic hypothesis can characterize effectively approximate the observed data trend. The data point at the minimum distance was removed from the interpolation procedure. As depicted in Figure 5.13, when the two sources are very close, the profile makes it impossible to distinguish the two maxima, as they merge into a single peak. This occurs at distances slightly below the Rayleigh criterion, causing the parabolic hypothesis to lose its applicability for excessively low spreads. Therefore, only data points with a ratio $I_{\mathrm{mid}}/I_{\mathrm{max}}$ lower or close to the Rayleigh condition were considered.
The analyzed points allow the determination of the Rayleigh limit for the studied system. The observed resolution with this approach is approximately 0.2 mm (equivalent to 0.21 mm when the obtained parabolic function reaches $8/\pi^2$). This result is in excellent agreement with the method of FWHM of single-cell image projections explained earlier. Therefore, in the two-dimensional cell culture scenario, it appears possible to conclude that the resolution that a detector based on the utilization of the ALPIDE chips can provide is around 0.2 mm. This resolution allows distinguishing regions with small dimensions where the prototype radiopharmaceutical is deposited, although it does not provide resolution at the individual cell level.

5.2.2.2 Three-dimensional cell culture scenario

An analysis of resolution was also carried out for three-dimensional cell culture to investigate how the under-construction beta detector responds to multiple cell sources inside a hydrogel matrix. The setup was modeled in GEANT4, as described in previous sections. Two cell sources were introduced into the hydrogel medium, and their separation distance was systematically modified to establish the boundary condition. Given the three-dimensional nature of the hydrogel-based culture, the source's mobility was not confined solely to the plane parallel to the detector's surface but was also investigated along the orthogonal axis. This entailed evaluating the instrument's resolution in various scenarios characterized by different positions along the z axis for the cells (0 and 500 μm depth). In each of these scenarios, the point at which the Rayleigh criterion is met was determined, accounting for cases where the cells were in proximity to both the lower and upper boundaries of the hydrogel volume. Two examples of the images generated in the hydrogel-based culture scenario are provided in Appendix, shown in Figures 6.4 and 6.5.

From each of the produced images, profiles along the x axis relevant to the analysis were extracted. The distributions obtained from the projection process along the y axis allowed the application of the Rayleigh criterion to identify the minimum distance still associated with a resolved image. The derived profiles for each investigated distance are summarized in Figure 5.16(a) for cells adhering to the lower wall of the hydrogel and in Figure 5.16(b) for cells positioned at the maximum distance.

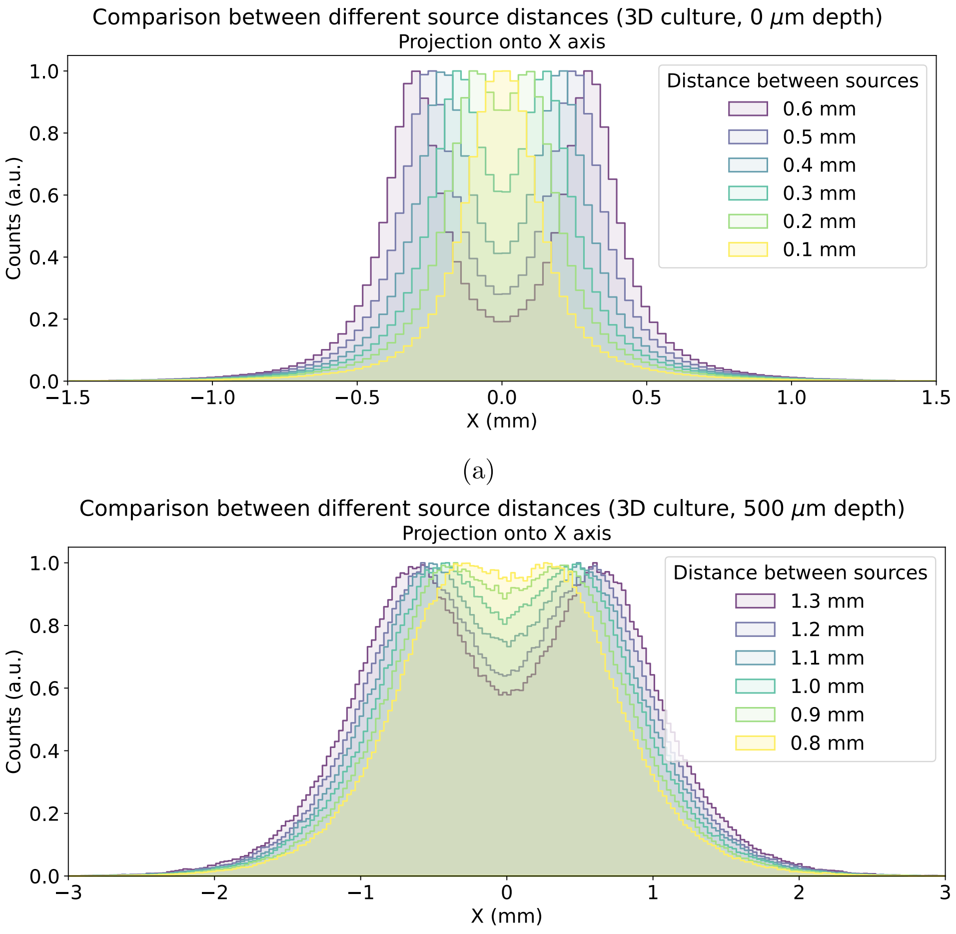

(a)

(b)

Figure 5.16: Projections onto the x axis of the two-cell image obtained in a two-dimensional cell culture with two cells positioned at a variable distance along the x axis. Along the z axis, the cells are located in contact with the (a) lower and (b) upper surface of a three-dimensional cell culture.

Also in the three-dimensional culture scenario, a preliminary attempt for the direct application of the Rayleigh criterion through a Gaussian fit procedure was attempted. The Gaussian assumption was however unable to capture the tails of the PSF distributions, making it impossible to verify the Rayleigh criterion in terms of locating maxima and minima. An example of the performed fits is shown in Appendix, Figure 6.6 and 6.7, where the limitations of the assumed hypothesis can be observed.

To determine the condition where the Rayleigh limit was satisfied, the same approach described for the 2D cell culture scenario was used. When the selected distance represents the limit of the resolution power, the ratio $I_{\mathrm{mid}}/I_{\mathrm{max}}$ assumes a known value. By studying the trend of how this ratio varies with the distance inserted between the cells in the simulations, it is possible to deduce the resolution estimate for both positions along z. Figure 5.17 shows how the $I_{\mathrm{mid}}/I_{\mathrm{max}}$ ratio varies as a function of the distance parameter between the cells, for both zero depth and 500 μm depth.

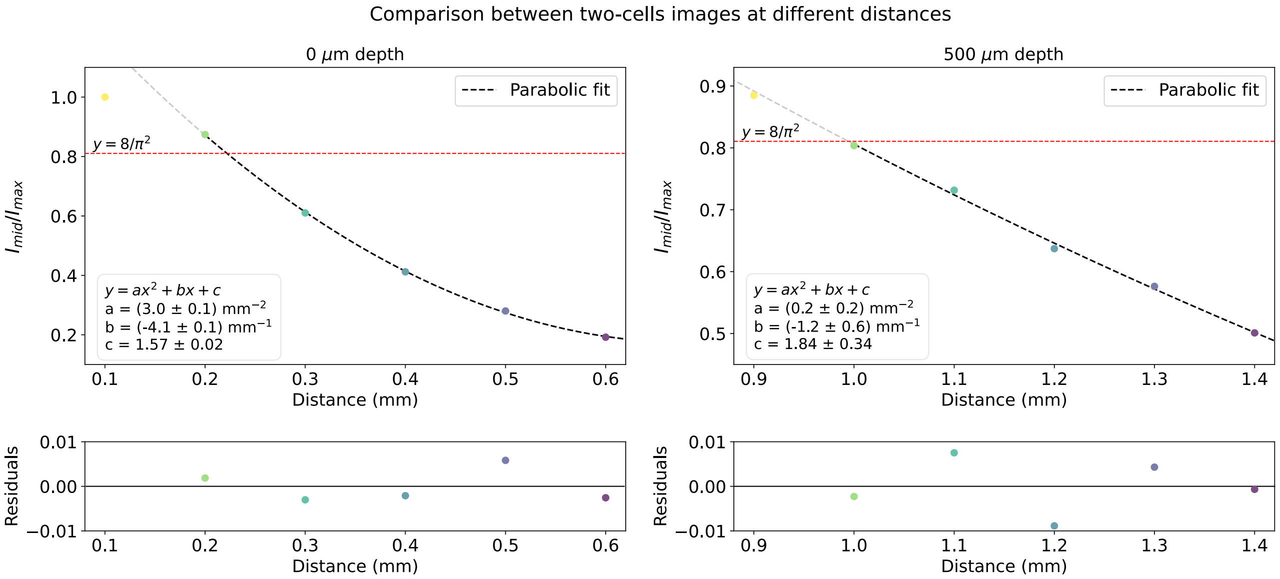

Figure 5.17: $I_{\mathrm{mid}}/I_{\mathrm{max}}$ ratios characterizing the examined two-cell images' profiles (three-dimensional cell culture scenario) as a function of the distance between the two sources. The points are fitted with a parabolic function.

As before, a parabolic fit was applied to the available data points to obtain an approximation of the studied curves, even for those distances that were not simulated. This assumption was again verified by excluding data points with values of the ratio $I_{\mathrm{mid}}/I_{\mathrm{max}}$ significantly greater than the reference value of $8/\pi^2$. It can be observed that in the case of maximum depth of the two cells within the hydrogel, the behavior appears to be more linear than parabolic, an observation also confirmed by the parameter a approaching zero.

The ratios $I_{\mathrm{mid}}/I_{\mathrm{max}}$ as a function of the distance between the source cells also allow verifying when the Rayleigh limit is reached. In the case of a cell positioned at the minimum possible distance from the lower surface of the hydrogel volume, the calculated resolution is 0.22 mm (computed when the fitted function reached $8/\pi^2$), which is consistent with the estimate obtained using the FWHM of the single-cell profiles. Additionally, it is noteworthy that this resolution is very close to the value determined in the case of two-dimensional cell culture.

Regarding the setup with cells positioned at the maximum distance from the detector surface, the resolution inferred using the Rayleigh criterion is 1 mm, significantly higher than the null depth case. A spacing of only 500 μm from the minimum considerate distance results in significant degradation of the resolution, increasing by a factor >4. This prediction aligns with the estimate obtained using the previous approach and confirms that moving a source cell away from the beta detector can heavily impact its performance, allowing for precise determination only of areas within the 3D cell culture with larger and more extended radio-pharmaceutical deposition surfaces.

In conclusion, a brief summary of the deduced results can be provided. To compute the resolution of the ALPIDE chip in different potential scenarios (traditional cell culture and hydrogel-based), the produced PSF of the device was characterized by studying its width and applying the Rayleigh criterion. Both applied approaches estimate the resolution of the instrument in a two-dimensional culture scenario to be approximately 0.2 mm, with slight fluctuations reaching values slightly higher by a few tens of microns. In the case of three-dimensional culture, the impact of the distance between the emitting cell and the detector on the resolution has been quantified. Utilizing both described techniques, it was determined that for a cell adhering to the lower surface of the culture, the resolution becomes 0.22 mm, while for a cell at the maximum distance from the detector, the resolution is around 0.95 mm (almost 5 times the previous value).

5.3 Protective material comparison

When analyzing the setup for future in-vitro tests, it is important to consider that hydrogel-based cell cultures will require the introduction of a protective layer between the gelatinous material and the upper surface of the device. This layer prevents possible contaminations and can serve several functions that facilitate the acquisition. However, the inclusion of a protective film introduces a thickness between the emitting cell and the chip, which worsens the image resolution. As the source moves away, the detector's surface covers a wider cross-sectional area of the emission volume, resulting in a larger image associated with the same cellular volume. To understand how the introduction of a film in the analyzed setup affects the resolution of the produced images and which materials may be more suitable for the application under study, various scenarios were compared in the conducted simulation. These considerations pertain to the three-dimensional culture scenario, where the inclusion of a protective film between the culture and the detector surface becomes fundamental. This supplementary layer serves the primary purpose of preventing any possible contamination of the detector surface, ensuring that no radioactive material adheres to the chip. Due to the semi-solid nature of hydrogel, there exists a potential risk of leaving unwanted radioactive residue on the detector surface during experiments involving radioactive samples. The protective film acts as a barrier that can be conveniently replaced after an acquisition concludes, thereby ensuring the continued absence of such contamination on the beta detector.

In order to minimize the impact on image quality, it was essential to select a protective film with the thinnest possible thickness. Two candidate materials that can answer this request were considered for comparison to determine their effects on the produced cell source image: mylar and polystyrene. Both mylar and polystyrene can produce films extremely thin, down to 50 μm.

Mylar is a polyester film that is widely used in physics laboratories due to its excellent barrier properties, providing resistance to moisture, gases, and chemicals. It is available in an "aluminized" form, which means that the mylar film is coated with a thin layer of aluminum. The aluminum layer serves as a shield against ambient light, preventing visible light photons from reaching the sensitive components of instruments and interfering with measurements. On the other hand, polystyrene is a synthetic polymer commonly used in laboratory settings, including biology laboratories. Compared to mylar, polystyrene is a much more rigid and durable material, although less malleable. It offers good resistance to chemicals and has excellent insulation properties.

In order to test and compare these materials, single-cell images produced by an individual ALPIDE detector have been analyzed. The aim is to understand how the material thickness degrades the image and to compare the effects of the candidate materials, *i.e.* mylar, aluminized mylar, and polystyrene. For each of the obtained images, the shape and profiles of the created peak were studied to investigate how the generated peak is affected by the materials used. In particular, the amplitudes of the projections of the images have been compared to understand how the resolution of the single-cell image is influenced by the introduction of the film material. The projection operation was carried out with the approach described in the previous section (summarized in Figure 5.9).

The analysis was based on a comparison of the three candidate materials (mylar, aluminized mylar, and polystyrene) to provide a basis for the hydrogel-based culture. Each of these materials allows

obtaining very thin layers, up to less than 50 μm in thickness. To analyze a realistic and general scenario, single-cell images were compared by inserting a protective film of 50 μm and 100 μm in each of the materials that could be used. Figure 5.18(a) represents a comparison of the profiles (along the x axis) of the single-cell images produced for a configuration with a cell adhering to the lower surface of the hydrogel volume, considering both a 50 μm and 100 μm thick film, while Figure 5.18(b) shows the equivalent comparison in the case of a cell placed at a 500 μm depth. All the profiles obtained as projections along the y axis are collected in the Appendix.
In this comparative analysis, the histograms were normalized while preserving the proportion of counts observed without normalization. For this purpose, instead of normalizing each individual histogram separately (which would result in each one-dimensional histogram having peak counts equal to 1), all histograms were normalized to the maximum of the histogram with the highest counts in the most populated bin.

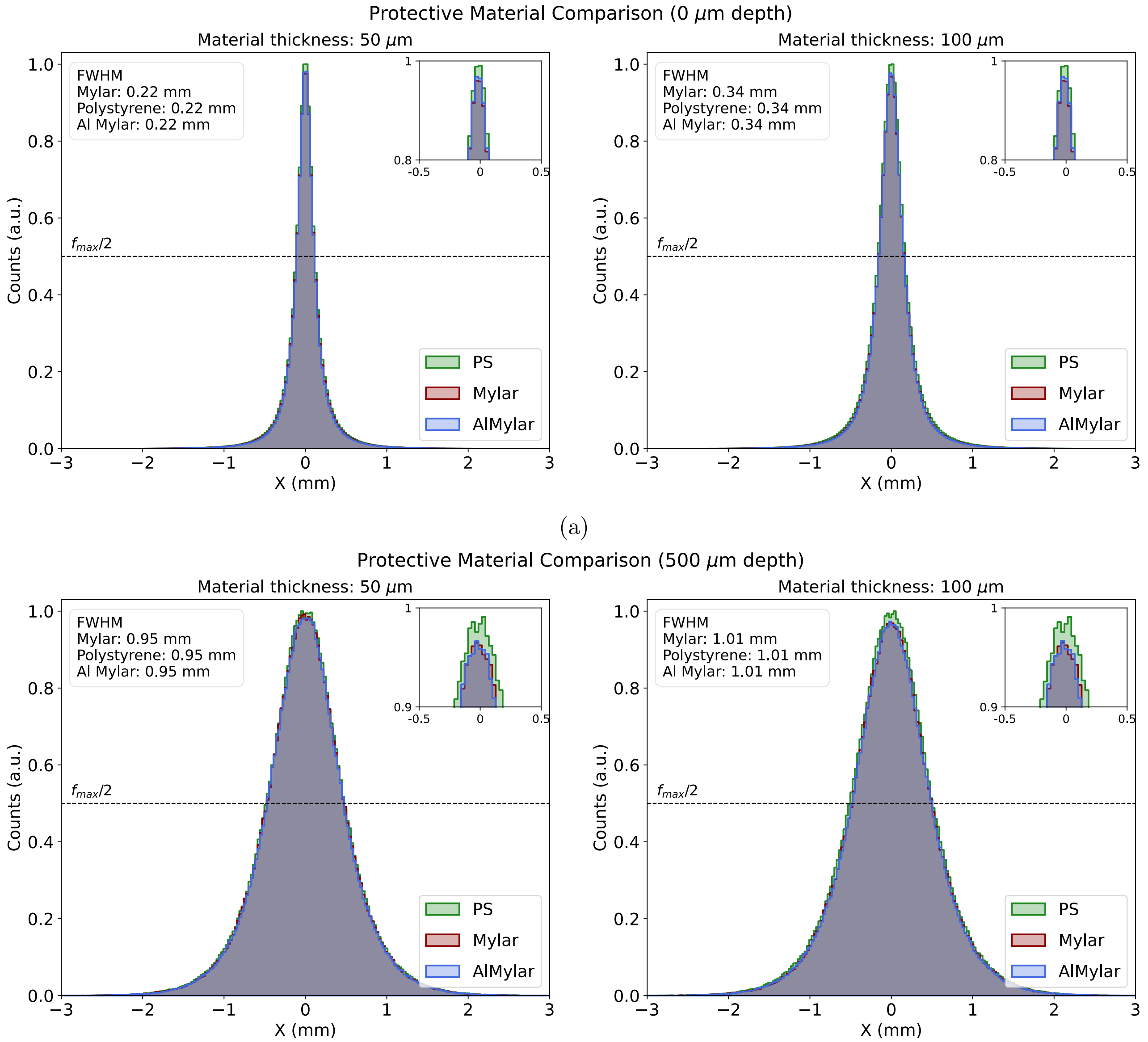

(a)

(b)

Figure 5.18: Comparison of the projections of single-cell images onto the x axis obtained by simulating different candidate materials for the protective layer (mylar, aluminized mylar, and polystyrene). The cell is placed in contact with the (a) lower and (b) upper surface of a three-dimensional cell culture. In each image, the FWHM associated with the obtained peaks is reported.

The presented plots also include quantitative information about the FWHM of the analyzed profiles to compute a quick measure of the resolution that will be provided in the studied scenario.
The first comparison that can be made regarding the possible protective films is between different material thicknesses used. Evaluating a slightly thicker film, around 100 μm, the image shows a greater amplitude, but the magnitude of this variation depends on the position of the examined source. When the cell is placed at the minimum distance from the device, there is a 55% increase in the calculated FWHM, while when it is located at 500 μm depth in the hydrogel matrix, the increase in FWHM is only 6%. This difference is entirely justified by the relative increase in the cell-detector distance upon the incorporation of a protective film with a specific thickness: for a source positioned in contact with the lower surface of the hydrogel, this distance is equivalent to the thickness of the film, whereas when the cell is positioned at a depth of 500 μm, the increase in distance is only 8% of the total when introducing the 100 μm film (from 550 μm to 600 μm). The introduction of a film thickness, therefore, has a greater influence on the alteration of images produced by cells closer to the bottom of the hydrogel. However, as also evident from the examined profiles, this difference is relatively small and secondary compared to the degradation of the image associated with the cell moving away from the detector.
Another important consideration that can be analyzed is a comparison between the different types of materials considered: it can be quickly noted that the three materials are almost similar when observing the profiles of the generated images. To better compare the materials, it might be convenient to evaluate the differences in bin counts for each of the projections, thus better observing how the shape of the profile varies in the case of different materials. To obtain a comparison between all three materials, it was chosen to compute the differences between the profiles obtained for aluminized mylar and the other possible candidates, classic mylar, and polystyrene. This choice allows for a direct comparison between the most interesting material, thanks to its property of shielding from background light, and the other potential candidates. Figure 5.19 shows this comparison in the case of a source positioned at null depth, and Figure 5.20 in the case of a source at the maximum distance from the detector. All the differences refer to the normalized counts computed as before, so each difference between two histograms relates to the previously represented profiles (Figure 5.18(a) and Figure 5.18(b)).

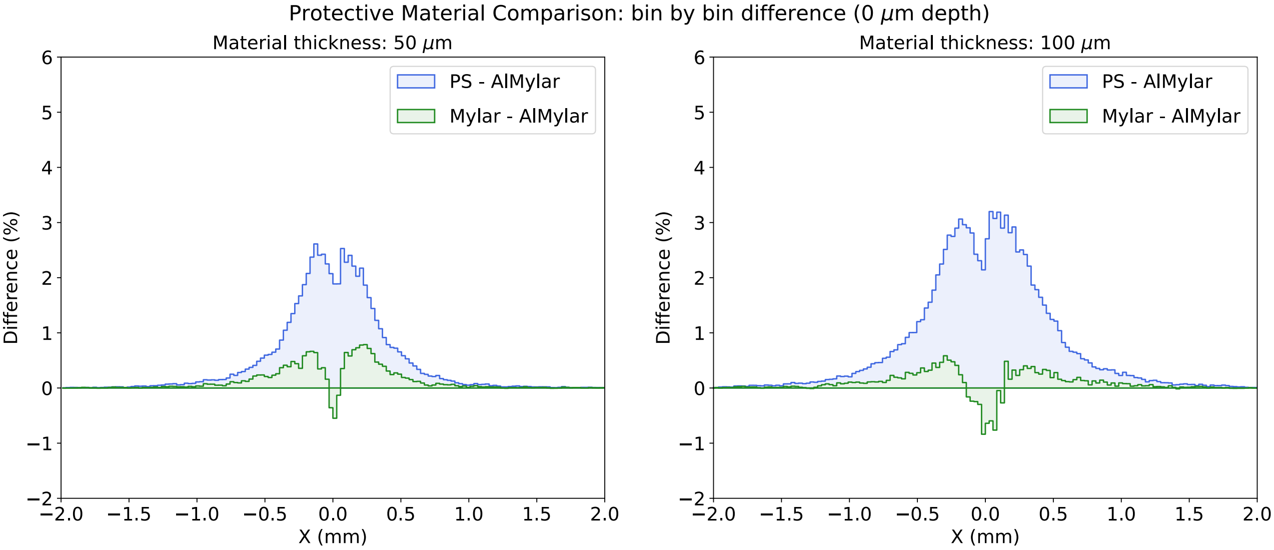

Figure 5.19: Percentage difference between the projections of single-cell images along the x axis between aluminized mylar and mylar, and aluminized mylar and polystyrene as materials for the protective film. The cell is placed in contact with the lower surface of a three-dimensional cell culture.

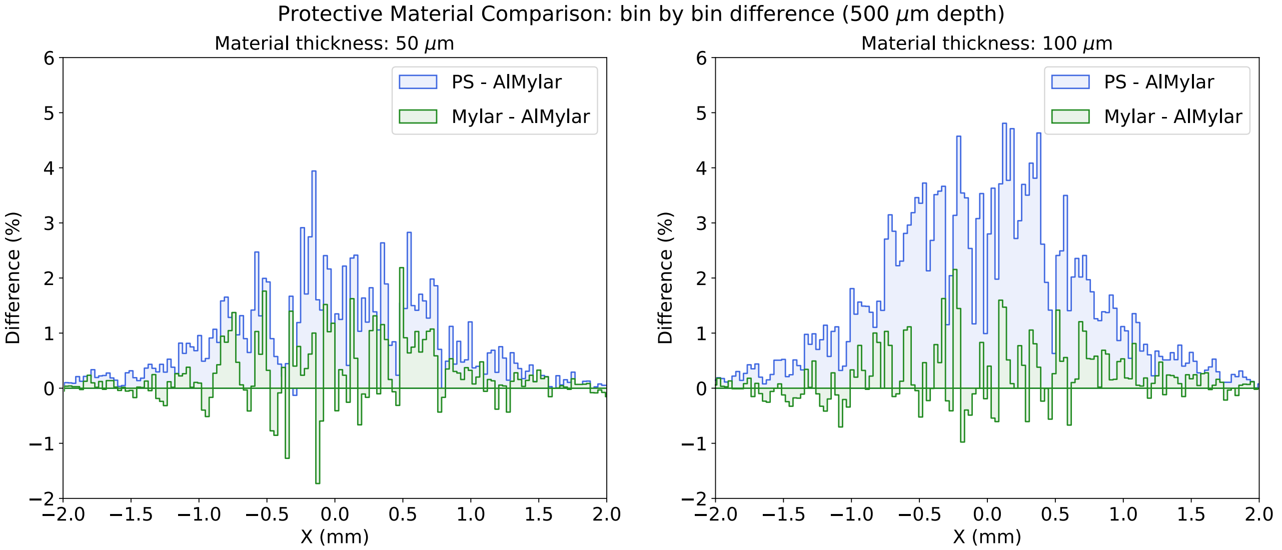

Figure 5.20: Percentage difference between the projections of single-cell images onto the x axis between aluminized mylar and mylar, and aluminized mylar and polystyrene as materials for the protective film. The cell is placed in contact with the upper surface of a three-dimensional cell culture.

When analyzing the two positions of the cell, distinct distributions of the differences between the profiles obtained with various protective materials are present.

In general, it can be observed that the bin-to-bin differences obtained in each material comparison are very low for all the considered configurations, never exceeding a few percentage points.

When the cell is at null depth, the differences in counts between the projections of the images obtained with the various setups are more limited compared to the other possible positioning cases. In this scenario, it can be seen that the difference between mylar and aluminized mylar is smaller than the difference between polystyrene and aluminized mylar. Mylar generally allows for a higher number of counts except at the center of the distribution. Around zero, there is a trend inversion indicating that proportionally, aluminized mylar tends to allow more particles to pass near the emission volume while reducing the number of counts at the periphery. This interesting effect seems partially repeated in the comparison between aluminized mylar and polystyrene. Overall, polystyrene allows for a higher number of counts. However, in this case, throughout the spatial range available, the number of counts obtained with a polystyrene film is higher than the condition with aluminized mylar by a small fraction (a few percentage units when considering the most populated bins).

In the opposite case, where the cell is positioned at the maximum distance, the differences in counts are on average higher. In the comparison between mylar and aluminized mylar, the distribution of differences bin by bin does not seem to follow an exclusive trend but fluctuates significantly. On average, however, it is observed that using regular mylar results in a slightly higher number of registered hits. When analyzing the difference between polystyrene and aluminized mylar, there is a clear tendency for a higher number of hits to pass through when using a polystyrene film, although statistical fluctuations are more significant compared to the case of the cell positioned at zero depth.

In conclusion, aluminized mylar tends to attenuate particles more than other possible materials. However, the observed differences are minimal: when aluminum-coated mylar is compared to the other candidate materials, the total counts decrease by at most 1%, and the bin-to-bin differences in the yielded image remain around limited values (a few percentage points). An interesting effect is observed when studying sources placed at the minimum distance from the detector, where the introduction of aluminized mylar tends to limit the counts along the tails of the single-cell image peak. This behavior could potentially generate sharper peaks, albeit with a slightly lower count, and might be worth exploring further in the future.

In general, aluminized mylar appears to be the most promising candidate, despite its partial attenuation of the produced particles. Besides being a flexible and cost-effective material for protecting the detector's surface, it helps shield potential noise sources related to background light. Considering the advantages it offers and the minimal differences observed compared to other materials, the decision was made to include an aluminized mylar layer as the protective film in the GEANT4 modeling. This choice, which can be modified if future necessities arise, is thus selected for all the developed simulations (and was included also in the previous analyses).

5.4 Impact of acquisition time and activity on image quality

In the upcoming years, the examined beta detector will be employed in in-vitro experiments to assess the capability of the prototype radiopharmaceutical developed by ISOLPHARM to selectively deposit in tumor regions while avoiding healthy tissue. The detector's generated images will serve the purpose of determining the drug's internalization areas within the cell culture. An essential aspect to consider when studying the potential of the instrument under development is to understand the required acquisition time to produce high-quality images, enabling precise localization of emission volumes. Dealing with biological sources, the acquisition time becomes a less flexible parameter as excessively long measurement times could degrade the culture state, leading to contaminations, alterations in metabolism, and cellular death. It is thus of interest to explore the instrument's capacity to generate meaningful images even under reduced acquisition times.

This investigation was carried out for both scenarios of interest for future in-vitro experiments, *i.e.* two-dimensional cell cultures and hydrogel-based cultures. For each of these options, the impact of different acquisition intervals on the visualization of the radiopharmaceutical deposit was studied, starting from the case of traditional cell culture.

5.4.1 Two-dimensional cell culture scenario

The GEANT4 tool does not allow for the direct introduction of the time variable in the developed Monte Carlo simulations, but only the specification of the number of events to be generated. In the considered case, this corresponds to the number of decays of the ^{111}Ag radioisotope and, consequently, to the number of radiopharmaceutical molecules hypothesized to have been internalized by the simulated number of cells. To incorporate the time variable in the analysis, the expected number of decays within a given time interval must be estimated.

The conversion from time to the expected number of decays involves knowing the number of cells present within the culture medium to later deduce the number of ^{111}Ag sources. This information can be calculated as the product of two biological source characteristics: the volume in which tumor cells are deposited and the cell density, which is the number of cells per unit volume in the culture. GEANT4 can directly provide the defined volume for modeling the culture medium or limited volumes where cancer cells are placed. In a heterogeneous culture containing both healthy and tumor cells, the tumor cells can exhibit different behaviors, such as aggregating in confined colonies or diffusing within the volume of normal tissue. The prediction of their behavior is closely linked to the chosen tumor cell line. The various patterns that tumor cells can exhibit can influence the fraction of volume occupied by the diseased tissue. To conduct the proposed analysis, it was chosen to assume that the volume of cancer occupies one-hundredth of the total volume available for cells, regardless of the behavior of a specific tumor line. This choice can be adjusted in the future to achieve accurate predictions for the specific setup used. The cell density is a variable parameter that can be established at the start of the culture. For two-dimensional cultures, a standard value during the stationary phase can be around 10^7 cells/mL [119], [120]. This value is chosen as the reference density during the analysis, and it can be modified based on future needs.

By utilizing the targeting agent included in its molecules, the radiopharmaceutical selectively binds to tumor cells by exploiting receptors exclusively present in the tumor target and absent in healthy tissue. The prototype radiopharmaceutical developed by ISOLPHARM to date utilizes the cholecystokinin-2 receptor (CCK-2R), a G-protein-coupled receptor that is overexpressed in several human cancers but exhibits limited expression in normal tissues [121]. When selecting the receptor to be targeted, an important parameter to consider is the number of receptors present in the cancerous cell, which represents the maximum number of drug molecules that can be internalized. Determining the exact number is complex as it can vary from cell to cell, even based on the tumor cell line used. For the CCK-2R receptor, a reliable range to consider is $[10^5, 10^6]$. Once this range is determined, it is possible to deduce how many radiopharmaceutical molecules, and consequently, silver radioisotopes, can bind to a single cell. This information allows for the calculation of the number of silver radioisotopes present in the culture at the initial time point, from which the number of decays observed within a fixed time interval can be inferred.
To determine the total number of decays observed after a certain time interval, it is simply possible to use the radioactive decay law. The exponential decay described by this law predicts the number of remaining parent isotopes over time. The number of decays can be easily inferred by calculating the difference between the initial number of nuclei and the final number of nuclei, according to the formula:

$$N_{decays} = N_0 \left(1 - \exp\left[-\frac{t}{\tau}\right]\right),$$

Where N_0 is the initial number of nuclei and τ is the mean-lifetime of the ^{111}Ag, equal to 7.423(13) days [22]. N_0 can be derived from all the previous considerations and computations as follows:

$$N_0 = N_{\text{cells}} \times N_{\text{internalization}},$$

which represents the product of the number of tumor cells present in the culture and the number of molecules of radiopharmaceutical deposited on the cell. $N_{\text{internalization}}$ is a parameter that is modified and aims to represent not only the variable number of CCK-2R receptors that a cancer cell expresses but also the possibility that the radiofarmaceutical binds only to a fraction of the available receptors. The temporal trend of the total number of decays occurring within a fixed time interval and the average number of decays associated with a single cancerous cell ($N_{\text{decays}}/N_{\text{cells}}$) for different values of $N_{\text{internalization}}$ are depicted in Figure 5.21.

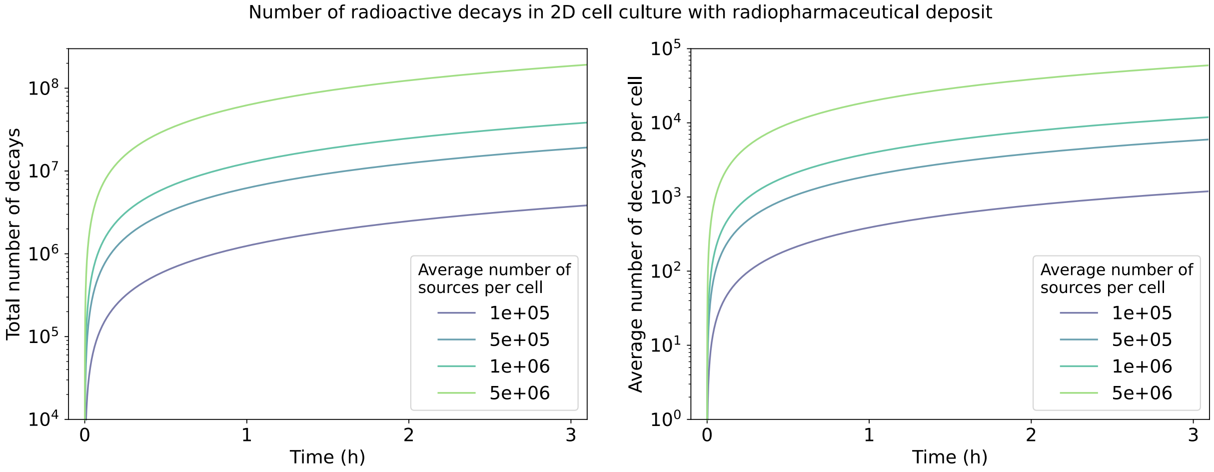

Figure 5.21: Total number of radioactive decays observed and average decays per single cell as a function of time. The cancerous cell is assumed to be collocated in a two-dimensional heterogeneous cell culture. The number of receptors per cell occupied by a radiofarmaceutical molecule is varied.

The second plot provides insight into the order of magnitude of the number of events that can be expected to be observed in a single cell within a given time interval. The information regarding the number of decays associated with each cell helps to understand the type of single-cell images that can be obtained after a certain time interval. Therefore, single-cell images were analyzed by simulating a fixed number of events based on the data obtained from the distributions of the average number of decays. As evident, the average number of decays per cell observed within a specific time interval significantly depends on the number of drug molecules internalized by the cell. However, by examining these average values, it can be inferred that a total of around 10^3 events are rapidly reached after a few minutes, and this count can further increase to approximately 10^4 decays after a few tens of minutes. Consequently, several Monte Carlo simulations were conducted with a setup similar to the ones described, considering a range of decay numbers per cell from 10^3 to 10^5. All the resulting two-dimensional histograms from these simulations are displayed in Figure 5.22.

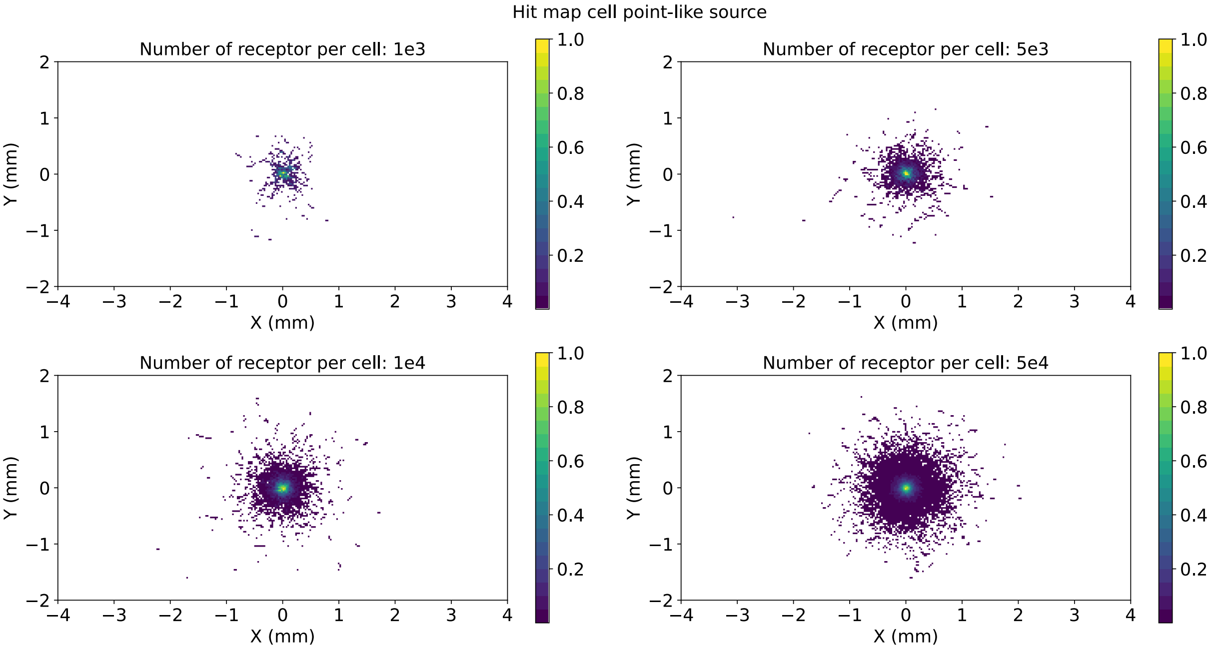

Figure 5.22: Single-cell images obtained by simulating a variable number of events, *i.e.* a variable number of ^{111}Ag decays occurring within the cell. The images illustrate the effect of different decay counts on the visualization of the radiopharmaceutical distribution within the cell.

Although 10^3 events might be a too small number for obtaining a satisfactory visualization of the single source cell, a number of events equal to 5×10^3 already provides an excellent graphical representation that allows identifying the emission center's position. The images appear noisier compared to the previous ones, which were simulated with a larger number of events to ensure better statistics, but they still allow a good identification of the source object.

An interesting parameter to assess how easy is to visually identify the emitting cell volume compared to its background is the contrast between regions with higher counts and those with lower intensity. As explained in Section 2.3.3, contrast is a variable that measures how distinguishable the foreground object (in this case, regions with higher counts) is from its background, represented by all bins with a low number of hits. It can be simply calculated by comparing the intensity of the object in the foreground to the intensity of the background. Contrast measures how distinctly the region of interest in the image can be distinguished from the rest. It also ensures that the number of counts in bins close to the position of the emitting cell is significantly larger than in the outer bins, indicating sufficient statistics for an accurate determination of the peak's location.

The contrast can thus provide an interesting and straightforward parameter for assessing the quality of the produced image. It is therefore feasible to investigate how the contrast evolves when simulating an increasing number of events. This progression has been examined by monitoring the contrast's variation in relation to the total number of decays observed within the individual cell. In this evaluation, additional simulations were included with a variable number of generated events to better understand the trend followed by the points of interest.

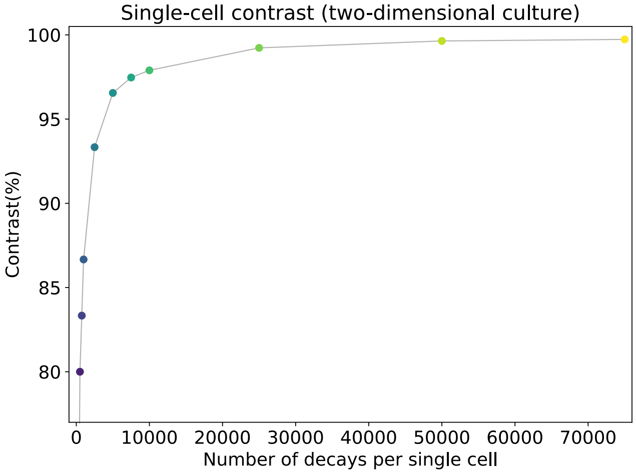

Figure 5.23: Contrast characterizing the examined single-cell images (two-dimensional cell culture scenario) as a function of the number of events generated, corresponding to the number of ^{111}Ag decays inside the cell volume.

As expected, the trend of the available data points describes a monotonically increasing function. As the number of radiopharmaceutical molecules internalized by the cell increases, the contrast exhibited by the single-cell image also increases. For the maximum values of generated decay numbers, it is observed that this parameter tends to approach asymptotically around the maximum value (100%).
By analyzing the trend described by the available data points, it can be inferred that the contrast, for a number of decays per cell of the order of 10^3, never falls below 80%. This finding is interesting because it indicates that even with shorter acquisition times, the image allows a sufficiently satisfactory visualization of the emission center, facilitating the identification of the cell positions at a glance.
In a realistic scenario, it is important to find a balance between image quality and the required measurement times to produce it. As a result, to study suitable acquisition times for the proposed objective, it is necessary to aim for reducing these measurement durations to the minimum required to achieve sufficient image quality, in this case defined as 80% contrast (but potentially variable). Figure 5.22 shows that this condition is met for a minimum of 10^3 radioactive molecules deposited within a single cell volume.
To conclude the conducted analysis, it is necessary to understand the time intervals required to achieve the desired quality in the case of a two-dimensional culture scenario. As a first step to assess this information, it was chosen to test how much time is needed for a single tumor cell, on which a variable number of radiofarmaceutical molecules have been deposited, to obtain a total of 10^3 decays. The acquisition times can be extrapolated from the curves in Figure 5.21. Figure 5.24 graphically illustrates when the number of decays per cell reaches the set value for the single cell case.

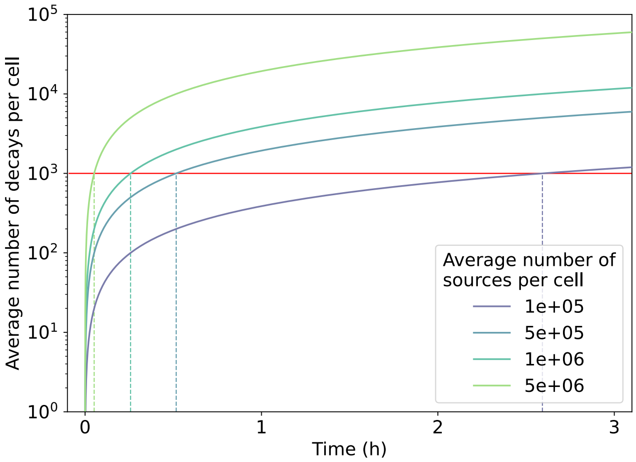

Figure 5.24: Average number of radioactive decays per single cell as a function of time. The cancerous cell is assumed to be collocated in a two-dimensional heterogeneous cell culture. The number of receptors per cell occupied by a radiofarmaceutical molecule is varied. The red line highlights where the decay counts are equal to 10^3, the quantity required for producing an image with sufficient contrast.

The single-cell information allows the estimation of the times required to obtain images of sufficient quality even in a more realistic scenario of two-dimensional cell culture. The condition of a single diseased cell dispersed within normal tissue is a possible but unlikely situation. In a heterogeneous culture, the growth dynamics of healthy and cancer cells can follow various behaviors based on the chosen tumor cell line [122], [123]. Therefore, the cancer cells can exhibit a wide variety of patterns within the culture. In most cases, these cells aggregate into a single compact volume within the culture or into several smaller clusters. Since diseased cells tend to gather in confined areas, it is useful to investigate how the visualization of cell clusters depends on the temporal variable rather than focusing on a single cell. The results obtained for single cells can be used for this purpose.

The acquisition times necessary to visualize clusters within the culture with sufficient contrast can be calculated by considering the number of cells present in the cluster. Assuming a sufficiently small volume in which the cancer cells are distributed, measurement times can be inferred from the intervals calculated for the single-cell case by multiplying them by the number of cancer cells present in the cluster. In the case under investigation, the assumption proposed at the beginning of the analysis was taken into account, namely that the cancer cells occupy one-hundredth of the total volume of the culture. Using this data, the acquisition times calculated to visualize such clusters are summarized in Table 5.1.

Number of drug molecules deposited on single cells	**Required acquisition time**
1×10^5	4 min 50 s
5×10^5	1 min
1×10^6	29 s
5×10^6	6 s

Table 5.1: Acquisition times required to obtain an image of sufficient quality (80% contrast) for clusters of size comparable to the detector's resolution. Cancer cells treated with the ISOLPHARM radiopharmaceutical, with varying levels of drug deposition, are analyzed to study the required measurement times.

In summary, it is observed that the acquisition times required for future in-vitro experiments with traditional cell cultures range from seconds to minutes. Even in the most pessimistic (and slightly

probable) scenario, where a limited amount of radiopharmaceutical was able to deposit on the tumor cell, the required time interval is minimal and completely compatible with the requirement for not too prolongated acquisitions demanded by in-vitro scenario.
These results allow for the conclusion that measurements with two-dimensional cell culture will demand only very limited acquisition times, thereby meeting the time constraints required by the biological sources involved in future in-vitro experiments.

5.4.2 Three-dimensional cell culture scenario

The same study must be conducted to understand the required acquisition times in the case of hydrogel-based cell culture, which presents specific characteristics in terms of volume, cell density, and the introduction of a parameter considering the distance from the detector. The first step of the analysis involves converting the acquisition time into the number of decays that can occur within a single cell, in order to determine the order of magnitude of this quantity. This conversion is performed by adopting the same approach described for the two-dimensional culture scenario. To understand how time impacts on the number of decays observed, it is necessary to know the total number of cells present within the hydrogel volume. The two required parameters to obtain this information are the volume occupied by the cancerous cells that will accumulate the radiopharmaceutical and the cell density present in the hydrogel culture. The volume where the diseased tissue is concentrated is assumed to be one-hundredth of the total culture volume, which is directly computed in Geant4. This assumption is chosen as it represents a reasonable scenario but can be adjusted and corrected when specific cultures are available for study. The cell density in the case of hydrogel-based culture has been discussed and fixed at 10^6 cells/mL, according to previous cultures produced at the BIOtech Research Center of Trento [3].
The information on the number of ill cells within the culture has to be connected to the number of drug molecules that are internalized by each single cell. The hypothesis on the type (CCK-2R receptor) and number of receptors per tumor cell is the same as discussed before as it is not influenced by the type of cell culture chosen. Therefore, the number of radiopharmaceutical molecules that can potentially bind to tumor cells remains unchanged from the previous calculation, ranging from 10^5 to 5×10^6. With these considerations concluded, the predicted number of decays over time was computed using the radioactive decay law as before. The result obtained in the case of three-dimensional cell culture is shown in Figure 5.25.

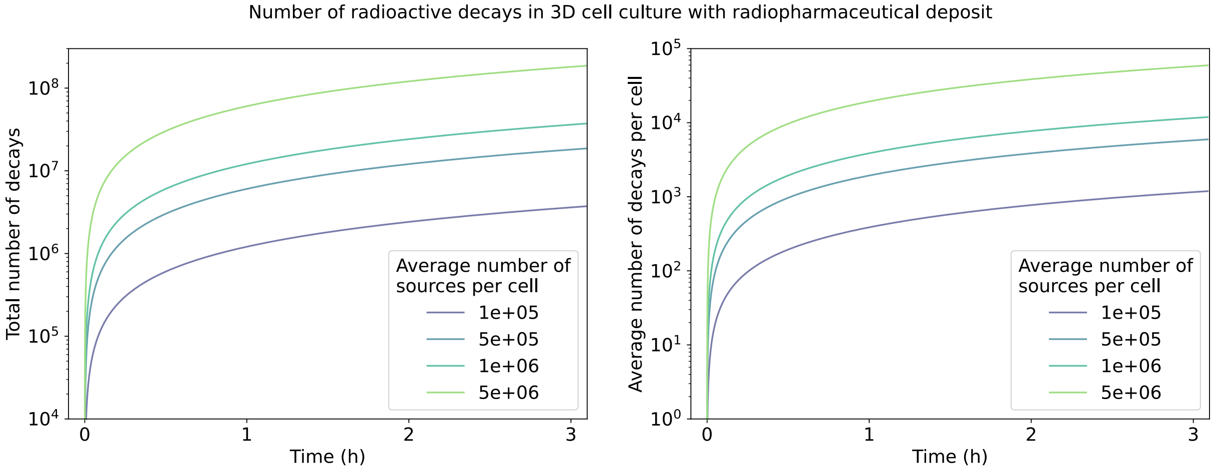

Figure 5.25: Total number of radioactive decays observed and average decays per single cell as a function of time. The cancerous cell is assumed to be collocated in a three-dimensional heterogeneous cell culture. The number of receptors per cell occupied by a radiofarmaceutical molecule is varied.

Comparing this plot with the previous Figure 5.21, it can be observed that the trend of the obtained curves is extremely similar.

The function describing the average number of decays occurring in a single cell over time allows for a direct correlation between the duration of the acquisition and the number of events observed during the measurement. This correspondence can directly link the single-cell images generated through the simulation of a fixed number of silver decays to the time variable. It may be informative to test, in this case as well, which images result when considering a number of decays per cell that allows for reasonably short acquisition times. In this perspective, the previous approach was employed, *i.e.* conducting Monte Carlo simulations while varying the number of generated events to compare the quality of the image outcomes. Similarly to what was considered for the two-dimensional culture scenario, a total number of ^{111}Ag decays ranging from 10^3 to 10^5 was simulated.

In the case of three-dimensional cell culture, it is essential to consider the distance of the radiation-emitting cell from the plane of the beta detector. The same total number of decays internal to the cell volume produces different images depending on whether the cell is located at the shallowest or deepest point inside the hydrogel volume. As the cell moves away, the number of detected particles decreases, and the image becomes broader. Therefore, it is necessary to test different distances from the detector to understand how the image varies with the source position along the z-axis. The two extreme cases were evaluated to compare the optimal and worst-case scenarios, *i.e.* when the cell is in contact with the lower and upper surfaces of the hydrogel. The resulting images are presented in Figure 5.26 and 5.27.

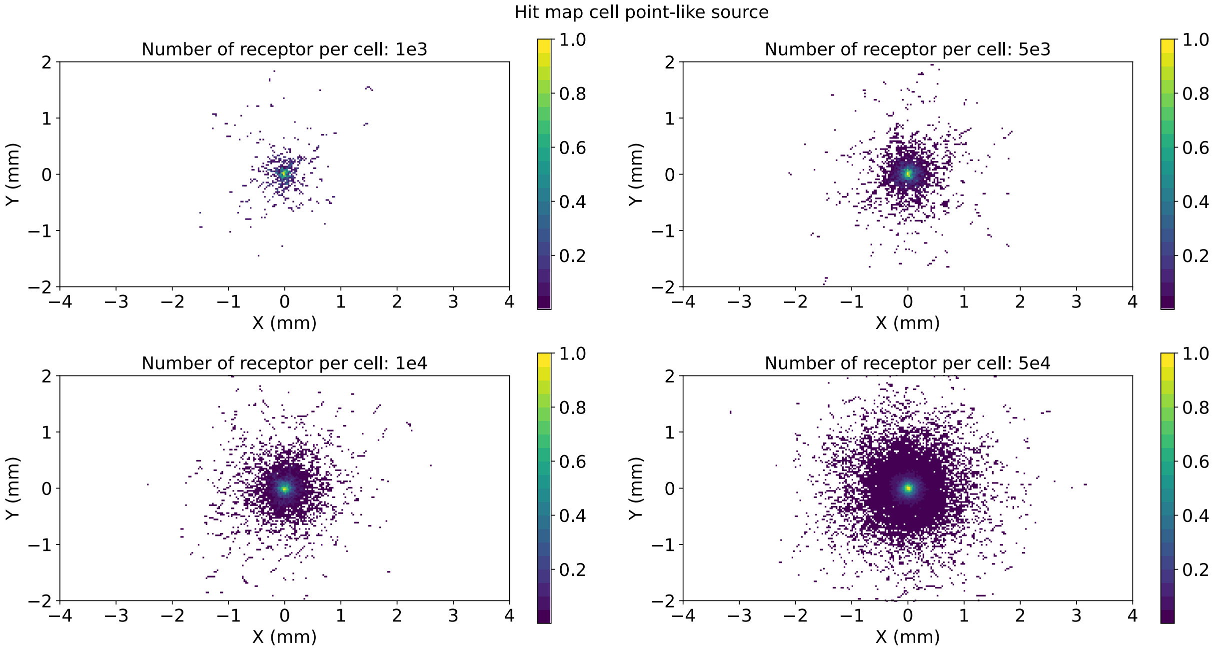

Figure 5.26: Single-cell images obtained by simulating a variable number of events, *i.e.* a variable number of ^{111}Ag decays occurring within the cell. The images illustrate the effect of different decay counts on the visualization of the radiopharmaceutical distribution within the cell. The source cell is placed in contact with the lower surface of a three-dimensional cell culture.

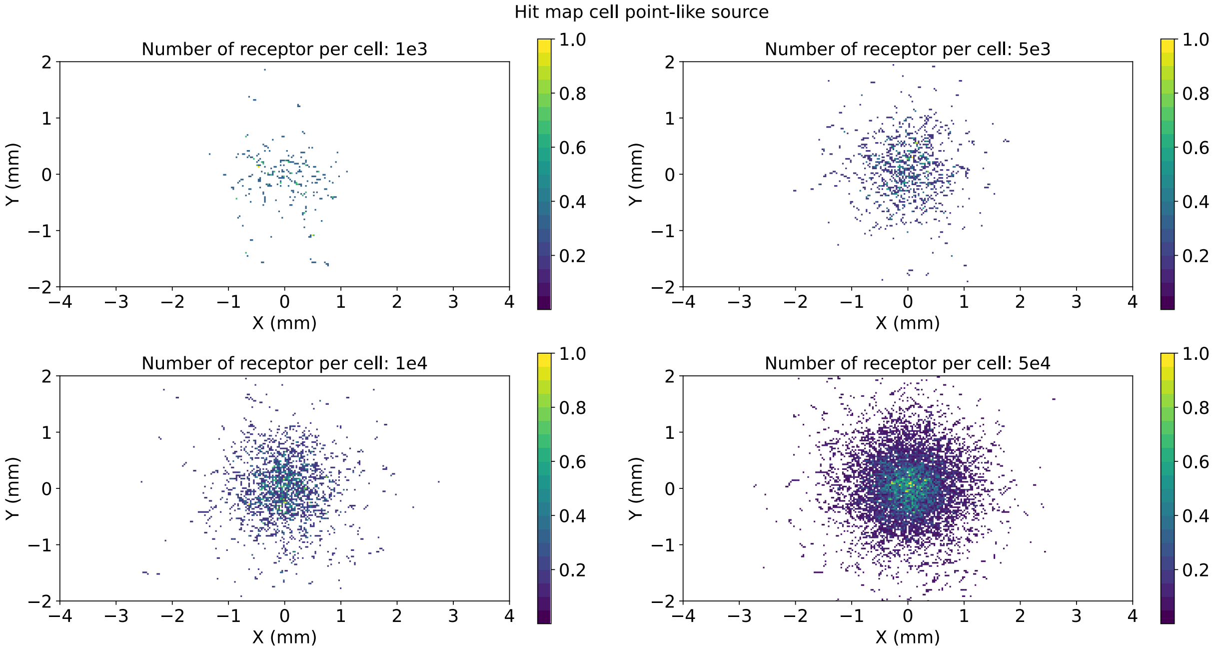

Figure 5.27: Single-cell images obtained by simulating a variable number of events, *i.e.* a variable number of ^{111}Ag decays occurring within the cell. The images illustrate the effect of different decay counts on the visualization of the radiopharmaceutical distribution within the cell. The source cell is placed in contact with the upper surface of a three-dimensional cell culture.

Firstly, it is possible to discuss some considerations on the images produced when the cell adheres to the lower surface of the hydrogel. The images are highly similar to those from the two-dimensional culture scenario, as previously observed in other analyses. However, it is noticeable that the maps for the hydrogel-based culture exhibit a slightly different pattern with more registered hits and broader distributions, leading to an increased number of peripheral bins with fewer counts. This difference can be attributed to the distinct material properties present in the hydrogel.

In the case of a cell adhering to the lower wall of a hydrogel-based culture, it seems possible to consider the same minimum limit on the number of events per cell that was discussed in the case of traditional culture. Therefore, it appears reasonable to set this limit at 10^3 events and investigate this hypothesis further in the subsequent analysis.

On the other hand, it is crucial to discuss the observations from the images when the cells are positioned at a depth of 500 μm within the culture. The images significantly deteriorate when there are only a few decay events occurring inside the cell. As discussed several times in the previous analyses, when the source moves away from the detector's surface, the recorded counts tend to decrease significantly, and the image becomes broader, making it more challenging to identify the source's position. It becomes evident that an order of magnitude of 10^3 generated events per cell is insufficient to visualize the radiation source. In this case, it may be more interesting to consider as a minimum limit condition on the number of events to generate, that of 5×10^3 events, or possibly 10^4 events.

To understand how the number of observed decays impacts the contrast in single-cell images and whether the established limits can be reasonable, the trend of the achievable contrast as a function of the number of recorded decays per single cell was analyzed. The approach followed is the same as in the previous two-dimensional culture scenario. In this case, contrast values were calculated for both cell boundary positions along the direction orthogonal to the device, aiming to understand the detector's response in each scenario. The trend extrapolated for a cell in contact with the lower surface of the hydrogel matrix is depicted in Figure 5.28(a), while for a cell at a 500 μm depth in Figure 5.28(b).

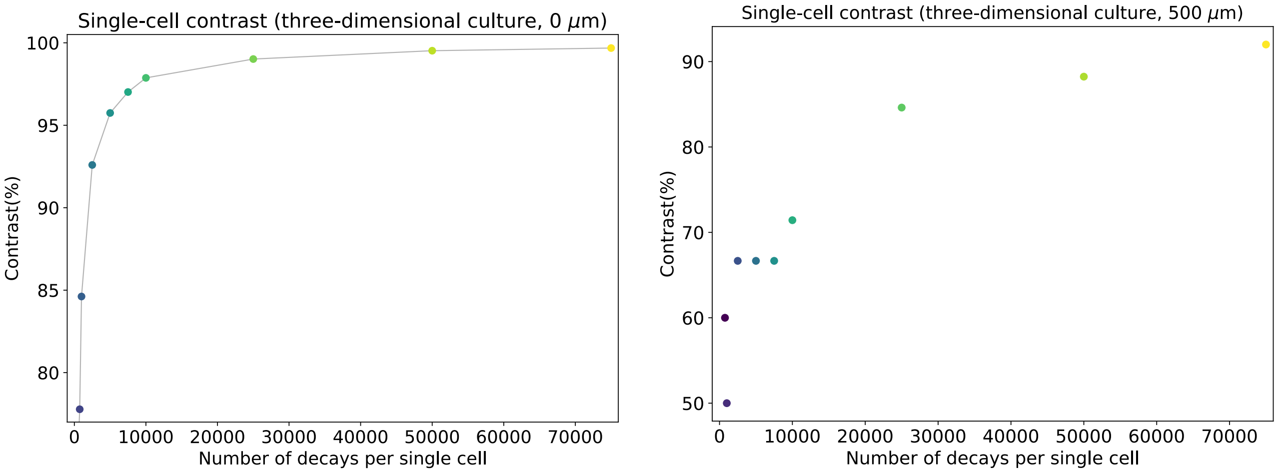

(a) (b)

Figure 5.28: Contrast characterizing the examined single-cell images (three-dimensional cell culture scenario) as a function of the number of events generated, corresponding to the number of ^{111}Ag decays inside the cell volume. The source cell is placed in contact with the (a) lower or (b) upper surface of a hydrogel-based cell culture.

For the cell located at zero depth, the data points seem to reproduce what was observed in the setup with traditional culture. Also in this case, the data trend describes a monotonically increasing function. Starting from 10^3 decays occurring in the single cell, the contrast remains consistently excellent, never falling below 80%. This behavior confirms the hypothesis put forward and that has already been utilized for the two-dimensional cell culture scenario: a total number of ^{111}Ag decays equal to 10^3 within a specified time interval provides a high-quality image.

The case of the cell in contact with the bottom surface of the hydrogel-based culture is different. The curve replicates the monotonically increasing trend observed in previous cases but is characterized by an interval of constant contrast around 10^4 events. However, the most significant difference is associated with the deterioration of contrast when the source is at the maximum distance from the instrument. The images produced achieve a contrast of 80% only if the total simulated events exceed 10^4, making it impossible to obtain high-contrast images in reasonable acquisition times. In the condition where the source is placed at the maximum distance from the device, it is then reasonable to require the measurement of at least 10^4 events, extending the measurement times. Despite the achievable contrast being rather small ($\approx 70\%$), this reference meets the time constraints posed by a biological source. However, it is essential to consider that this scenario represents the most pessimistic scenario possible in the case of hydrogel-based culture: in most cases, the cells will tend to distribute at depths below the maximum limit, leading to a relative improvement in the image.

The conclusion of the performed study is represented by the calculation of the acquisition times required for the production of an image of sufficient quality, in this case, considering different source positions along the z-axis. The first step to perform this calculation is represented by the estimation of the intervals necessary to observe a fixed number of ^{111}Ag decays per single cell. For the reasons discussed, in the case of a cell at the minimum distance from the device, this number has been set at 10^3, while in the case of a cell at a depth of 500 μm in the hydrogel volume, the value of 10^4 was considered. Starting from these values, it is possible to obtain the necessary times by utilizing the curves in Figure 5.25. Figure 5.29(a) illustrates when the number of decays per cell reaches the set value for the single cell case in the scenario of a cell adhering to the lower wall of the hydrogel, while Figure 5.29(b) to the upper surface.

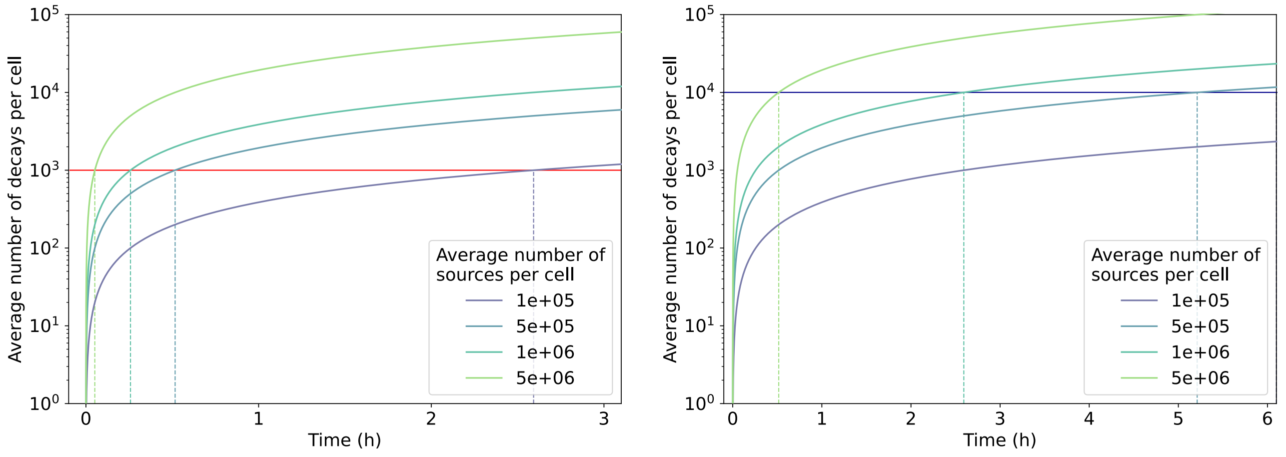

(a)

(b)

Figure 5.29: Average number of radioactive decays per single cell as a function of time. The cancerous cell is assumed to be collocated in a three-dimensional heterogeneous cell culture. The number of receptors per cell occupied by a radiofarmaceutical molecule is varied. The red and blue line highlights respectively where the decay counts are equal to (a) 10^3 and (b) 10^4.

The information obtained from the single-cell images allows for inferring what could be suitable acquisition times even when cancer cells group into small clusters. As anticipated in the previous section, at the end of the growth phase, cancer cells tend to form clusters. It is then useful to understand the time intervals required to obtain meaningful acquisitions when studying one of these clusters, using the results from single-cell analysis.
The hypothesis put forward in this scenario is also that the tumor cluster occupies a volume equal to 1% of the total available volume within the three-dimensional culture. Using the same approach as previously utilized, it is then possible to deduce directly from the single-cell temporal information what acquisition times may be suitable for producing images of these clusters with sufficient quality. Table 5.2 summarizes the calculated acquisition times.

Number of decays	**Number of drug molecules deposited on single cells**	**Time required to observe fixed number of events**
10^3	1×10^5	5 min 1 s
	5×10^5	1 min 0 s
	1×10^6	30 s
	5×10^6	6 s
10^4	1×10^5	11 min 42 s
	5×10^5	10 min 0 s
	1×10^6	4 min 59 s
	5×10^6	1 min 2 s

Table 5.2: Acquisition time required to observe a total of 10^3 and 10^4 decays within a single tumor cell in three-dimensional cell culture. Cancer cells treated with the ISOLPHARM radiopharmaceutical, with varying levels of drug deposition and different distances from the detector surface, are analyzed to study the required measurement times.

In all the cases analyzed, it is observed that the minimum measurement intervals do not exceed a few minutes. The calculated times are consistent with what has been observed in the case of two-dimensional culture and are compatible with the requirements necessary for in-vitro measurements with biological sources.

Similarly to what has already been observed, the three-dimensional culture scenario also lends itself to the possibility of obtaining high-quality acquisitions even within very short times, allowing for the production of an image with sufficient contrast in a matter of minutes. This result verifies that the instrument under analysis is suitable for working with biological sources (both two-dimensional and three-dimensional) and allows for the acquisition of activity maps in sufficiently short times.

5.5 Image production in realistic in-vitro scenario

The previous analyses have enabled the investigation and optimization of the experimental setup planned for future in vitro experiments within the ISOLPHARM project. Information gathered through Monte Carlo simulations has revealed the advantages and limitations of the β-imaging system, which is being developed to produce two-dimensional activity maps for cell cultures, demonstrating the adaptability of the project to measurement requirements.

After having tested the characteristics of the beta detector under development, it is interesting to conduct a study of the device's application in a comprehensive in-vitro scenario. While previous analyses focused on simulating a single chip to investigate the ALPIDE's response to the planned sources, this study aims to analyze how the detector behaves in its final configuration (both 2 × 2 and 4 × 2 geometries). The purpose of these tests is to provide examples of images that the device can yield when introduced into different in-vitro experimental scenarios. By integrating the previously obtained information, it becomes possible to analyze the maps that will be produced when an entire cell culture, including a tumor cell line, is investigated. These images will provide concrete examples to understand how the radioisotope deposition will be imaged by the beta detector in upcoming experiments.

To make the studied scenario as realistic as possible, the simulation replicates the conditions verifiable after a predetermined acquisition time. As discussed in Section 5.4, the time required to obtain a good-quality image for each cell depends on how many radioisotope molecules are internalized by the cancer cells. This parameter is stochastic and influences the number of ^{111}Ag isotopes deposited, thereby affecting the maximum number of electrons that can be produced and potentially detected by the detector. To replicate a realistic application, it is assumed that each cell within the culture will have a random number of drug molecules deposited, ranging between 10^5 and 5×10^6. Due to this variability, the selection of the appropriate measurement time becomes arbitrary, considering the calculated times to obtain a sufficient number of hits for each cell to be visualized (see Tables 5.1 and 5.2). For this analysis, the chosen acquisition interval is 15 minutes, a time frame that appears reasonable for the experimental conditions that will be encountered. In addition to aligning with the biological requirements of the cultures, the chosen time interval facilitates carrying out simulations of relatively high computational complexity and time consumption. Incorporating numerous source cells and a larger number of active pixels within the detector, the simulation entails intricate geometries and dynamics, which significantly extend the computational times making it challenging to simulate longer acquisition times.

Another important factor to consider when characterizing the cell culture used in the experiments is the proportion of healthy and cancerous tissue. This parameter is highly arbitrary and will need adjustment when working with actual cultures for experiments. As previously suggested in Section 5.4, it is assumed that the tumor cells constitute 1% of the total cell count in the studied cultures. This choice has also been made for reasons related to the feasibility of the simulations to be conducted: the introduction of a very high number of source volumes (along with the need to simulate a large number of events in this case) makes GEANT4 simulations extremely time-consuming. The consideration of a tumor volume equal to 1% of the total volume allows for reducing these times while still obtaining interesting results. This condition allows for specific results for the selected proportion but can be further refined when more information becomes available, leading to a more accurate adjustment.

5.5.1 Two-dimensional cell culture scenario

The first case analyzed is that of two-dimensional cell culture. These cultures offer the advantage of keeping the cells at a constant distance from the detector but exhibit biological disadvantages (as summarized in Table 3.2). The size of traditional cultures is constrained by the standard petri dishes or flasks used for their maintenance. Particularly for the studied in-vitro application, tissue culture dishes with a bottom designed to minimize the material volume and thus the attenuation of particles emitted by the radioisotope are preferred. Several solutions are available on the market, with different products designed to achieve thin-bottom culture dishes, varying according to the manufacturer. For the examples studied (also in previous sections), the dishes adopted by the Pharmacology Department at the University of Padova were chosen [112], selecting the petri dishes that met the specified requirements. These cylindrical containers have a thin bottom made of patented material, highly similar to mylar but more robust. The available dimensions are as already described in the setup modeling presented in Chapter 4. During the characterization of the 2 × 2 and 4 × 2 detector configurations, the same source geometry was considered, without the possibility of adapting to a larger surface.

One more crucial factor to consider is the cell density characterizing the cell culture. To obtain a generalized result, the most common order of magnitude for the cell density in the case of two-dimensional cell culture, namely 10^7 cells/mL, was selected (analogous to what was chosen in Section 5.4). The information about the density and source geometry (and hence the volume occupied by the cells) allows for knowing the total number of cells that can be incorporated into the modeling of the culture. Once these parameters were incorporated into the GEANT4-based setup model, the Monte Carlo simulations for image production were conducted. Besides comparing two possible detector configurations, two scenarios that can occur biologically within the culture were selected to be compared. As discussed in Section 5.4, within heterogeneous cultures, cancer cells commonly tend to aggregate into one or more clusters dispersed within healthy tissue. To accurately model the distribution of cancer cells within the medium, the two most common scenarios when considering solid tissue were chosen: the case where the tumor cells compact into a single volume or spread across multiple clusters.

In the first scenario, it is assumed that the cancerous tissue is confined to a single colony within the cellular medium. In the produced simulation, it is specified that the emitting cells are randomly distributed within a confined volume representing one-hundredth of the total volume. Under these conditions, a total of 7.9×10^6 events are simulated to replicate a 15-minutes acquisition time. The image produced by the 2 × 2 beta detector under these assumptions is illustrated in Figure 5.30.

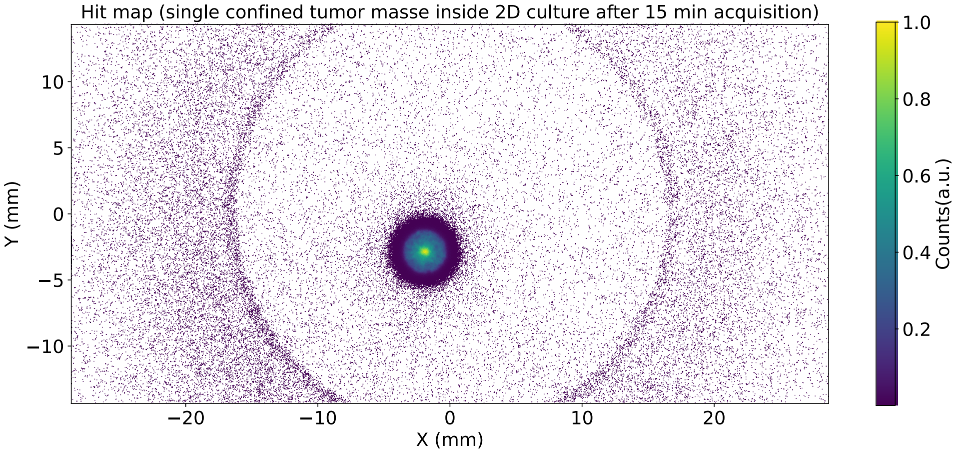

Figure 5.30: Image of an ill volume obtained by simulating a single tumor mass (circular) with a maximum diameter of 3.2 mm inside a two-dimensional heterogeneous culture. Cancer cells are randomly distributed within the diseased tissue volume. The image simulates a 15-minutes acquisition. The radiopharmaceutical is only internalized by tumor cells: a random number of drug molecules, chosen within the range [10^5, 5×10^6], is deposited on each cell.

The image clearly delineates the region corresponding to the tumor volume, exhibiting a well-contrasted central area against the background. It is noteworthy that the center of the volume is characterized by a high-count region, resulting from a crossfire effect between the cancer cells.

In the image, the outlines of the Petri dishes used to contain the traditional culture are immediately noticeable. This outline can be easily explained by considering the scattering effects that particles undergo when interacting with the lateral walls of the container instead of the air. In previous simulations, this behavior was not evident due to the use of a single ALPIDE chip, resulting in a smaller available surface area.

To understand the type of information extractable from this image (and the subsequent ones), the region was characterized with a count threshold that effectively distinguishes it from the background, represented by the darkest color in the colormap. The choice of threshold for eliminating counts is arbitrary, and it was decided to consider only the region of counts that clearly stands out from the background with fewer hits. The selected threshold zeroes all bins with a hit count lower than 10% of the count in the most populated bin (in the case of a normalized histogram, 1). The resulting image, with the retained area highlighted, is presented in Appendix (Figure 6.11). This operation also allows for estimating the extent of the foreground region.

As the geometry is symmetric, the dimensions of the central area are evaluated along the two axes, x and y. The calculation was carried out by identifying, for each of the two directions, the row or column where the retained area had the highest number of occupied bins. The image size was thus obtained by computing this value and converting it into spatial dimensions. The acquired data is collected and compared with the expected values in Table 5.3.

Axis	**Real dimension** (mm)	**Estimated dimension** (mm)
x	3.20	3.28
y	3.20	3.30

Table 5.3: Dimensions of the foreground region (threshold equal to 10% of maximum counts) in the image of a single tumor mass in two-dimensional culture (Figure 5.30).

The estimations appear to provide a reliable prediction of the diseased volume. Although the calculated dimensions slightly overestimate the actual ones, this effect could be attributed to the inherent distance between the two-dimensional culture and the detector, attributed to the petri dish container. Despite being a relatively small intermediate thickness, this introduces image distortion due to the cone of emission of beta particles released by the radiopharmaceutical. By considering this factor, it is possible to conclude that the examined image not only enables the visualization of the area where the drug is internalized but also provides a reasonably accurate estimation of the extent of this surface. This validation ensures that any radiopharmaceutical deposits accumulating outside the tumor tissue and in its vicinity can be detected and further studied.

The next scenario examined involves modeling a heterogeneous culture where cancer cells tend to form individual clusters within the medium. In the considered case, a total of 10 clusters of cancer cells distributed randomly within healthy tissue were chosen. To replicate various types of different behaviors, the volumes in which tumor cells are located have varying sizes. The sum of these volumes amounts to 1% of the total occupiable volume. In the simulation, cells are distributed among the possible clusters based on a probability proportional to the volume of that region. This approach ensures that while the various tumor regions are not deterministically filled, volumes with larger diameters are occupied by a greater number of particles.

In this condition as well, a simulation was conducted to replicate a 15-minute measurement, involving a total of 8.0×10^6 events. The number of events varies because the decision was made to randomize the number of drug molecules internalized per single cell, as previously anticipated. This choice results in a varying total number of decays observed after 15 minutes, depending on the total number of available ^{111}Ag radioisotopes. The image obtained in this scenario exploiting the 2 × 2 configuration of the beta detector is presented in Figure 5.31.

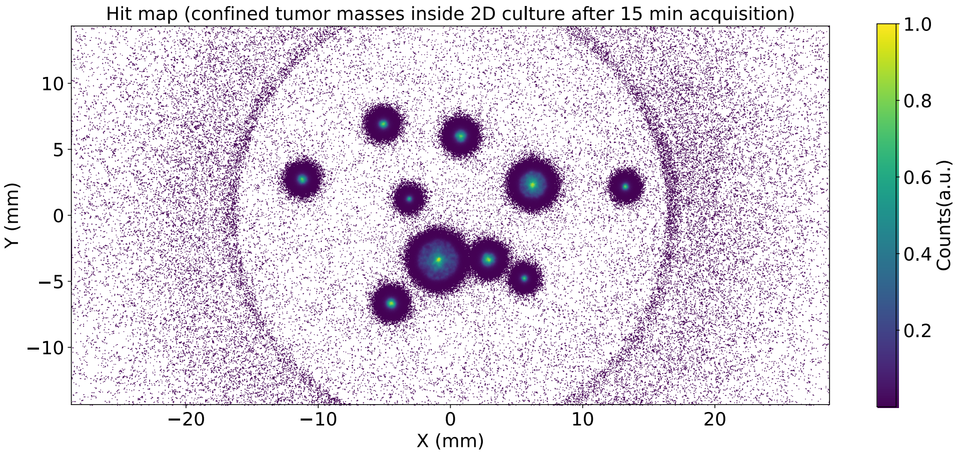

Figure 5.31: Image of an ill volume obtained by simulating different confined tumor masses (circular) with a variable dimension inside a two-dimensional heterogeneous culture. Cancer cells are randomly distributed within every single diseased volume. The image simulates a 15-minutes acquisition. The radiopharmaceutical is only internalized by tumor cells: a random number of drug molecules, chosen within the range $[10^5, 5{\times}10^6]$, is deposited on each cell.

The produced image clearly distinguishes all 10 introduced volumes, each associated with an area of varying dimensions. Consistent with previous observations, each tumor cluster is depicted as a central region (more or less defined in this instance) surrounded by a low-count background. Given the same acquisition duration, it is natural to anticipate that each cluster will produce a less defined image compared to the previous scenario where all cells are enclosed within a single volume. Nonetheless, the overall image provides sufficient contrast and clarity.

To ascertain whether it is also possible to recognize and measure the sizes of such clusters when diseased cells aggregate within distinct volumes, a similar analysis to the one conducted previously was performed. When dealing with various individual clusters, the process of identifying different areas in the image proves to be more labor-intensive compared to the single-volume case. While previously it was sufficient to eliminate low-count regions to locate the foreground area, in this context, more complex algorithms are necessary, capable of segregating the available data into individual clusters. This operation can be accomplished using a Machine Learning (ML) approach.

In this analysis, the DBSCAN algorithm (Density-Based Spatial Clustering of Applications with Noise) was employed. DBSCAN, or Density-Based Spatial Clustering of Applications with Noise, represents a clustering algorithm employed for grouping data points based on their spatial density [124], [125]. It characterizes clusters as dense regions within the data, separated by regions of lower density. The algorithm commences by selecting a data point and proceeds to build clusters by connecting neighboring points within a defined radius. Clusters that meet the criteria for having a sufficient number of neighboring points continue to expand. Conversely, data points failing to satisfy the density requirements are regarded as noise or outliers. This unique approach allows DBSCAN to identify clusters with arbitrary shapes, making it a robust choice for various data scenarios. In this specific analysis, the implementation of the DBSCAN algorithm was executed using the Python library `sklearn` [126],

[127].

The clustering algorithm is executed after an initial noise reduction operation on the image, similar to previous processes: bins with counts less than 5% of the most populous bin are set to zero. This method streamlines the application of the algorithm, rendering it faster and more accurate. In this instance, a more conservative approach was favored regarding discarded bins, retaining bins even with fewer counts than the previous method. This choice is tied to the lower contrast present within individual clusters between foreground and background. Consequently, regions near the emission point could also be characterized by minimal counts. To achieve a more balanced analysis, an effort was made to include those meaningful low-count areas.

The DBSCAN algorithm successfully identified all 10 clusters present in the image. The accumulation regions identified through the performed operation are displayed in Figure 5.32, with each region identified by a specific color overlay on the original map.

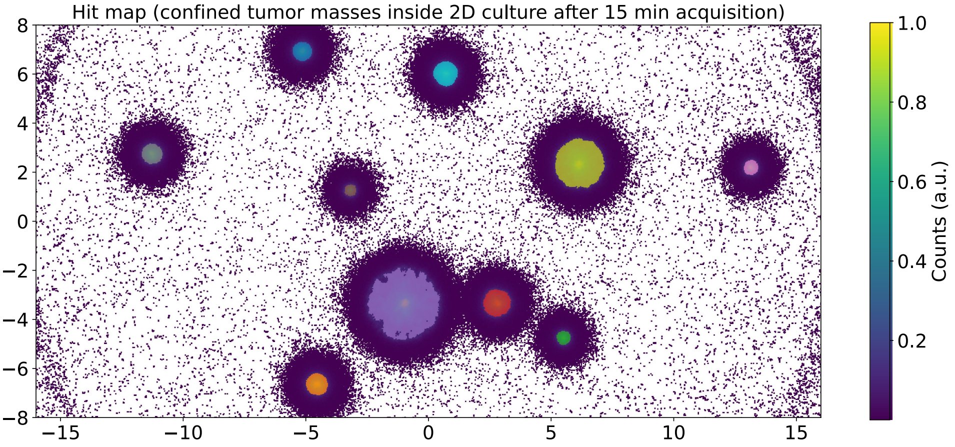

Figure 5.32: Image of an ill volume obtained by simulating different confined tumor masses (circular) with a variable dimension inside a two-dimensional heterogeneous culture. Cancer cells are randomly distributed within every single diseased volume. The image simulates a 15-minutes acquisition. The radiopharmaceutical is only internalized by tumor cells: a random number of drug molecules, chosen within the range [10^5, $5{\times}10^6$], is deposited on each cell. The identified clusters are represented using different colors by applying the DBSCAN algorithm.

From the image, it can be observed that the DBSCAN algorithm manages to identify all the areas corresponding to the 10 clusters satisfactorily. Smaller clusters are recognized with excellent precision, while it is observed that the algorithm struggles more to define the boundaries of larger clusters, possibly due to their less uniform density.

The process of cluster recognition also enables the study of their shapes. Analogously to what was previously examined, it becomes interesting to verify whether precise information about the dimensions of each cluster can be extracted from the image. The approach adopted to calculate the extent along the two x and y axes of each of the areas identified by the clustering algorithm remains the same as previously described. For each identified cluster, its projection along the two spatial axes is characterized. The maximum amplitude of each profile, in terms of bins, is determined and subsequently translated into spatial dimensions. The results computed using this approach are presented in Table 5.4 where, for each of the identified clusters, the estimated size is compared to the actual size set by the simulation.

Cluster ID	**Axis**	**Real dimension** (mm)	**Estimated dimension** (mm)	**Cluster ID**	**Axis**	**Real dimension** (mm)	**Estimated dimension** (mm)
1	x	3.04	2.94	6	x	0.67	0.90
	y	3.04	2.83		y	0.67	0.92
2	x	2.02	2.04	7	x	0.66	0.78
	y	2.02	2.10		y	0.66	0.87
3	x	1.01	1.18	8	x	0.43	0.67
	y	1.01	1.20		y	0.43	0.67
4	x	0.88	1.02	9	x	0.41	0.64
	y	0.88	1.02		y	0.41	0.64
5	x	0.72	0.95	10	x	0.34	0.53
	y	0.72	0.90		y	0.34	0.53

Table 5.4: Dimensions of the foreground clusters (identified through DBSCAN clustering algorithm) in the image of different artificial volumes simulated as confined tumor masses in two-dimensional culture (Figure 5.32).

In this comparison, it is noted that the cluster sizes determined through the described process are less accurate than those arising from emissions originating from a single tumor volume. With the exception of larger volumes, the calculated emission volume sizes tend to overestimate the actual dimensions. In general, this effect could result from a combination of multiple factors. On one hand, the scattering effect of particles emitted in radioactive decay plays a role: since the detector is positioned at a defined distance from the cellular volumes, the particles scatter against intermediate materials, broadening the beam defined by the cell. On the other hand, it should be noted that the clustering process can be refined using algorithms specifically designed for this purpose. In this case, one of the most commonly employed algorithms for clustering problems has been adopted. However, the recognition process can be optimized and enhanced for the specific challenge under investigation by embedding even more advanced ML techniques.

Considering these observations, it is concluded that the method followed allows for the correct identification of cellular clusters and estimation of the dimensions of each recognized region. Despite the limitations of the employed process, it is observed that the dimensional estimations obtained are nearly always within the instrument's resolution values, which are set at 0.2 mm.

Concluding the analysis of the two-dimensional cell culture scenario, the aim was to investigate the type of images that can be produced using the 4 × 2 configuration of the beta detector. Implementing this geometry proves useful for potential application in future experiments.

In terms of the image production process and characteristics of the obtained image, no differences are noted compared to the previously analyzed configuration, *i.e.* the 2 × 2 configuration. For this reason, the two images obtained by evaluating the 4 × 2 detector configuration, both for traditional cultures where cancerous cells cluster into a single volume and for cases where they cluster into different volumes, are included in the Appendix. The collected images are depicted in Figure 6.12 and 6.14.

5.5.2 Three-dimensional cell culture scenario

The analysis continued by exploring the same scenarios involving tumor volumes within a realistic hydrogel-based cell culture. Despite the advantages of three-dimensional cultures in providing an environment more similar to in-vivo conditions, they bear the limitation of potential cell placement within the hydrogel at a greater distance from the detector. This characteristic deteriorates the resolution provided by the instrument and negatively affects the possibility of precise determination of small emission volumes. As in the previous sections, the culture is modeled as a hydrogel volume within which cells are distributed in a three-dimensional medium. A more detailed description of the developed model is summarized in Chapter 4.

A specific aspect of three-dimensional culture is the cell density within the medium. This information has been defined based on data provided by the BIOtech Research Center of Trento [3], which will produce the hydrogel-based cultures for the ISOLPHARM project. The density is considered to be 10^6 cells/mL. This parameter is essential for computing various factors, starting from the total number of cells present in the culture volume.

Incorporating all the aforementioned information and the established density, it was possible to model different tissue tumor patterns similar to what was previously developed, distinguishing between a scenario where cancer cells aggregate into a single cluster and one where multiple distinct clusters are observed.

The initial case analyzed is represented by the scenario where cancerous cells are aggregated within a single volume, again set at one-hundredth of the total volume for simulation ease. By randomizing the number of drug molecules deposited on each cell, the number of observed and simulated events after 15 minutes is 7.7×10^6. The image obtained evaluating the beta detector in its 2 × 2 configuration with these parameters is presented in Figure 5.33.

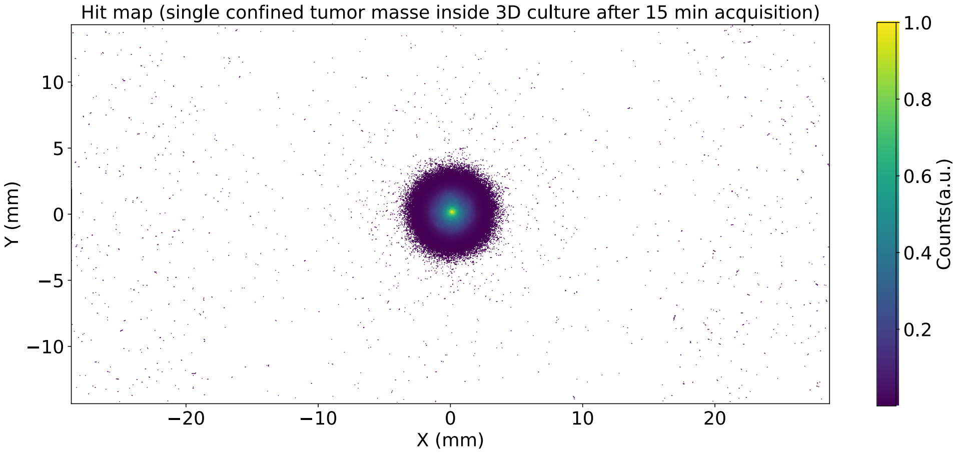

Figure 5.33: Image of an ill volume obtained by simulating a single tumor mass (circular) with a maximum diameter of 2.8 mm inside a hydrogel-based heterogeneous culture. Cancer cells are randomly distributed within the diseased tissue volume. The image simulates a 15-minutes acquisition. The radiopharmaceutical is only internalized by tumor cells: a random number of drug molecules, chosen within the range $[10^5, 5{\times}10^6]$, is deposited on each cell.

Although cells are arranged randomly along the direction perpendicular to the detector's surface, it can be observed that the image of the diseased volume is well-defined and exhibits strong contrast, similar to what was observed in the two-dimensional culture.

These data enable clear identification of the region of interest and its features. The analysis applied to the image follows the same methodology described for the traditional culture, evaluating those areas of the image where counts exceed 10% of the maximum counts in the most populated bins. While the selected region is depicted in Figure 6.10 in the Appendix, the dimensions of this surface along the x and y axes, calculated as previously described, are compiled in Table 5.5. The calculation method employed to estimate the clusters' dimensions remains consistent with the approach outlined in the preceding sections: the projections along the two axes of the histogram are evaluated, and the extent along the two dimensions of the row/column with the highest number of occupied bins is estimated. Ultimately, these values are converted into lengths.

Axis	**Real dimension** (mm)	**Estimated dimension** (mm)
x	2.82	2.91
y	2.82	2.88

Table 5.5: Dimensions of the foreground region (threshold equal to 10% of maximum counts) in the image of an artificial volume simulated with a single tumor mass in hydrogel-based culture (Figure 5.33).

The calculated results must be interpreted while considering the previously mentioned factors. Due to the distance between the source cells and the instrument (which can also vary from cell to cell in this case), the cross-section of the particle volume reaching the detector is physically larger than at the emission point. This accounts for the slight discrepancy between the actual dimensions of the tumor cluster and those estimated through the described procedure. Nevertheless, the image allows for reasonably accurate identification of the region of interest, even considering the limitation of the hydrogel-based culture attributed to the introduction of the depth parameter.

The second step in the analysis of a three-dimensional culture in a realistic scenario involves introducing a model of a heterogeneous culture where diseased cells cluster into distinct volumes. To replicate this setup, a similar approach to the previous one was employed: 10 cancerous clusters were simulated, collectively occupying one-hundredth of the total volume available in the medium. Cells group together into colonies of varying sizes, following a probability proportional to their size.

The Monte Carlo simulation conducted to model the 15-minute acquisition duration involved a total of 7.9×10^6 decays of ^{111}Ag isotopes. The image produced with these parameters integrating the beta detector in a 2 × 2 configuration is illustrated in Figure 5.34.

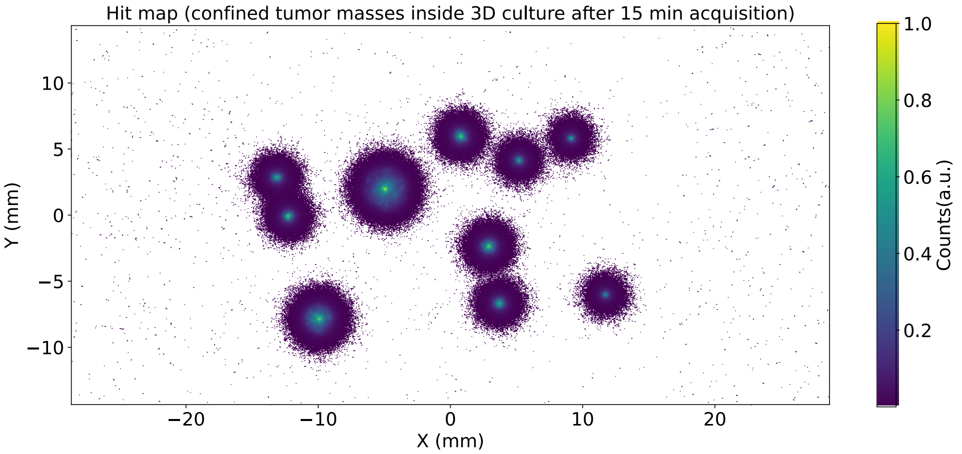

Figure 5.34: Image of an ill volume obtained by simulating different confined tumor masses (circular) with a variable dimension inside a hydrogel-based heterogeneous culture. Cancer cells are randomly distributed within every single diseased volume. The image simulates a 15-minutes acquisition. The radiopharmaceutical is only internalized by tumor cells: a random number of drug molecules, chosen within the range [10^5, $5{\times}10^6$], is deposited on each cell.

It is possible to note that the clusters depicted in this image appear to be less resolved and with lower contrast compared to the results yielded in the two-dimensional culture case.

It is possible to highlight a worsening of the visualization quality for smaller clusters when dealing with a three-dimensional culture. These clusters are the less populated ones and it is difficult to precisely distinguish them by the human eye. This degradation in contrast is entirely justified by the fact that cells might be positioned at distances from the detector's surface bigger than the condition of adherence to the lower wall of the hydrogel matrix. As previously investigated in Section 5.4 (and shown in Figure 5.28(b)), when a cell is at the maximum distance from the device, the contrast significantly degrades, especially if the number of decays recorded within that cell's volume is limited. In order to assess the feasibility of detecting the smaller clusters and determining their dimensions, a clustering algorithm was employed. The DBSCAN algorithm was utilized to successfully identify all 10 clusters, following a methodology similar to the previously proposed one. Data preprocessing was conducted prior to the algorithm's application, eliminating bins with too low counts (bins that collect a number of hits inferior to the 10% of the maximum counts per bin in the histogram). Figure 6.13 in the Appendix illustrates the identified clusters.

The final step in verifying the ability to investigate the defined clusters involves estimating their dimensions. For each individual cluster, the previously outlined calculation is performed, yielding the results presented in Table 5.6.

Cluster ID	**Axis**	**Real dimension** (mm)	**Estimated dimension** (mm)	**Cluster ID**	**Axis**	**Real dimension** (mm)	**Estimated dimension** (mm)
1	x	3.21	2.93	6	x	0.71	0.92
	y	3.21	2.89		y	0.71	0.95
2	x	2.14	1.99	7	x	0.64	0.81
	y	2.14	2.07		y	0.64	0.82
3	x	1.07	1.15	8	x	0.46	0.73
	y	1.07	1.26		y	0.46	0.73
4	x	0.92	1.06	9	x	0.43	0.62
	y	0.92	1.12		y	0.43	0.67
5	x	0.76	0.95	10	x	0.37	0.59
	y	0.76	0.95		y	0.37	0.62

Table 5.6: Dimensions of the foreground clusters (identified through DBSCAN clustering algorithm) in the image of different artificial volumes simulated as confined tumor masses in hydrogel-based culture (Figure 6.13).

On average, the determined dimensions partially overestimate the actual values. Apart from accounting for the distortion of cluster sizes due to the distance between cells and the detector, potential errors related to the application of the clustering algorithm need to be considered in this calculation. Nevertheless, the employed approach enables a sufficiently precise analysis of the available image, allowing for the identification and measurement of each defined cluster.

A brief observation can be made regarding the larger cluster. In this instance, a counter-trend is noticeable in the determination of cluster sizes, likely linked to a limitation in accurate cluster identification. This issue could be refined by developing more sophisticated clustering algorithms designed specifically for the examined problem.

Considering the discussed results, it can be concluded that even in a scenario involving short acquisitions (15 minutes) in a three-dimensional culture, readable and analyzable images are obtained using the performed procedure. This method enabled the accurate identification of tumor clusters of various sizes and the determination of the dimensions of each within a range of a few tenths of a millimeter.

The analysis of the three-dimensional scenario concluded by also investigating the case of a 4 × 2 configuration for the beta detector to determine the images that can be produced. This setup allows the utilization of a larger acquisition surface, potentially accommodating the geometries of three-dimensional cultures or employing multiple petri flasks for traditional cultures. The images obtained by modeling the setup described in the previous paragraphs are presented in the Appendix (Figures 6.15 and 6.16).

Chapter 6

Conclusions

The discussed thesis work aimed to provide an initial investigation of the beta detector that will be developed in the upcoming years for in-vitro experiments within the ISOLPHARM project. By considering a geometry that employs 4 or more ALPIDE chips in a flat setup, it is possible to obtain a cost-effective instrument capable of capturing two-dimensional images depicting the distribution of a radiopharmaceutical within various cell cultures. The construction of this detector aims to provide a device that will determine the regions of radiopharmaceutical ^{111}Ag-based internalization in the ISOLPHARM prototype for future in-vitro experiments. This testing will verify the drug's ability to selectively bind to tumor cells while monitoring any potential impacts on normal tissue.

This thesis presented a preliminary investigation of the detector that will be developed in the coming years. The instrument was modeled using GEANT4 to assess its performance through Monte Carlo simulations. Specifically, the developed simulations included a modeling of the possible types of cell cultures to be utilized in ISOLPHARM experiments, encompassing two-dimensional traditional cultures and three-dimensional hydrogel-based cultures.

The ability to replicate the instrument's performance was investigated by comparing GEANT4 simulations with real data. An ALPIDE chip was employed for initial testing with this device. Measurements with collimated laboratory sources were conducted using a dedicated DAQ system built for ALPIDE configuration and data acquisition management. Experimental two-dimensional images were compared to images produced by Monte Carlo simulations adapted to the utilized setup. This comparison verified that the modeled detector accurately predicts the response of the real MAPS.

The tested simulation was then utilized to explore the characteristics and potential of the imaging system under development. The detector was integrated into a setup featuring cell cultures: the deposition of radiopharmaceutical was modeled by assuming that ^{111}Ag decays within cellular volumes where the drug is internalized. The GEANT4-designed application allowed testing the response and performance of the detector in a realistic context in preparation for future experiments.

The conducted analysis led to the following conclusions:

- The application of a 1 keV threshold to the beta detector can eliminate potential noise sources and multiple hits effects, *i.e.* hits caused by individual particles undergoing scattering processes within the sensitive volume, activating multiple pixels;
- The instrument's resolution, calculated considering a point-like source consisting of a single cell placed at a proper distance to replicate a real experimental environment, is 0.2 mm for a two-dimensional culture scenario. The resolution varies within a range of 0.2 mm to 1 mm for hydrogel-based culture scenarios due to the three-dimensional nature of the culture;
- Optimal acquisition times are strongly influenced by the number of drug molecules a cell can internalize and by the sizes of clusters that tumor cells form within normal tissue. The measure-

ment times required to visualize the distribution of clusters of sizes comparable to the instrument's resolution range from a few seconds to few minutes, demonstrating compatibility with the requirements imposed by biological sources;

- Images generated by the detector in heterogeneous cultures, where clusters of tumor tissue coexist with normal tissue, effectively delineate the volumes hosting radiopharmaceutical deposits. The application of clustering algorithms facilitates automated identification and sufficiently precise dimensional analysis of these volumes.

In conclusion, the conducted study provided a comprehensive investigation of the device under development, confirming its suitability for the intended purpose. The designed simulations not only predicted the detector's performance but can also be applied for future assessments during the instrument's construction and in-vitro experiments.

Appendix

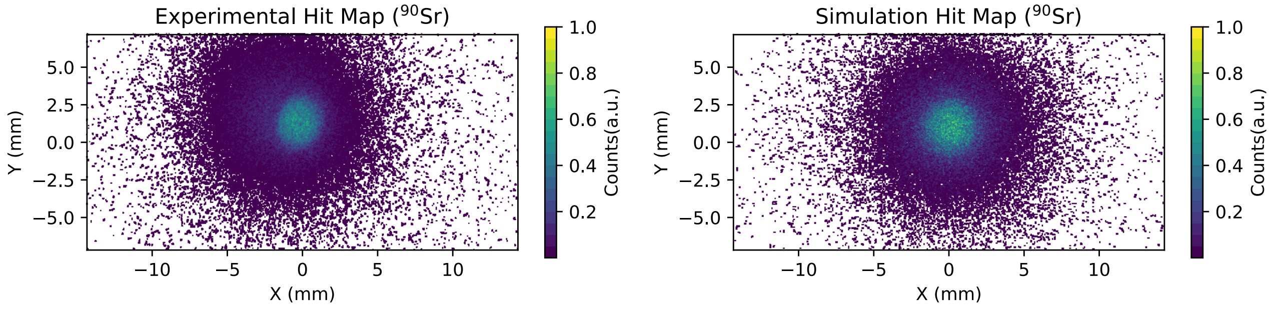

Figure 6.1: Comparison between the 2D image experimentally obtained using a ^{90}Sr source during the ALPIDE detector tests and the 2D image obtained through the Monte Carlo simulations via Geant4. The source is positioned 2 mm away from the detector surface.

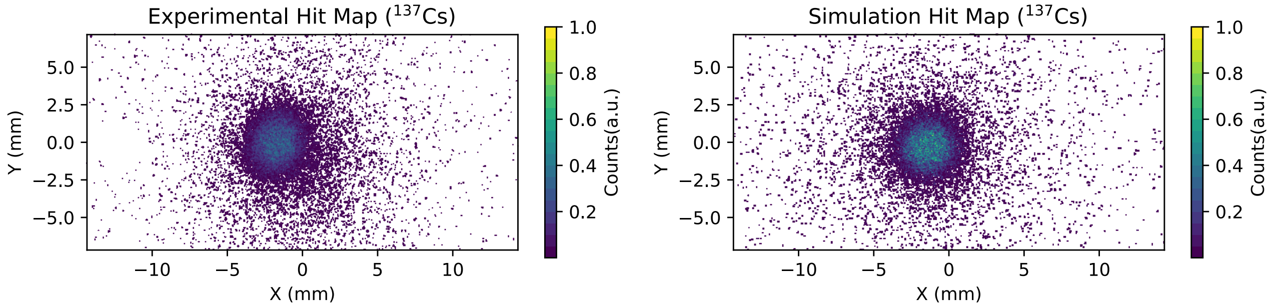

Figure 6.2: Comparison between the 2D image experimentally obtained using a ^{137}Cs source during the ALPIDE detector tests and the 2D image obtained through the Monte Carlo simulations via Geant4. The source is positioned 2 mm away from the detector surface.

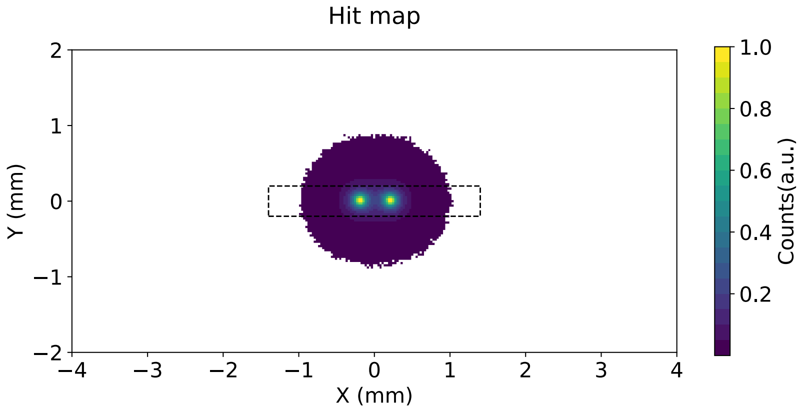

Figure 6.3: Two-cell image acquired in a two-dimensional cell culture with both cells placed at the center of the culture medium. The cells are separated along the x axis with a fixed distance of 0.4 mm. The image is post-processed by removing bins with very low counts (less than 0.1% of the counts in the most populated bin) and then zoomed in.

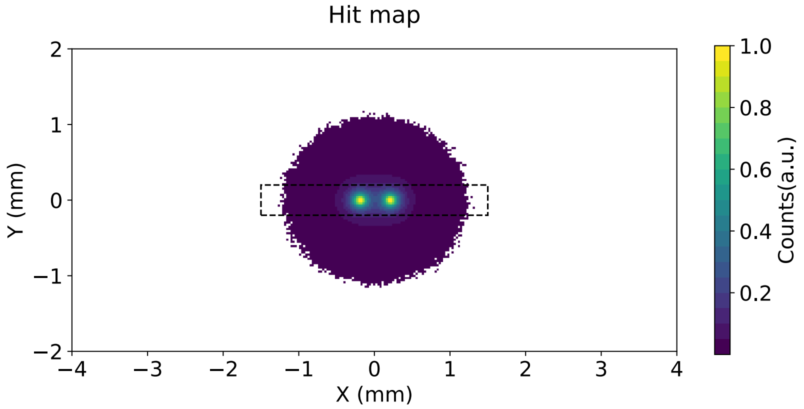

Figure 6.4: Two-cell image acquired in a three-dimensional cell culture with both cells placed in contact with the lower surface of the culture hydrogel volume. The cells are separated along the x axis with a fixed distance of 0.4 mm. The image is post-processed by removing bins with very low counts (less than 0.05% of the counts in the most populated bin) and then zoomed in.

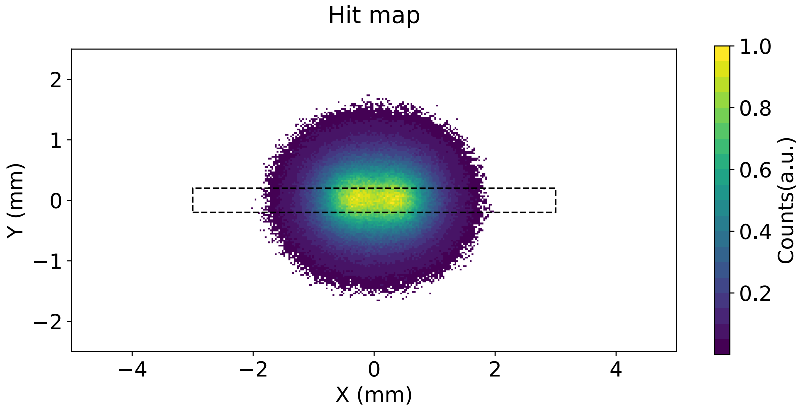

Figure 6.5: Two-cell image acquired in a three-dimensional cell culture with both cells placed in contact with the upper surface of the culture hydrogel volume. The cells are separated along the x axis with a fixed distance of 0.8 mm. The image is post-processed by removing bins with very low counts (less than 0.05% of the counts in the most populated bin) and then zoomed in.

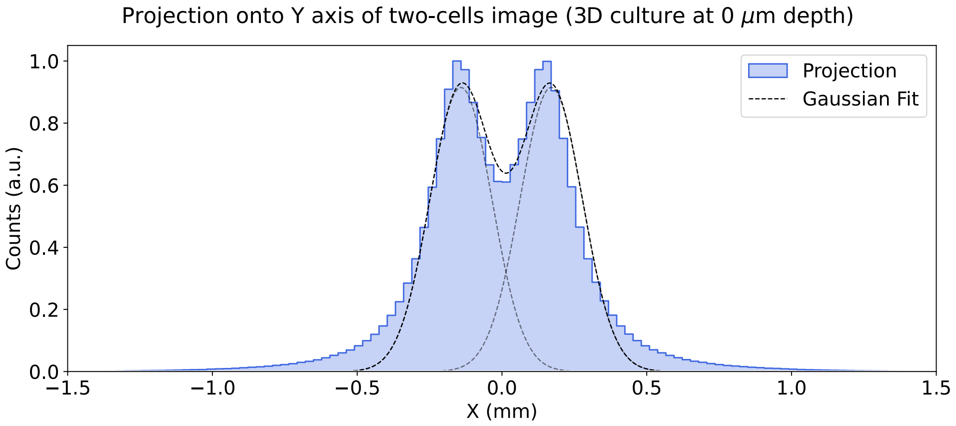

Figure 6.6: Projections onto the x axis of the two-cell image obtained in a three-dimensional cell culture with two cells positioned in contact with the lower surface of the culture hydrogel volume. The cells are separated along the x axis with a predetermined distance of 0.4 mm. The profile is fitted with a function that is the sum of two Gaussian distributions, each of which is also represented individually.

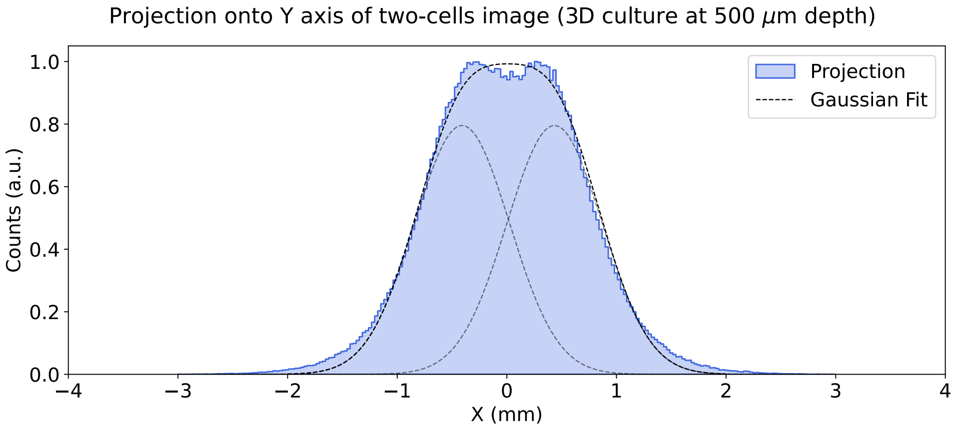

Figure 6.7: Projections onto the x axis of the two-cell image obtained in a three-dimensional cell culture with two cells positioned in contact with the upper surface of the culture hydrogel volume. The cells are separated along the x axis with a predetermined distance of 0.8 mm. The profile is fitted with a function that is the sum of two Gaussian distributions, each of which is also represented individually.

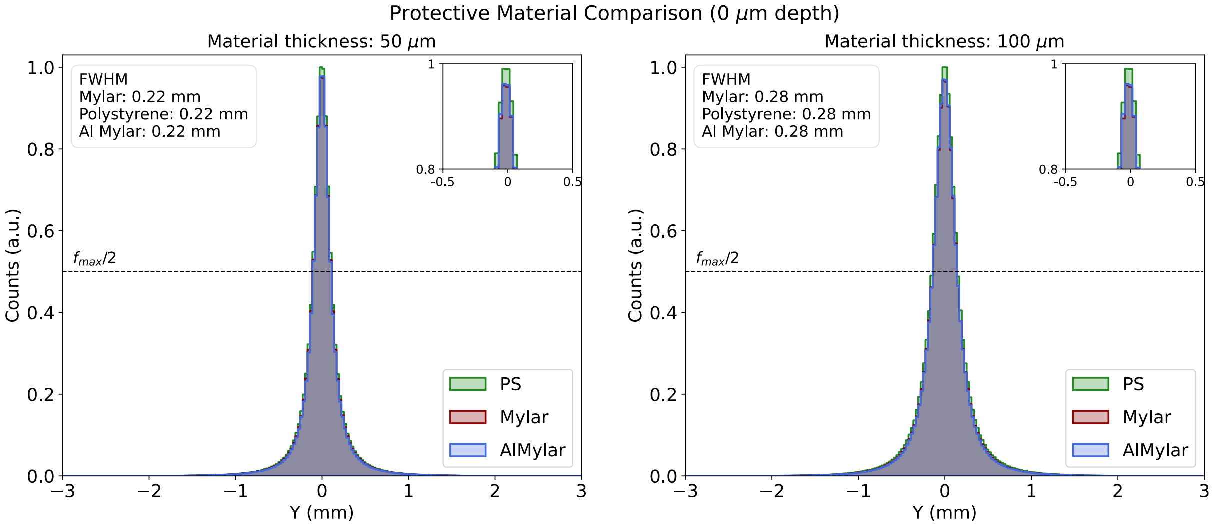

(a)

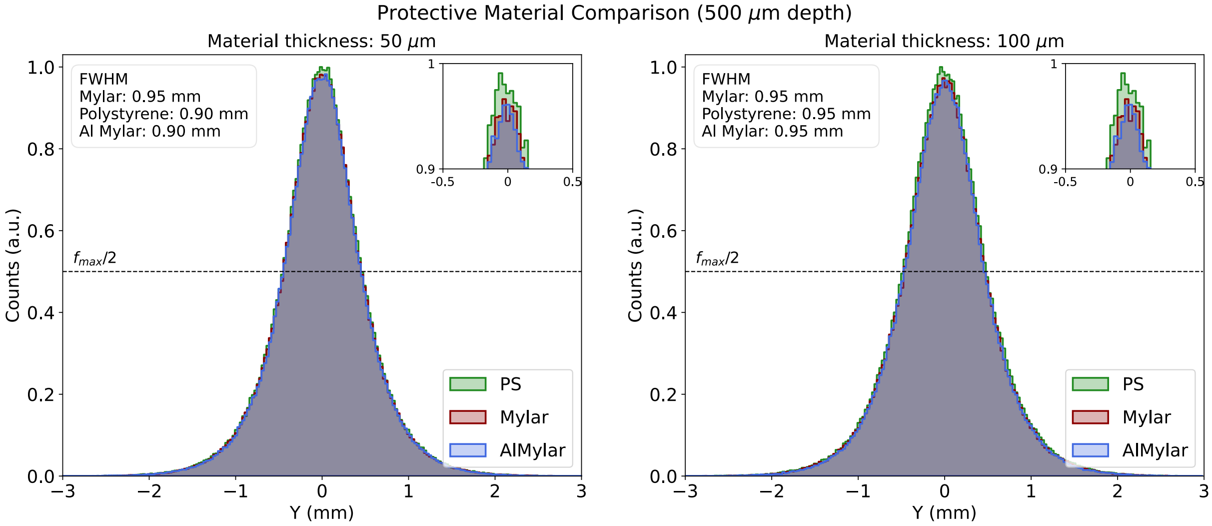

(b)

Figure 6.8: Comparison of the projections of single-cell images onto the y axis obtained by simulating different candidate materials for the protective layer (mylar, aluminated mylar, and polystyrene). The cell is placed in contact with the (a) lower and (b) upper surface of a three-dimensional cell culture. In each image, the Full Width Half Maximum (FWHM) associated with the obtained peaks is reported.

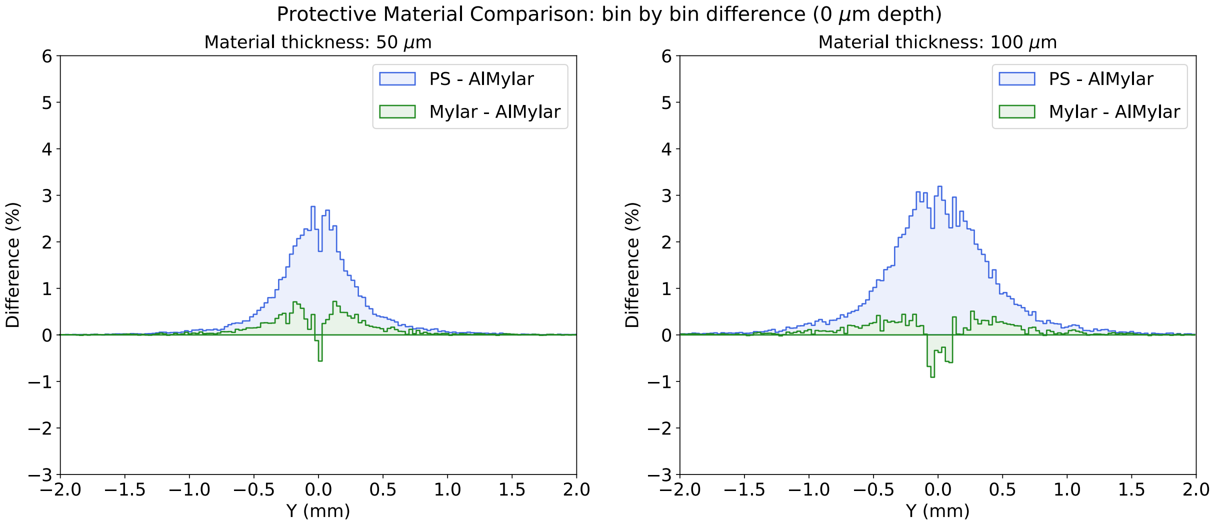

(a)

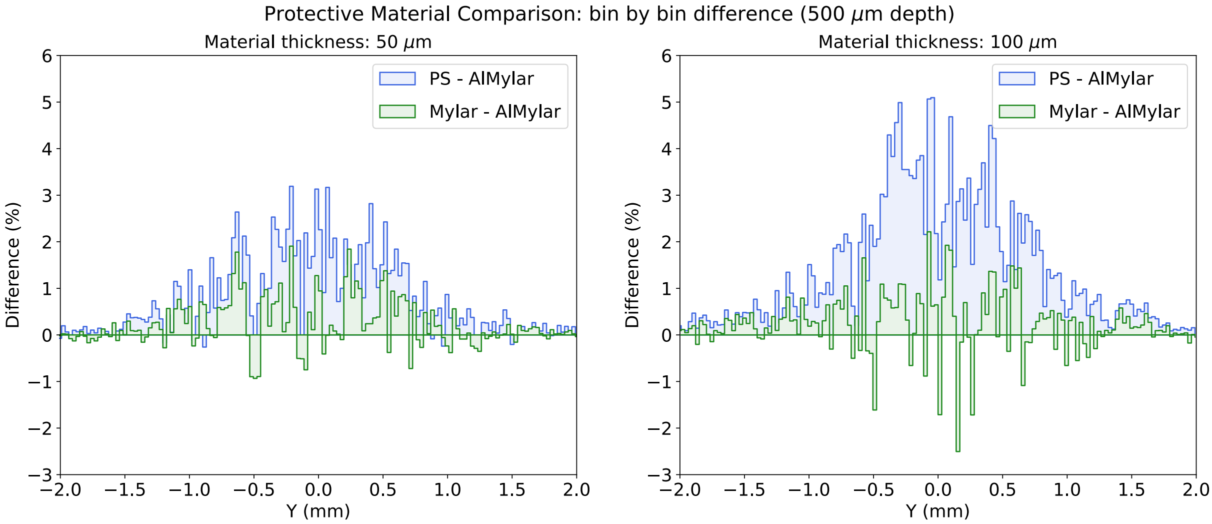

(b)

Figure 6.9: Difference between the projections of single-cell images onto the y axis between aluminated mylar and mylar, and aluminated mylar and polystyrene as materials for the protective film. The cell is placed in contact with the (a) lower and (b) upper surface of a three-dimensional cell culture.

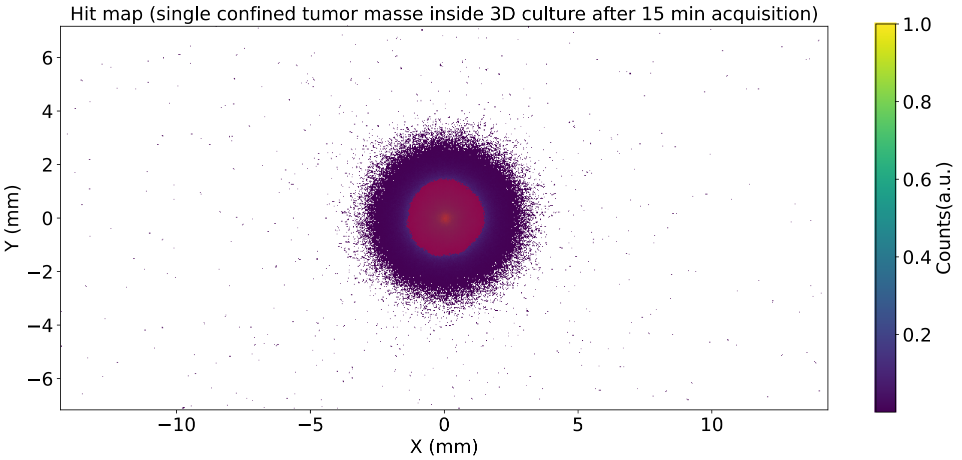

Figure 6.10: Image of an ill volume obtained by simulating a single tumor mass (circular) with a maximum diameter of 2.82 mm inside a hydrogel-based heterogeneous culture. Cancer cells are randomly distributed within the diseased tissue volume. The image simulates a 15-minutes acquisition. The radiopharmaceutical is only internalized by tumor cells: a random number of drug molecules, chosen within the range [10^5, $5{\times}10^6$], is deposited on each cell. In red, the foreground region is highlighted, selected as the area with a number of hits exceeding 10% of the maximum count value.

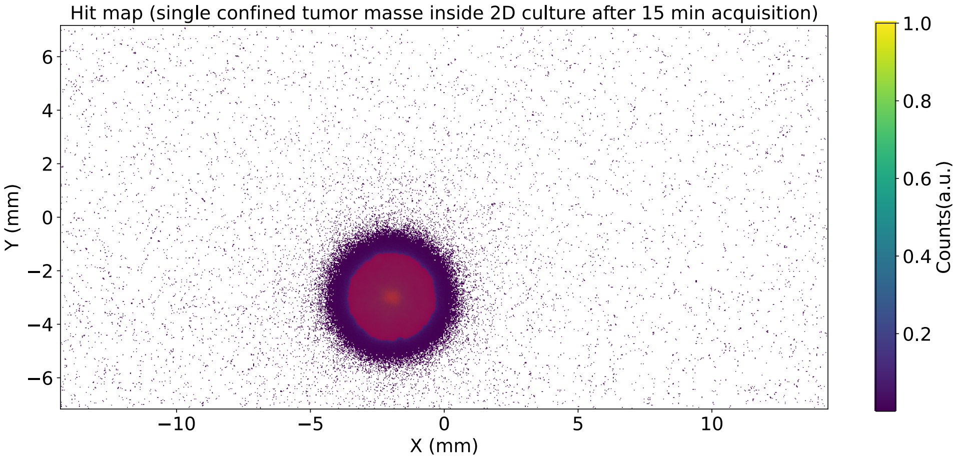

Figure 6.11: Image of an ill volume obtained by simulating a single tumor mass (circular) with a maximum diameter of 3.2 mm. Cancer cells are randomly distributed within the diseased tissue volume. The image simulates a 15-minutes acquisition. The radiopharmaceutical is only internalized by tumor cells: a random number of drug molecules, chosen within the range [10^5, $5{\times}10^6$], is deposited on each cell. In red, the foreground region is highlighted, selected as the area with a number of hits exceeding 10% of the maximum count value. The image is zoomed-in for better visualization.

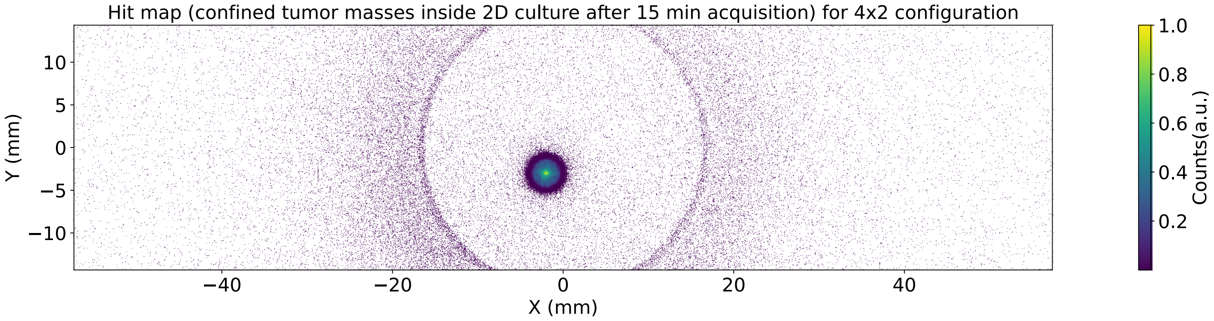

Figure 6.12: Image of an ill volume obtained by simulating a single tumor mass (circular) with a maximum diameter of 3.2 mm inside a two-dimensional heterogeneous culture. Cancer cells are randomly distributed within the diseased tissue volume. The image simulates a 15-minutes acquisition. The radiopharmaceutical is only internalized by tumor cells: a random number of drug molecules, chosen within the range [10^5, $5{\times}10^6$], is deposited on each cell. The detector is simulated in its 4 × 2 configuration, with the chips facing along their long sides.

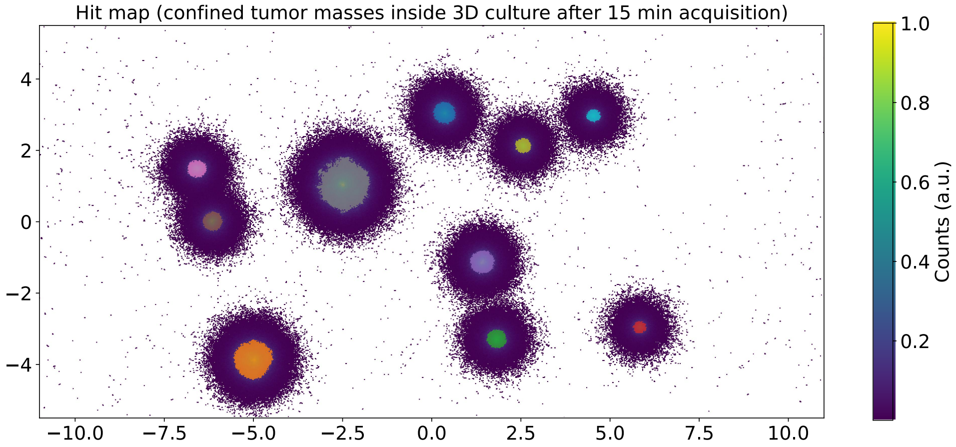

Figure 6.13: Image of an ill volume obtained by simulating different confined tumor masses (circular) with a variable dimension inside a hydrogel-based heterogeneous culture. Cancer cells are randomly distributed within every single diseased volume. The image simulates a 15-minutes acquisition. The radiopharmaceutical is only internalized by tumor cells: a random number of drug molecules, chosen within the range [10^5, $5{\times}10^6$], is deposited on each cell. The identified clusters are represented using different colors by applying the DBSCAN algorithm.

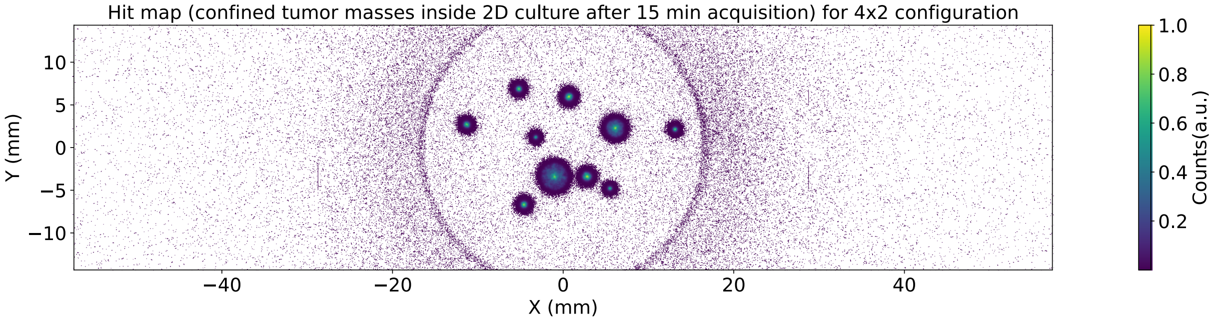

Figure 6.14: Image of an ill volume obtained by simulating different confined tumor masses (circular) with a variable dimension inside a two-dimensional heterogeneous culture. Cancer cells are randomly distributed within every single diseased volume. The image simulates a 15-minutes acquisition. The radiopharmaceutical is only internalized by tumor cells: a random number of drug molecules, chosen within the range [10^5, 5×10^6], is deposited on each cell. The detector is simulated in its 4 × 2 configuration, with the chips facing along their long sides.

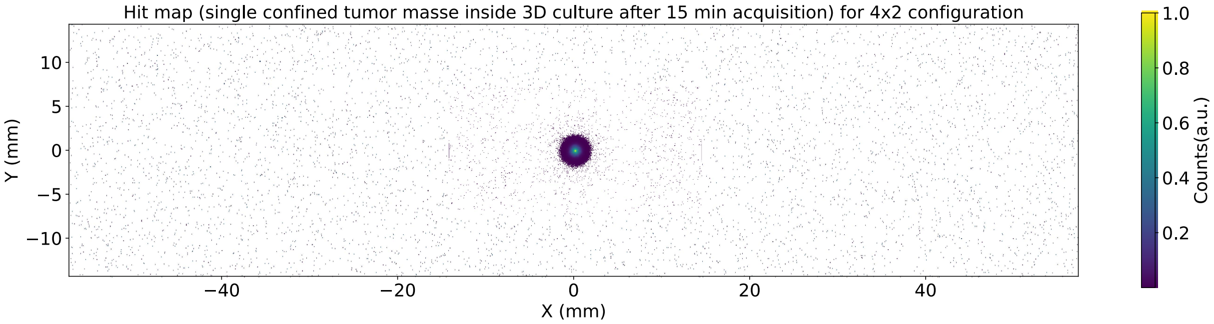

Figure 6.15: Image of an ill volume obtained by simulating a single tumor mass (circular) with a maximum diameter of 2.82 mm inside a hydrogel-based heterogeneous culture. Cancer cells are randomly distributed within the diseased tissue volume. The image simulates a 15-minutes acquisition. The radiopharmaceutical is only internalized by tumor cells: a random number of drug molecules, chosen within the range [10^5, 5×10^6], is deposited on each cell. The detector is simulated in its 4 × 2 configuration, with the chips facing along their long sides.

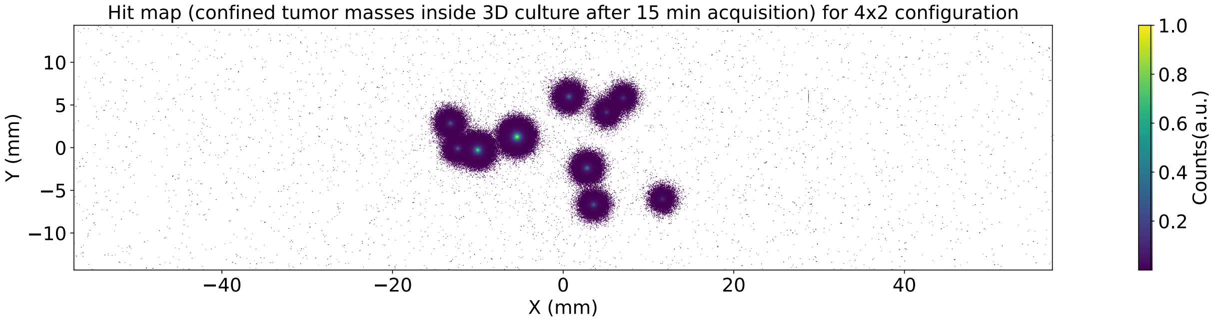

Figure 6.16: Image of an ill volume obtained by simulating different confined tumor masses (circular) with a variable dimension inside a hydrogel-based heterogeneous culture. Cancer cells are randomly distributed within every single diseased volume. The image simulates a 15-minutes acquisition. The radiopharmaceutical is only internalized by tumor cells: a random number of drug molecules, chosen within the range [10^5, 5×10^6], is deposited on each cell. The detector is simulated in its 4 × 2 configuration, with the chips facing along their long sides.

Bibliography

[1] A. Andrighetto et al. “The ISOLPHARM project: A New ISOL production method of high specific activity beta-emitting radionuclides as radiopharmaceutical precursors”. In: *International Journal of Modern Physics: Conference Series* 48 (2018), p. 1860103. DOI: 10.1142/S2010194518601035.

[2] F. Borgna. “Pharmaceutical development of the ISOL technique for the production of raadionuclides and their applications in targeted radionuclide therapy”. PhD thesis. Università degli Studi di Padova, 2018.

[3] Università degli Studi di Trento. 2020. URL: https://www.unitn.it/biotech/ (visited on 04/11/2023).

[4] Alberto Arzenton. “Radiobiological model for -emitter radiopharmaceutical therapy in dynamic cell cultures in the framework of the ISOLPHARM project”. In: *Il Nuovo Cimento C* 46.3 (June 2023), pp. 1–10. ISSN: 03905551, 03905551. DOI: 10.1393/ncc/i2023-23072-3.

[5] ISOLPHARM. 2023. URL: https://isolpharm.pd.infn.it/web/ (visited on 04/11/2023).

[6] E. Vettorato et al. “A new production method of high specific activity radionuclides towards innovative radiopharmaceuticals: The ISOLPHARM project”. In: *RAD Conference Proceedings* (2022). DOI: 10.21175/radproc.2022.02.

[7] Alberto Monetti et al. “The RIB production target for the SPES project”. In: *The European Physical Journal A* 51.10 (2015). DOI: 10.1140/epja/i2015-15128-6.

[8] A. Andrighetto et al. “Spes: The Infn Radioactive Beam Facility for Nuclear Physics”. In: *AIP Conference Proceedings* (2012). DOI: 10.1063/1.4764202.

[9] Mattia Manzolaro, Giovanni Meneghetti, and Alberto Andrighetto. “Thermal–electric numerical simulation of a surface ion source for the production of radioactive ion beams”. In: *Nuclear Instruments and Methods in Physics Research Section A: Accelerators, Spectrometers, Detectors and Associated Equipment* 623.3 (2010), pp. 1061–1069. ISSN: 0168-9002. DOI: 10.1016/j.nima.2010.08.087.

[10] F. Borgna et al. “A preliminary study for the production of high specific activity radionuclides for nuclear medicine obtained with the isotope separation on line technique”. In: *Applied Radiation and Isotopes* 127 (2017), pp. 214–226. ISSN: 0969-8043. DOI: 10.1016/j.apradiso.2017.06.022.

[11] L. Morselli. “Production and Characterization of ^{111}Ag for radiopharmaceutical applications in the framework of the ISOLPHARM project”. PhD thesis. Università degli Studi di Ferrara, 2022.

[12] M. Ballan. “Development of targets for the production of radionuclides of medical interest according to the ISOL technique”. PhD thesis. Università degli Studi di Ferrara, 2018.

[13] A. Arzenton. “Monte Carlo based dosimetry using PET/CT and SPECT/CT imaging in radiopharmaceutical therapy in the context of the ISOLPHARM project”. MA thesis. Università degli Studi di Padova, 2021.

[14] Isao Kuroda. “Effective use of strontium-89 in osseous metastases”. In: *Annals of Nuclear Medicine* 26.3 (2011), pp. 197–206. DOI: 10.1007/s12149-011-0560-5.

[15] Fazle Hosain and Richard P. Spencer. “Radiopharmaceuticals for palliation of metastatic osseous lesions: Biologic and physical background”. In: *Seminars in Nuclear Medicine* 22.1 (1992), pp. 11–16. ISSN: 0001-2998. DOI: 10.1016/S0001-2998(05)80152-7.

[16] Riad Salem and Kenneth G. Thurston. “Radioembolization with 90-Yttrium Microspheres: A State-of-the-Art Brachytherapy Treatment for Primary and Secondary Liver Malignancies: Part 1: Technical and Methodologic Considerations”. In: *Journal of Vascular and Interventional Radiology* 17.8 (2006), pp. 1251–1278. ISSN: 1051-0443. DOI: 10.1097/01.RVI.0000233785.75257.9A.

[17] Silke B Schwarz et al. “Iodine-125 brachytherapy for brain tumours - A Review”. In: *Radiation Oncology* 7.1 (2012). DOI: 10.1186/1748-717x-7-30.

[18] Freek J. Beekman et al. “Towards in vivo nuclear microscopy: iodine-125 imaging in mice using micro-pinholes”. In: *European Journal of Nuclear Medicine and Molecular Imaging* 29.7 (2002). ISSN: 1619-7070, 1619-7089. DOI: 10.1007/s00259-002-0805-6.

[19] Yan-Li Xue et al. “Value of 131-I SPECT/CT for the evaluation of differentiated thyroid cancer: A systematic review of the literature”. In: *European Journal of Nuclear Medicine and Molecular Imaging* 40.5 (2012), pp. 768–778. DOI: 10.1007/s00259-012-2310-x.

[20] Richard J. Robbins and Martin J. Schlumberger. “The Evolving Role of 131I for the Treatment of Differentiated Thyroid Carcinoma”. In: *Journal of Nuclear Medicine* 46.1 suppl (2005), 28S–37S. ISSN: 0161-5505.

[21] L. Morselli et al. “Production and characterization of 111Ag radioisotope for medical use in a TRIGA Mark II nuclear research reactor”. In: *Applied Radiation and Isotopes* (2023), p. 110798. ISSN: 0969-8043. DOI: 10.1016/j.apradiso.2023.110798.

[22] Brookhaven National Laboratory. *National Nuclear Data Center*. URL: https://www.nndc.bnl.gov/nudat3/ (visited on 04/14/2023).

[23] P.August Schubiger and Alan Smith. “Optimising the radioimmunotherapy of malignant disease: the broadening choice of carrier and effector moieties”. In: *Pharmaceutica Acta Helvetiae* 70.3 (1995), pp. 203–217. ISSN: 0031-6865. DOI: 10.1016/0031-6865(95)00013-Y.

[24] International Atomic Energy Agency. 2023. URL: https://www-nds.iaea.org/ (visited on 04/22/2023).

[25] S. Agostinelli et al. “GEANT4 – a simulation toolkit”. In: *Nucl. Instrum. Meth. A* 506 (2003), pp. 250–303. DOI: 10.1016/S0168-9002(03)01368-8.

[26] F. Rohrlich and B.C. Carlson. In: 93.1 (1954), pp. 38–44. DOI: 10.1103/PhysRev.93.38.

[27] Claude Leroy and Pier-Giorgio Rancoita. *Principles of radiation interaction in matter and detection*. Singapore: World Scientific, 2011. ISBN: 978-981-238-909-1. DOI: 10.1142/5578.

[28] Richard Wilson. “A Formula for Thick Target Bremsstrahlung”. In: *Proceedings of the Physical Society. Section A* 66.7 (1953), p. 638. DOI: 10.1088/0370-1298/66/7/309.

[29] Ugo Amaldi. “Fluctuations in Calorimetry Measurements”. In: *Physica Scripta* 23.4A (Apr. 1981), p. 409. DOI: 10.1088/0031-8949/23/4A/012.

[30] National Institute of Standards and Technology (NIST). 2023. URL: https://physics.nist.gov/PhysRefData/Star/Text/ESTAR.html (visited on 04/24/2023).

[31] Kenneth R. Hogstrom and Peter R. Almond. “Review of electron beam therapy physics”. In: *Physics in Medicine Biology* 51.13 (June 2006), R455. DOI: 10.1088/0031-9155/51/13/R25.

[32] I. H. Kunkler e J. Walter C. K. Bomford. *Walter and Miller’s textbook of radiotherapy : radiation physics, therapy, and oncology*. Eighth. Churchill Livingstone, 2003.

[33] George Sgouros et al. “Radiopharmaceutical therapy in cancer: Clinical advances and challenges”. In: *Nature Reviews Drug Discovery* 19.9 (2020), pp. 589–608. DOI: 10.1038/s41573-020-0073-9.

[34] Sadaf Aghevlian, Amanda J. Boyle, and Raymond M. Reilly. “Radioimmunotherapy of cancer with high linear energy transfer (LET) radiation delivered by radionuclides emitting -particles

or Auger electrons”. In: *Advanced Drug Delivery Reviews* 109 (2017). Radiotherapy for cancer: present and future, pp. 102–118. ISSN: 0169-409X. DOI: 10.1016/j.addr.2015.12.003.

[35] “The 2007 Recommendations of the International Commission on Radiological Protection. ICRP publication 103.” In: *Annals of the ICRP* 37.2-4 (2007), pp. 1–332. DOI: 10.1016/j.icrp.2007.10.003.

[36] Michael S Hofman et al. “[^{177}Lu]-PSMA-617 radionuclide treatment in patients with metastatic castration-resistant prostate cancer (LuPSMA trial): a single-centre, single-arm, phase 2 study”. In: *The Lancet Oncology* 19.6 (2018), pp. 825–833. ISSN: 1470-2045. DOI: 10.1016/S1470-2045(18)30198-0.

[37] Ute Hennrich and Klaus Kopka. “Lutathera®: The First FDA- and EMA-Approved Radiopharmaceutical for Peptide Receptor Radionuclide Therapy”. In: *Pharmaceuticals* 12.3 (2019). ISSN: 1424-8247. DOI: 10.3390/ph12030114.

[38] Rafael C. Gonzalez and Richard E. Woods. *Digital image processing.* 2. ed. Prentice-Hall, 2002. ISBN: 0-201-18075-8.

[39] Mina M. Benjamin, Marco Shaker, and Mark G. Rabbat. “Chapter 5 - Assessing coronary artery disease using coronary computed tomography angiography”. In: *Cardiovascular and Coronary Artery Imaging.* Ed. by Ayman S. El-Baz and Jasjit S. Suri. Academic Press, 2022, pp. 129–145. ISBN: 978-0-12-822706-0. DOI: 10.1016/B978-0-12-822706-0.00011-1.

[40] *Nuclear Medicine Physics.* Non-serial Publications. Vienna: INTERNATIONAL ATOMIC ENERGY AGENCY, 2015. ISBN: 978-92-0-143810-2. URL: https://www.iaea.org/publications/10368/nuclear-medicine-physics.

[41] Max Born et al. *Principles of Optics: Electromagnetic Theory of Propagation, Interference and Diffraction of Light.* 7th ed. Cambridge University Press, 1999. DOI: 10.1017/CBO9781139644181.

[42] Edinburgh Instruments. 2023. URL: https://www.edinst.com/blog/the-rayleigh-criterion-for-microscope-resolution/ (visited on 03/02/2023).

[43] Holger Pettersson. *The Encyclopedia of Medical Imaging.* NICER Institute, 1999.

[44] Haney A Alsleem and Hussain M Almohiy. “The Feasibility of Contrast-to-Noise Ratio on Measurements to Evaluate CT Image Quality in Terms of Low-Contrast Detailed Detectability”. In: *Medical Sciences* 8.3 (2020). ISSN: 2076-3271. DOI: 10.3390/medsci8030026.

[45] Debanti Sengupta et al. “Bright Lu2O3:Eu Thin-Film Scintillators for High-Resolution Radioluminescence Microscopy”. In: *Advanced healthcare materials* 4 (July 2015). DOI: 10.1002/adhm.201500372.

[46] Nicole Barthe et al. “Chapter 9 - High-resolution beta imaging”. In: *Handbook of Radioactivity Analysis: Volume 2 (Fourth Edition).* Ed. by Michael F. L’Annunziata. Fourth Edition. Academic Press, 2020, pp. 669–727. ISBN: 978-0-12-814395-7. DOI: 10.1016/B978-0-12-814395-7.00009-X.

[47] Eric G. Solon. “Autoradiography techniques and quantification of drug distribution”. In: *Cell and Tissue Research* 360.1 (2015), pp. 87–107. DOI: 10.1007/s00441-014-2093-4.

[48] Kunihiro Morishima et al. “Discovery of a big void in Khufu’s Pyramid by observation of cosmic-ray muons”. In: *Nature* 552 (Dec. 2017). DOI: 10.1038/nature24647.

[49] W.M. Yen, S. Shionoya, and H. Yamamoto. *Phosphor handbook, second edition.* 2006, pp. 1–1053.

[50] H. Kumagai et al. “Development of Parallel Plate Avalanche Counter (PPAC) for BigRIPS fragment separator”. In: *Nuclear Instruments and Methods in Physics Research Section B: Beam Interactions with Materials and Atoms* 317 (Dec. 2013), pp. 717–727. DOI: 10.1016/j.nimb.2013.08.050.

[51] M. Cortesi, Y. Ayyad, and J. Yurkon. “Development of a parallel-plate avalanche counter with optical readout (O-PPAC)”. In: *Journal of Instrumentation* 13.10 (Oct. 2018), P10006. DOI: 10.1088/1748-0221/13/10/P10006.

[52] A. Breskin and N. Zwang. “A Fast, Bidimensional, Position Sensitive Parallel Plate AvalancheCounter (Ppac) for Light and Heavy Particles”. In: *IEEE Trans. Nucl. Sci.* 25 (1978), pp. 126–129. DOI: 10.1109/TNS.1978.4329290.

[53] V. Peskov et al. “Investigation of light emission from a parallel-plate avalanche chamber filled with noble gases and with TEA, TMAE, and H2O vapours at atmospheric pressure”. In: *Nuclear Instruments and Methods in Physics Research Section A: Accelerators, Spectrometers, Detectors and Associated Equipment* 277.2 (1989), pp. 547–556. ISSN: 0168-9002. DOI: 10.1016/0168-9002(89)90788-2.

[54] N Barthe et al. “Recent technologic developments on high-resolution beta imaging systems for quantitative autoradiography and double labeling applications”. In: *Nuclear Instruments and Methods in Physics Research Section A: Accelerators, Spectrometers, Detectors and Associated Equipment* 527.1 (2004). Proceedings of the 2nd International Conference on Imaging Technologies in Biomedical Sciences, pp. 41–45. ISSN: 0168-9002. DOI: 10.1016/j.nima.2004.03.014.

[55] Serge Duarte Pinto. “Micropattern gas detector technologies and applications the work of the RD51 collaboration”. In: *IEEE Nuclear Science Symposuim Medical Imaging Conference*. 2010, pp. 802–807. DOI: 10.1109/NSSMIC.2010.5873870.

[56] Fabio Sauli and Archana Sharma. “MICROPATTERN GASEOUS DETECTORS”. In: *Annual Review of Nuclear and Particle Science* 49.1 (1999), pp. 341–388. DOI: 10.1146/annurev.nucl.49.1.341.

[57] J. Manjarres et al. “Performances of Anode-resistive Micromegas for HL-LHC”. In: *Journal of Instrumentation - J INSTRUM* 7 (Feb. 2012). DOI: 10.1088/1748-0221/7/03/C03040.

[58] Tae Jin Kim, Silvan Türkcan, and Guillem Pratx. “Modular low-light microscope for imaging cellular bioluminescence and radioluminescence”. In: *Nature Protocols* 12.5 (2017), pp. 1055–1076. DOI: 10.1038/nprot.2017.008.

[59] Qian Wang et al. “Performance evaluation of 18F radioluminescence microscopy using computational simulation”. In: *Medical Physics* 44.5 (), pp. 1782–1795. DOI: 10.1002/mp.12198.

[60] Guillem Pratx et al. “High-Resolution Radioluminescence Microscopy of 18F-FDG Uptake by Reconstructing the -Ionization Track”. In: *Journal of Nuclear Medicine* 54.10 (2013), pp. 1841–1846. ISSN: 0161-5505. DOI: 10.2967/jnumed.112.113365.

[61] M. Mager. “ALPIDE, the Monolithic Active Pixel Sensor for the ALICE ITS upgrade”. In: *Nuclear Instruments and Methods in Physics Research Section A: Accelerators, Spectrometers, Detectors and Associated Equipment* 824 (2016). Frontier Detectors for Frontier Physics: Proceedings of the 13th Pisa Meeting on Advanced Detectors, pp. 434–438. ISSN: 0168-9002. DOI: 10.1016/j.nima.2015.09.057.

[62] B. Abelev et al and (The ALICE Collaboration). In: 41.8 (July 2014), p. 087002. DOI: 10.1088/0954-3899/41/8/087002.

[63] F. Colamaria et al. “Study of the photon rejection of the ALPIDE pixel detector for medicalapplications”. In: *2019 IEEE 8th International Workshop on Advances in Sensors and Interfaces(IWASI)*. 2019, pp. 1–6. DOI: 10.1109/IWASI.2019.8791306.

[64] G. Tambave et al. “Characterization of monolithic CMOS pixel sensor chip with ion beams for application in particle computed tomography”. In: *Nuclear Instruments and Methods in Physics Research Section A: Accelerators, Spectrometers, Detectors and Associated Equipment* 958 (2020). Proceedings of the Vienna Conference on Instrumentation 2019, p. 162626. ISSN: 0168-9002. DOI: 10.1016/j.nima.2019.162626.

[65] W. Snoeys. “CMOS monolithic active pixel sensors for high energy physics”. In: *Nuclear Instruments and Methods in Physics Research Section A: Accelerators, Spectrometers, Detectors and Associated Equipment* 765 (2014), pp. 167–171. ISSN: 0168-9002. DOI: 10.1016/j.nima.2014.07.017.

[66] CERN. 2021. URL: https://home.cern/news/news/experiments/ls2-report-upgraded-inner-tracking-system-joins-alice-detector (visited on 04/21/2023).

[67] Andrea Sofia Triolo. "Calibration of the Upgraded ALICE Inner Tracking System". In: *10th International Workshop on Semiconductor Pixel Detectors for Particles and Imaging (PIXEL)*. 2023. DOI: 10.48550/arXiv.2302.00433.

[68] Francesco Barile and Vito Manzari. "Characterization of the prototype pixel chip for the ALICE ITS upgrade". In: *2015 6th International Workshop on Advances in Sensors and Interfaces (IWASI)*. 2015, pp. 63–67. DOI: 10.1109/IWASI.2015.7184948.

[69] G. on behalf of the ALICE collaboration Contin. "The MAPS-based ITS Upgrade for ALICE". In: *The 28-th International Workshop on Vertex Detectors*. 2019. DOI: 10.22323/1.373.0003.

[70] J. Prabket et al. "Resistivity profile of epitaxial layer for the new ALICE ITS sensor". In: *Journal of Instrumentation* 14.05 (2019), T05006. DOI: 10.1088/1748-0221/14/05/T05006.

[71] ALICE ITS ALPIDE development team. *ALPIDE Operations Manual*. Version 0.3. 2016.

[72] Tarek Saydé et al. "Biomaterials for Three-Dimensional Cell Culture: From Applications in Oncology to Nanotechnology". In: *Nanomaterials* 11.2 (2021). ISSN: 2079-4991. DOI: 10.3390/nano11020481.

[73] R Ian Freshney and Amanda Capes-Davis. *Freshney's culture of animal cells*. 8th ed. Standards Information Network, Mar. 2021.

[74] Charles T Ambrose. "An amended history of tissue culture: Concerning Harrison, Burrows, Mall, and Carrel". In: *Journal of Medical Biography* 27.2 (Jan. 2017), pp. 95–102. DOI: 10.1177/0967772016685033.

[75] W. D. Coffman G.O. Gey and M. T. Kubicek. "Tissue Culture Studies of the proliferative capacity of cervical carcinoma and normal epithelium". In: *Cancer Research* 12 (1952), pp. 264–265.

[76] Kitaek Lim et al. "Cell Image Processing Methods for Automatic Cell Pattern Recognition and Morphological Analysis of Mesenchymal Stem Cells - An Algorithm for Cell Classification and Adaptive Brightness Correction". In: *Journal of Biosystems Engineering* 30.1 (2013), pp. 55–63. DOI: 10.5307/JBE.2013.38.1.055.

[77] Onur Uysal et al. "Chapter 17 - Cell and Tissue Culture: The Base of Biotechnology". In: *Omics Technologies and Bio-Engineering*. Ed. by Debmalya Barh and Vasco Azevedo. Academic Press, 2018, pp. 391–429. ISBN: 978-0-12-804659-3. DOI: 10.1016/B978-0-12-804659-3.00017-8.

[78] Jennie P. Mather and Penelope E. Roberts. *Introduction to Cell and Tissue Culture*. Springer US, 1998. DOI: 10.1007/b102298.

[79] Merck KGaA. *ECACC Handbook - Fundamental Techniques in Cell Culture Laboratory Handbook*. 4th edition. 2018.

[80] S. Sood et al. "2.13 - Inoculum Preparation". In: *Comprehensive Biotechnology (Second Edition)*. Ed. by Murray Moo-Young. Second Edition. Burlington: Academic Press, 2011, pp. 151–164. ISBN: 978-0-08-088504-9. DOI: 10.1016/B978-0-08-088504-9.00090-8.

[81] Meenakshi Arora. "Cell Culture Media: A Review". In: *Materials and Methods* 3 (Mar. 2013). DOI: 10.13070/mm.en.3.175.

[82] Michael L Shuler and Fikret Kargi. *Bioprocess Engineering*. 2nd ed. Prentice Hall international series in the physical and chemical engineering sciences. Philadelphia, PA: Prentice Hall, 2000. ISBN: 0-13-081908-5.

[83] Marta Kapałczyńska et al. "2D and 3D cell cultures – a comparison of different types of cancer cell cultures". In: *Archives of Medical Science* (2016). DOI: 10.5114/aoms.2016.63743.

[84] UPM Biomedicals. 2023. URL: https://www.upmbiomedicals.com/B (visited on 06/18/2023).

[85] John W. Haycock. "3D Cell Culture: A Review of Current Approaches and Techniques". In: *Methods in Molecular Biology*. Humana Press, Oct. 2010, pp. 1–15. DOI: 10.1007/978-1-60761-984-0_1.

[86] Sudha Krishnamurthy and Jacques E. Nör. “Orosphere assay: A method for propagation of head and neck cancer stem cells”. In: *Head &amp Neck* 35.7 (July 2012), pp. 1015–1021. doi: `10.1002/hed.23076`.

[87] CERN. 2023. url: `https://geant4.web.cern.ch/` (visited on 05/27/2023).

[88] Omrane Kadri et al. “Application of GEANT4 code in gamma irradiation processing”. In: Jan. 2010, pp. 477–492.

[89] Tullio Basaglia et al. “Experimental quantification of Geant4 PhysicsList recommendations: methods and results”. In: *Journal of Physics: Conference Series* 664.7 (Dec. 2015), p. 072037. doi: `10.1088/1742-6596/664/7/072037`.

[90] Geant4 Collaboration. 2022. url: `https://geant4-userdoc.web.cern.ch/UsersGuides/ForApplicationDeveloper/html/index.html` (visited on 06/26/2023).

[91] Tatsumi Koi. “EM Physics”. In: SLAC GEANT4 Tutorial Course, 2014.

[92] International Atomic Energy Agency - Nuclear Data Section. 2023. url: `https://www-nds.iaea.org/epdl97/` (visited on 06/26/2023).

[93] O. Klein and Y. Nishina. “Über die Streuung von Strahlung durch freie Elektronen nach der neuen relativistischen Quantendynamik von Dirac”. In: *Zeitschrift für Physik* 52.11-12 (Nov. 1929), pp. 853–868. doi: `10.1007/bf01366453`.

[94] “On the stopping of fast particles and on the creation of positive electrons”. In: *Proceedings of the Royal Society of London. Series A, Containing Papers of a Mathematical and Physical Character* 146.856 (Aug. 1934), pp. 83–112. doi: `10.1098/rspa.1934.0140`.

[95] S. Saito. “Low-Energy Theorem for Compton Scattering”. In: *Physical Review* 184.5 (Aug. 1969), pp. 1894–1902. doi: `10.1103/physrev.184.1894`.

[96] J. Sempau et al. “Experimental benchmarks of the Monte Carlo code penelope”. In: *Nuclear Instruments and Methods in Physics Research Section B: Beam Interactions with Materials and Atoms* 207.2 (June 2003), pp. 107–123. doi: `10.1016/s0168-583x(03)00453-1`.

[97] GEANT4 Collaboration. *Guide For Physics Lists.* Version 6.0. 2021.

[98] E. Rutherford. “LXXIX. iThe scattering of and particles by matter and the structure of the atom/i”. In: *The London, Edinburgh, and Dublin Philosophical Magazine and Journal of Science* 21.125 (May 1911), pp. 669–688. doi: `10.1080/14786440508637080`.

[99] Laszlo Urban. “A model for multiple scattering in Geant4”. In: (Dec. 2006).

[100] H. J. Bhabha. “The scattering of positrons by electrons with exchange on Dirac’s theory of the positron”. In: *Proceedings of the Royal Society of London. Series A - Mathematical and Physical Sciences* 154.881 (Mar. 1936), pp. 195–206. doi: `10.1098/rspa.1936.0046`.

[101] Stephen M. Seltzer and Martin J. Berger. “Bremsstrahlung spectra from electron interactions with screened atomic nuclei and orbital electrons”. In: *Nuclear Instruments and Methods in Physics Research Section B: Beam Interactions with Materials and Atoms* 12.1 (Aug. 1985), pp. 95–134. doi: `10.1016/0168-583x(85)90707-4`.

[102] S. Goudsmit and J. L. Saunderson. “Multiple Scattering of Electrons”. In: *Physical Review* 57.1 (Jan. 1940), pp. 24–29. doi: `10.1103/physrev.57.24`.

[103] P. Arce et al. “Report on G4-Med, a Geant4 benchmarking system for medical physics applications developed by the Geant4 Medical Simulation Benchmarking Group”. In: *Medical Physics* 48.1 (Dec. 2020), pp. 19–56. doi: `10.1002/mp.14226`.

[104] Brookhaven National Laboratory. 2023. url: `https://www.nndc.bnl.gov/ensdf/` (visited on 06/25/2023).

[105] Steffen Hauf et al. “Validation of Geant4-Based Radioactive Decay Simulation”. In: *IEEE Transactions on Nuclear Science* 60.4 (Aug. 2013), pp. 2984–2997. doi: `10.1109/tns.2013.2271047`.

[106] GEANT4 Collaboration. *Physics Reference Manual.* Version 4.0. 2019.

[107] Steffen Hauf et al. “Radioactive Decays in Geant4”. In: *IEEE Transactions on Nuclear Science* 60.4 (Aug. 2013), pp. 2966–2983. DOI: `10.1109/tns.2013.2270894`.

[108] P Venkataramaiah et al. “A simple relation for the Fermi function”. In: *Journal of Physics G: Nuclear Physics* 11.3 (Mar. 1985), pp. 359–364. DOI: `10.1088/0305-4616/11/3/014`.

[109] M.E. ROSE. “Analysis of Beta Decay Data”. In: *Pure and Applied Physics*. Elsevier, 1960, pp. 811–833. DOI: `10.1016/b978-1-4832-3064-1.50011-5`.

[110] Si-Jie Hao et al. “Size-based separation methods of circulating tumor cells”. In: *Advanced Drug Delivery Reviews* 125 (Feb. 2018), pp. 3–20. DOI: `10.1016/j.addr.2018.01.002`.

[111] Sara Mohammadi, Mahdy Ebrahimi Loushab, and Mohammad Taghi Bahreyni Toossi. “Geant4 Modeling of Cellular Dosimetry of 188Re: Comparison between Geant4 Predicted Surviving Fraction and Experimentally Surviving Fraction Determined by MTT Assay”. In: *Journal of Biomedical Physics and Engineering* (2021). DOI: `10.31661/jbpe.v0i0.1050`.

[112] SARSTEDT AG Co. 2023. URL: `https://www.sarstedt.com/en/` (visited on 07/05/2023).

[113] Jindřich Kopeček. “Hydrogel biomaterials: A smart future?” In: *Biomaterials* 28.34 (Dec. 2007), pp. 5185–5192. DOI: `10.1016/j.biomaterials.2007.07.044`.

[114] Enas M. Ahmed. “Hydrogel: Preparation, characterization, and applications: A review”. In: *Journal of Advanced Research* 6.2 (Mar. 2015), pp. 105–121. DOI: `10.1016/j.jare.2013.07.006`.

[115] Guoliang Ying et al. “Three-dimensional bioprinting of gelatin methacryloyl (GelMA)”. In: *Bio-Design and Manufacturing* 1.4 (Nov. 2018), pp. 215–224. DOI: `10.1007/s42242-018-0028-8`.

[116] Laboratorio Energia Nucleare Applicata. 2020. URL: `https://lena.unipv.it/` (visited on 07/26/2023).

[117] Spectrum Techniques. 2023. URL: `https://www.spectrumtechniques.com/` (visited on 07/26/2023).

[118] Steffen Beirle et al. “Parameterizing the instrumental spectral response function and its changes by a super-Gaussian and its derivatives”. In: *Atmospheric Measurement Techniques* 10.2 (Feb. 2017), pp. 581–598. DOI: `10.5194/amt-10-581-2017`.

[119] Sadettin S. Ozturk. “Engineering challenges in high density cell culture systems”. In: *Cytotechnology* 22.1-3 (1996), pp. 3–16. DOI: `10.1007/bf00353919`.

[120] American Type Culture Collection. *ATCC Animal Cell Culture Guide: Tips and Techniques for Continuous Cell Lines*. American Type Culture Collection, 2012.

[121] Marco Verona et al. “Preliminary Study of a 1, 5-Benzodiazepine-Derivative Labelled with Indium-111 for CCK-2 Receptor Targeting”. In: *Molecules* 26.4 (Feb. 2021), p. 918. DOI: `10.3390/molecules26040918`.

[122] Roland Moll et al. “The catalog of human cytokeratins: Patterns of expression in normal epithelia, tumors and cultured cells”. In: *Cell* 31.1 (Nov. 1982), pp. 11–24. DOI: `10.1016/0092-8674(82)90400-7`.

[123] Dirk Drasdo and Stefan Höhme. “A single-cell-based model of tumor growthiin vitro/i: monolayers and spheroids”. In: *Physical Biology* 2.3 (July 2005), pp. 133–147. DOI: `10.1088/1478-3975/2/3/001`.

[124] Shraddha K. Popat and M. Emmanuel. “Review and comparative study of clustering techniques”. In: *International journal of computer science and information technologies* 5.1 (2014), pp. 805–812.

[125] Attri Ghosal et al. “A Short Review on Different Clustering Techniques and Their Applications”. In: *Advances in Intelligent Systems and Computing*. Springer Singapore, July 2019, pp. 69–83. DOI: `10.1007/978-981-13-7403-6_9`.

[126] Scikit-learn developers. 2023. URL: `https://scikit-learn.org/stable/modules/generated/sklearn.cluster.DBSCAN.html` (visited on 08/01/2023).

[127] Guido Van Rossum and Fred L. Drake. *Python 3 Reference Manual.* Scotts Valley, CA: CreateSpace, 2009. ISBN: 1441412697.